Remote Sensing Observations of Tundra Snow with Ku- and X-band Radar

by

Joshua Michael Lloyd King

A thesis
presented to the University of Waterloo
in fulfillment of the
thesis requirement for the degree of
Doctor of Philosophy
in
Geography

Waterloo, Ontario, Canada, 2014

This thesis consists of material all of which I authored or co-authored: See Statement of Contributions included in this thesis. This is a true copy of the thesis, including any required final revisions, as accepted by my examiners.

I understand that my thesis may be made electronically available to the public.

Abstract

Seasonal patterns of snow accumulation in the Northern Hemisphere are changing in response to variations in Arctic climate. These changes have the potential to influence global climate, regional hydrology, and sensitive ecosystems as they become more pronounced. To refine our understanding of the role of snow in the Earth system, improved methods to characterize global changes in snow extent and mass are needed. Current space-borne observations and ground-based measurement networks lack the spatial resolution to characterize changes in volumetric snow properties at the scale of ground observed variation. Recently, radar has emerged as a potential complement to existing observation methods with demonstrated sensitivity to snow volume at high spatial resolutions (< 200 m). In 2009, this potential was recognized by the proposed European Space Agency Earth Explorer mission, the Cold Regions High Resolution Hydrology Observatory ($CoReH_2O$); a satellite based dual frequency (17.2 and 9.6 GHz) radar for observation of cryospheric variables including snow water equivalent (SWE). Despite increasing international attention, snow-radar interactions specific to many snow cover types remain unevaluated at 17.2 or 9.6 GHz, including those common to the Canadian tundra. This thesis aimed to use field-based experimentation to close gaps in knowledge regarding snow-microwave interaction and to improve our understanding of how these interactions could be exploited to retrieve snow properties in tundra environments.

Between September 2009 and March 2011, a pair of multi-objective field campaigns were conducted in Churchill, Manitoba, Canada to collect snow, ice, and radar measurements in a number of unique sub-arctic environments. Three distinct experiments were undertaken to characterize and evaluate snow-radar response using novel seasonal, spatial, and destructive sampling methods in previously untested terrestrial tundra environments. Common to each experiment was the deployment of a sled-mounted dual-frequency (17.2

and 9.6 GHz) scatterometer system known as UW-Scat. This adaptable ground-based radar system was used to collect backscatter measurements across a range of representative tundra snow conditions at remote terrestrial sites. The assembled set of measurements provide an extensive database from which to evaluate the influence of seasonal processes of snow accumulation and metamorphosis on radar response.

Several advancements to our understanding of snow-radar interaction were made in this thesis. First, proof-of-concept experiments were used to establish seasonal and spatial observation protocols for ground-based evaluation. These initial experiments identified the presence of frequency dependent sensitivity to evolving snow properties in terrestrial environments. Expanding upon the preliminary experiments, a seasonal observation protocol was used to demonstrate for the first time Ku-band and X-band sensitivity to evolving snow properties at a coastal tundra observation site. Over a 5 month period, 13 discrete scatterometer observations were collected at an undisturbed snow target where Ku-band measurements were shown to hold strong sensitivity to increasing snow depth and water equivalent. Analysis of longer wavelength X-band measurements was complicated by soil response not easily separable from the target snow signal. Definitive evidence of snow volume scattering was shown by removing the snowpack from the field of view which resulted in a significant reduction in backscatter at both frequencies. An additional set of distributed snow covered tundra targets were evaluated to increase knowledge of spatiotemporal Ku-band interactions. In this experiment strong sensitivities to increasing depth and SWE were again demonstrated. To further evaluate the influence of tundra snow variability, detailed characterization of snow stratigraphy was completed within the sensor field of view and compared against collocated backscatter response. These experiments demonstrated Ku-band sensitivity to changes in tundra snow properties observed over short distances.

A contrasting homogeneous snowpack showed a reduction in variation of the radar signal in comparison to a highly variable open tundra site.

Overall, the results of this thesis support the single frequency Ku-band (17.2 GHz) retrieval of shallow tundra snow properties and encourage further study of X-band interactions to aid in decomposition of the desired snow volume signal.

Acknowledgements

First, I would like to extend gratitude to my PhD advisor Dr. Richard Kelly for providing me with the opportunity to work on this project and for insuring that I had the academic and moral support needed to attack the broad questions involved. Thank you for providing me the freedom and resources needed to complete field based experiments that I will never forget. I would also like to extend my sincere gratitude to my PhD committee members Drs. Claude Duguay (Geography and Environmental Management), Chris Dersken (Environment Canada), and Tony Endres (Earth Science) for their continued support. Thank you to my external thesis examinor Dr. Michael Durand (The Ohio State University) for his role in improving this thesis. Additional thanks to Drs. Peter Deadman, John Kovacs, and David Robotham for providing me with my first research opportunities. Thank you to the National Sciences and Engineering Research Council of Canada, Ontario Graduate Scholarship, and University of Waterloo for their sustaining financial contributions.

Thanks to the many friends I've made during my PhD. In particular, Niina Luus, Andrew Kasurak, Raymond Cabrera, Nic Svacina, Kevin Kang, Miranda Lewis, Grant Gunn, Patrick Nicholson, Michelle Rutty, Ryan Sim, Ryan Ahola, and Derrick Hambley.

Most importantly, thank you to my family: Kelly McLean, Catherine Morabito-King, Bob King, Nick King, and Jun Deng. This thesis is as much yours as it is mine. Your support throughout my life has given me the confidence to finish what I started.

Table of Contents

List of Tables

List of Figures

List of Abbreviations and Nomenclature

χ	Electrical susceptibility
Δ_{total}	Total error in estimation of σ^0
Γ_{cal}	Multiplicative bias errors
Γ_{res}	Residual multiplicative calibration errors
κ	Thermal conductivity
λ	Wavelength
ρ	Density
σ_h	Roughness criterion
τ	Relaxation time
ε''	Imaginary component of complex relative permittivity
ε_0	Permittivity of free space (Vacuum)
ε_r	Relative permittivity
ε	Permittivity
ε'	Real component of complex relative permittivity
ζ	Snow depth
A	Radar illuminated area
C	Specific heat

c	Speed of light (299,792,458 m s^{-1})
C_{ice}	Specific heat of ice
C_s	Specific heat of snow
D	Electric displacement field
E	Electric field
F	Farad
f_0	Relaxation frequency
G	Antenna gain
H_{a}	Antenna height
H_{p}	Positioner height
i	Imaginary number
k	Boltzmann's constant
k_{eff}	Effective thermal conductivity
n	Viscosity
N_{ind}	Number of independent samples
P	Water-equivalent precipitation
P_r	Power received
P_t	Power trasmitted
Q_s	Rate of saltation
Q_t	Rate of turbulent-suspenetion
Q_v	Rate of sublimation
R	Range
r	Molecular radius
R_{b}	Antenna-positioner phase center offset

R_y Antenna-mounting phase center offset

T Temperature

x_a Absorption coefficient

CLPX Cold Land Processes Experiment

CoReH$_2$O Cold Regions Hydrology High-Resolution Observatory

EM Electromagnetic

ESA European Space Agency

ET Equi-temperature

FMCW Frequency modulated continuous wave

IEEE Institute of Electrical and Electronics Engineers

IGOS Integrated Global Observing Strategy

NASA National Aeronautics and Space Administration

NOAA National Oceanic and Atmospheric Administration

POLSCAT Polarimetric scatterometer

Radar Radio detection and ranging

SCE Snow cover extent

SCR Signal-to-clutter ratio

SLCP Snow and Cold Land Processes

SNR Signal-to-noise ratio

SWE Snow water equivalent

TG Temperature gradient

Statement of Contributions

In addition to introductory chapters, this thesis contains three articles that are collaborative efforts which been accepted or submitted for publishing in peer-reviewed journals. The first paper has been published in *IEEE Geoscience and Remote Sensing Letters* and is presented as chapter 4 of this thesis. A IEEE copyright waiver can be found in the appendices of this document. The second paper has been submitted for review to *Remote Sensing of Environment* and is presented as chapter 5 of this thesis. The submitted manuscript has been assigned the reference of RSE-D-13-01044. The third paper has been submitted for review to *Journal of Glaciology* and is presented as chapter 6 of this thesis. The submitted manuscript has been assigned the reference of 14J020

Materials constituting each of the included journal articles were created in their original format by the author of this thesis in the capacity of the primary investigator. The final format of each paper is a direct result of collaboration with the listed coauthors. Chapter 4 was a collaborative effort between Joshua King and coauthors Richard Kelly, Andrew Kasurak, Grant Gunn, Claude Duguay and James Mead. Field-based methodologies presented in chapter 4 were developed Joshua, Andrew, and Richard. Data collections in Churchill were completed by Joshua, Andrew, Richard, Grant, and Claude. The scatterometer hardware was built by James Mead and Prosensing Inc. Original block diagrams of the scatterometer hardware presented in the appendices of this document were created by James Mead. The scatterometer signal processing software was a collaborative effort between Joshua King, James Mead and Prosensing Inc. The original written manuscript and diagrams contained in chapter 4 were created in their entirety by Joshua and edited by the coauthors.

Chapter 5 was a collaborative effort between Joshua King and coauthors Andrew Kasurak, Richard Kelly, Grant Gunn, and Claude Duguay. Field-based methods were developed by Joshua, Andrew, and Richard. Field data collections were completed by Joshua, Andrew, Richard, Grant, and Claude. Data analysis methods and discussion presented in chapter 5 was completed by Joshua. The original written manuscript and diagrams contained in chapter 5 were created in their entirety by Joshua and edited by the coauthors. In addition to the listed coauthors Chris Derksen of Environment Canada provided an external review of manuscript prior to submission.

Chapter 6 was a collaborative effort between Joshua King and coauthors Richard Kelly, Andrew Kasurak, Grant Gunn, Claude Duguay, Nick Rutter, Tom Watts, and Chris Derksen. The scatterometer measurement protocol was developed by Joshua, Richard, and Andrew. The trench excavation and processing of near infrared photography was completed by Nick and Tom. Field data collections were completed by Richard, Andrew, Grant, Claude, Nick Rutter, Tom Watts, and Chris Derksen. The original written manuscript and diagrams contained in chapter 6 were created in their entirety by Joshua and edited by the coauthors.

The undersigned are in agreement with the evaluation of the roles and contributions of the authors listed in the preface

	January 6, 2014
Richard Kelly	Date

	January 14, 2014
Andrew Kasurak	Date

	January 9, 2014
Grant Gunn	Date

	January 6, 2014
Claude Duguay	Date

	January 7, 2014
James Mead	Date

	January 7, 2014
Nick Rutter	Date
	January 13, 2014
Tom Watts	Date
	January 6, 2014
Chris Derksen	Date

Chapter 1

General introduction

1.1 Motivation

Snow is a significant seasonal component of the cryosphere with a vast Northern Hemisphere maximum extent of nearly 50 million km^2. Variability at multiple scales in the duration, extent, and mass of seasonal snow over land can have profound implications for sensitive hydrological and climate systems. Once deposited, the optical and thermal properties of snow exert considerable control on terrestrial exchange of heat and energy by effectively decoupling atmosphere and soil boundary conditions (Zhang, 2005). As a result, an inherent relationship exists between snow and climate where properties including high albedo serve to maintain lower surface temperatures. Conversely, when absent or limited in extent, a positive feedback may occur where surface temperatures increase and the capacity of seasonal snow to persist is diminished. An increasing number of studies have drawn attention to strong linkages between recent Arctic warming and reductions in spring snow cover extent (SCE) (e.g. Brown et al., 2010; Chapin et al., 2005; Derksen and Brown, 2012;

Dye, 2002; McCabe and Wolock, 2010). Over the last 30 years, June SCE has decreased at a rate of nearly -20% decade^{-1}, exceeding the widely publicized decline in September sea ice extent by a substantial margin (Figure 1.1, Derksen and Brown, 2012). In addition to its role in the climate system, snow is an important storage of fresh water where Arctic snowmelt accounts for up to 90% of annual flow and across the Northern Hemisphere is a dominate component of regional run off (Barnett et al., 2005; Pomeroy et al., 2006). Changes to accumulated mass can threaten communities dependent on seasonal snow for fresh water security and overland travel. Moreover, sensitive ecosystem functions including net exchange have been shown to respond to changing terrestrial snow conditions (Luus et al., 2013).

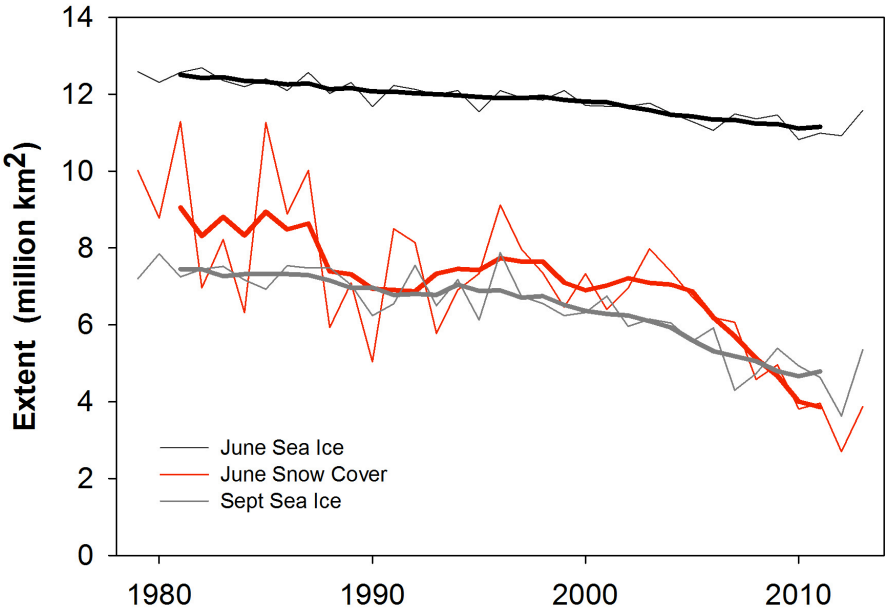

Figure 1.1: Northern Hemisphere June snow cover and September sea ice extent. Snow cover extent time series was derived from the NOAA snow chart climate data record (Modified and updated from Derksen and Brown, 2012).

Improving global capacity to characterize spatiotemporal variability in local snow properties is an important step towards advancing understanding of the role of snow in multi-scale climate systems and regional hydrology. Existing ground-based networks for measurement of key properties including depth, density, and snow water equivalent (SWE) lack sufficient spatial density to characterize seasonal changes at scales of ground observed variation (Derksen et al., 2005; Dyer and Mote, 2006). In Canada, snow depth measurements have been made at most synoptic weather stations since the 1950's, but are generally limited by proximity to populated areas (Figure 1.2, Brown et al., 2003; Rees et al., 2013). Lack of snow information is an important issue in the Canadian Arctic where a very small number of measurement stations are used to characterize a very large spatial domain. In the Northern Hemisphere, now cover types common to the Arctic constitute more than 20% of non-ephemeral seasonal cover (Table 1.1). Moreover, tundra snowpack found in these areas are characterized by significant spatial variability relative to other snow types making measurement difficult and monitoring of seasonal variability a challenge with the current ground-based observation networks (Brown et al., 2010; Liston, 2004; Rees et al., 2013).

Widespread lack of *in situ* snow measurements have made readily available satellite observations an attractive alternative for monitoring of large spatial domains including Arctic and sub-Arctic regions. Practical examples of advancement in the observation of Northern Hemisphere snow cover extent (SCE) are abundant (e.g. Brown and Robinson, 2011; Hall et al., 2010), but substantial challenges persist in satellite-based retrieval of volumetric snow properties (e.g. Derksen, 2008; Foster et al., 2005; Kelly et al., 2003). The Integrated Global Observing Strategy (IGOS) has recognized the limitations of current methods and advised that novel satellite sensors capable of snow hydrology observations at scales of ground observed variation ($<$ 200 m) receive priority (IGOS, 2007). In this

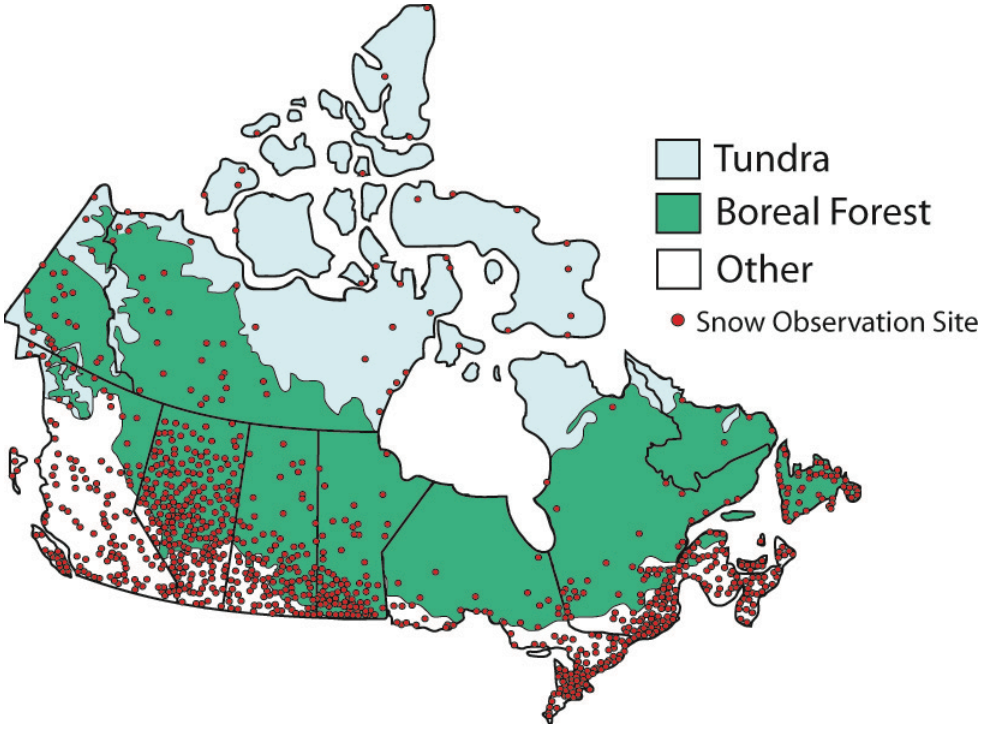

Figure 1.2: Distribution of snow depth monitoring sites (Modified from Rees et al., 2013).

regard, active microwave remote sensing (e.g. radar) has emerged as a strong complement to existing methods and a potential catalyst for advancement. Radar systems at frequencies between 8 and 18 GHz penetrate dry snow to substantial depths providing all-weather, time independent observation of volumetric snow processes. In 2005, the European Space Agency (ESA) Earth Explorer candidate mission CoReH$_2$O (Cold Regions Hydrology High-Resolution Observatory for Snow and Cold Land Processes) proposed a dual-frequency (17.2 and 9.6 GHz) synthetic aperture radar for observation of cryospheric variables including snow at high spatial resolutions ($\leq$ 50 m x 50 m). Despite international support for CoReH$_2$O and radar-based retrieval of snow properties, few studies have evaluated the seasonal Ku- and/or X-band response of terrestrial snow. Additionally, no previous studies have attempted to do so in tundra environments. An opportunity exists to

Table 1.1: Area and percentage of Northern Hemisphere snow distribution categories excluding Greenland and ephemeral snow covers (Modified from Liston, 2004).

Category name	Area (10^6 km^2)	Percentage
Mid-latitude, non-mountainous forest	3.4	6.9
High-latitude, non-mountainous forest	8.0	16.2
High-latitude, mountainous forest	2.2	4.5
Arctic tundra	10.8	21.8
Mid-latitude prairie	14.2	28.7
High-latitude, mountainous forest	2.3	4.7
High-latitude, mountainous	3.7	7.4
Mid-latitude, treeless mountains	4.9	9.8

evaluate the seasonal and spatial response of tundra snow at Ku- and X-band to address gaps in understanding of field observed interaction and to support the present need for innovative methods of snow property retrieval.

1.2 Objectives

The primary goal of this thesis is to improve knowledge of snow-microwave interactions with analysis of field-based measurements collected in a Canadian tundra environment. As an intermediary towards robust satellite-based retrieval of snow properties, an attempt was made to answer the question: (1) Does Ku- and/or X-band (17.2 and/or 9.6 GHz) backscatter show sensitivity to evolving dielectric and physical properties of terrestrial tundra snow? Additionally, (2) what role do spatiotemporal processes of accumulation and metamorphosis play in evolving backscatter signatures? These questions were approached with a set of three objectives:

1. Demonstrate proof-of-concept methodology and experimental results for deployment of a sled-mounted dual frequency scatterometer system in a previously untested tundra environment

2. Characterize the seasonal response of snow covered terrain using repeat coincident meteorological, snow, and backscatter measurements to assess the influence of local processes of accumulation and metamorphosis without disturbing the natural snowpack

3. Evaluate the influence of spatial variability and lateral heterogeneity on backscatter response using measurements collected from a distributed set of snow covered terrestrial sites with detailed snow surveys completed within the instrument field of view.

1.3 Structure

This manuscript-based thesis is structured with seven chapters to provide relevant background information and field-based experiments to address each of the identified study objectives. This preliminary chapter introduces rationale and objectives of the study, outlining the need for advancement in understanding of tundra specific radar-snow interactions. Chapter two provides a review of thermodynamic and physical processes key in the the development of terrestrial snow, while chapter three connects introduced snow processes to backscatter response by providing the background on radar theory and measurement principles.

Chapter four addresses the first objective of this thesis with introduction of the University of Waterloo Scatterometer (UW-Scat) system and by providing examples of its inaugural deployment near Churchill, Manitoba, Canada. This chapter has been published in the peer reviewed journal *IEEE Geoscience and Remote Sensing Letters*:

> King, J., Kelly, R., Kasurak, A., Gunn, G., Duguay, C., and Mead, J. (2013). UW-Scat - A ground-based dual frequency scatterometer for observation of snow properties. *IEEE Geoscience and Remote Sensing Letters*, 10(3), 528-532.

Chapter five addresses the second objective of the thesis with comparative analysis of seasonal backscatter and snow property measurements collected at an undisturbed tundra observation site near Churchill, Manitoba Canada. Chapter five has been submitted for peer review to the journal *Remote Sensing of Environment*:

> King, J., Kasurak, A., Kelly, R., Gunn, G., and Duguay, C. (2013). Seasonal scatterometer observations of a shallow tundra snowpack. *Remote Sensing of Environment*, in review, RSE-D-13-01044.

Chapter six addresses the final objective of the thesis presenting a spatially distributed set of snow covered tundra backscatter responses. This chapter also contains a case study exploring the use of enhanced trench sampling methods to compare high resolution stratigraphy against coincident radar returns. Chapter six was submitted for peer review to the *Journal of Glaciology*:

> King, J., Kelly, R, Kasurak, A., Duguay, C., Gunn, G., Rutter, N., Watts, T., Derksen, C. (2014). Spatiotemporal influence of tundra snow properties on Ku-band (17.2 GHz) backscatter. *Journal of Glaciology*, in review, 14J020.

The final chapter provides a summary of findings and limitations, as well as suggestions for future direction of applied research and field study. Chapters containing published or in-review material have been included in their original format as they are subject to copyright. This may result in some repetition of introductory material, fundamental equations and common field methodologies.

Chapter 2

Seasonal dry snow in terrestrial environments

Snow is thermodynamically unstable and undergoes rapid structural change throughout its lifespan (Colbeck, 1982a; Pinzer and Schneebeli, 2009). Due to this, it must be understood as a dynamic medium affected by numerous spatial and temporal processes. This chapter introduces seasonal processes responsible for the physical and thermodynamic state of terrestrial seasonal snowpack. Precipitation, transport, and metamorphosis are discussed to conceptualize the seasonal evolution of bulk and stratigraphic dry snow properties. Summation of this discussion will provide the necessary knowledge to deconstruct seasonally observed snow state and identify features of interest specific to tundra environments.

2.1 Accumulation

The Earth's atmosphere is host to quantities of water vapour which when condensed form clouds and ice particles (Jordan et al., 2008). Under certain conditions, ice particles grow and fall to the Earth's surface forming terrestrial accumulation often desrcibed as snowpack. Atmospheric inhomogeneities of vapour and temperature govern the process of precipitation and the range of possible snow crystal structures (Libbrecht, 2005).

2.1.1 Precipitation

A snow crystal, more commonly known as a snowflake, begins as ice crystal growth in response to the deposition of water vapour (Libbrecht, 2005). The process of growth includes a series of atmospheric interactions meeting four primary requirements: (1) the presence of water vapour, (2) relative humidity of 100%, (3) air temperature below 0°C, and (4) the presence of a nucleating agent (Berry and Maxwell, 1981; Jordan et al., 2008; Serreze and Barry, 2005).

Atmospheric moisture exists as a multi-phase equilibrium of water droplets, vapour, and ice particles. Presence and concentration are determined by air temperature and regional flow of moisture. The latter is driven by processes of air mass movement while the former determines total water vapour as a function of air mass saturation (Ahrens, 2007; Berry and Maxwell, 1981). Consider here the equilibrium state of a suspended droplet of water where molecules evaporate and condense at an equal rate. The force exerted by the evaporate above the droplet surface is known as the actual vapour pressure. As temperature increases, energetic molecules readily escape the liquid surface. The resulting increase of molecules above the surface exerts an additional force increasing vapour pressure. Conversely, a decrease in temperature lowers pressure as molecules are less likely to escape. Condensation

occurs where molecules of lower energy collide with the droplet surface. The pressure at equilibrium is known as the saturation vapour pressure. Coupled with vertical air mass movement, the decrease in temperature creates the supersaturated conditions needed for precipitation.

In sub-zero temperature clouds, ice nucleation occurs when water vapour comes into contact with a surface. These surfaces, known as nucleating agents, are found as suspended clays, bacteria, and aerosols (Hoose, 2010). In very cold clouds, spontaneous nucleation of supercooled water droplets may occur when temperatures are below -36°C. These processes are known as heterogenous and homogenous nucleation and, as a whole, compose the Bergeron process. Once nucleated, ice particles begin to grow by processes of accretion, aggregation, and vapour diffusion. Accretion is the contact deposition of supercooled water on ice particles as they move within a cloud. Aggregation occurs when ice particles collide forming larger masses at which point become known as snow crystals. Finally, vapour diffusion occurs as water deposits onto the ice particles due to their lower saturation vapour pressure.

Crystal shapes formed in the atmosphere vary from simple hexagonal columns and plates to complex tree like structures known as dendrites. Nakaya (1954) was the first to observe snow crystal growth in a laboratory setting, and developed a morphology diagram to explain observed variations in structure (Figure 2.1). As crystals grow and accumulate mass, they overcome suspension in the atmosphere and begin to fall. This transit subjects the crystallization to variations in temperature and saturation, producing the unique attributes of individual snow crystals. Under supersaturated conditions, the iconic snow flake is created as vapour diffuses to each of the six points of an ice particle producing the distinctive dendritic pattern.

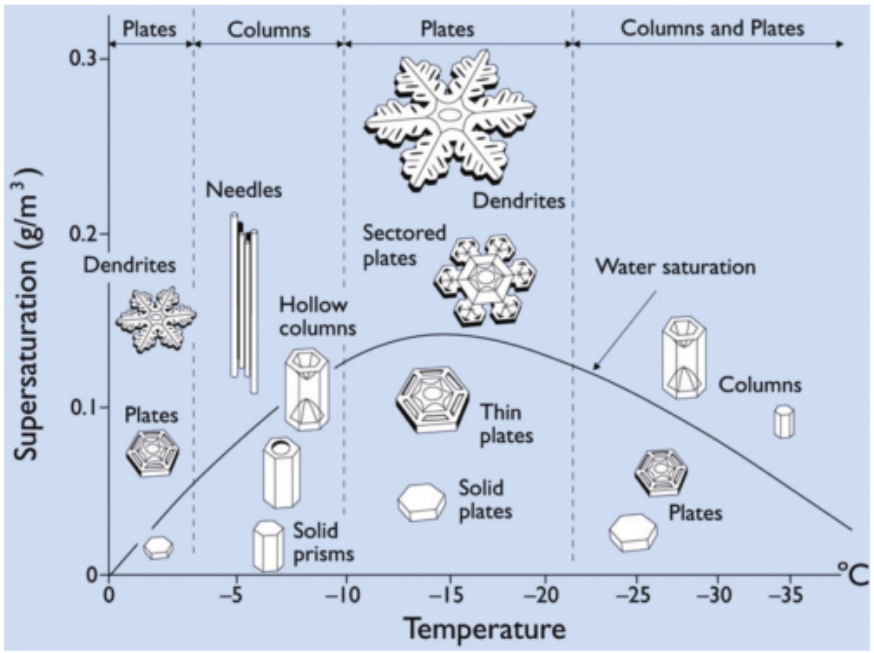

Figure 2.1: Snow crystal morphology (Modified from Libbrecht, 2005)

2.1.2 Deposition, transport, and stratification

Precipitation reaching the surface is deposited and redistributed according to local variations (< 200 m) in topography, wind, and vegetation (Liston, 2004; Pomeroy et al., 1997; Woo, 2012). Each physical and environmental attribute exerts significant control on depth and determines the initial characteristics of snowpack layering otherwise know as stratigraphy. At regional scales, common land cover composition and climatic regime create distinctive snow cover types with prevalent features over scales of tens to hundreds of kilometres (Derksen et al., 2009).

Snow transport models provide an accessible means of description for interactions amongst local factors influencing distribution (Liston and Sturm, 1998; Pomeroy et al., 1993, 1997; Purves et al., 1998). Liston and Sturm (1998) describe the physical processes

of distribution or redistribution as changes in snowpack mass balance. Spatial and temporal variations in snow depth (ζ) result from change in horizontal mass-transport rates of saltation (Q_s), and turbulent suspension (Q_t). Moreover, rates of sublimation (Q_v), and water-equivalent precipitation (P) contribute to mass input and output:

$$\frac{d\zeta}{dt} = \frac{1}{\rho_s}\left[\rho_w P - \left(\frac{dQ_s}{dx} + \frac{dQ_t}{dx} + \frac{dQ_s}{dy} + \frac{dQ_t}{dy}\right) + Q_v\right] \tag{2.1}$$

where, x and y are coordinates in meters, t time in seconds, ρ_s snow density, and ρ_w water density. Wind transport is divided among three components: creep, saltation, and suspension. Creep is low velocity transport where snow crystals roll along the surface. Increasing wind speed begins the process of saltation where particles are transported just above the surface in a skipping action (Pomeroy et al., 1993). The impact of particles causes splintering, adding to the saltation volume. Moreover, crystals transported by saltation are subject to structural change due to sublimation and abrasion (Pomeroy and Gray, 1990). This type of transport constitutes the bulk of wind blown snow and can result in significant losses of mass due to sublimation. Finally, suspension is the movement of snow crystals by atmospheric turbulence. Saltation is required for turbulent suspension and forms the lower bound of its transport rate (Liston and Sturm, 1998). These processes are all affected by wind speed which dictates the height and volume of transportation. Variability in local wind plays a substantial role in the mass balance equation as it drives changes in both depth and density. For example, newly fallen snow which ranges in density from 50 kg m^{-3} to 120 kg m^{-3}, can rapidly change by rate of up to 9 kg m^{-3} per hour during wind events (Pomeroy et al., 1998). Rounding of grains as part of the process of wind transport drive rapid increases in snowpack density. Under sustained periods of wind action density can exceed 300 kg m^{-3} forming crusts known as wind slab.

Blowing snow dominates redistribution and is a controlling factor of seasonal snowpack evolution in open areas (Pomeroy et al., 1993). Tundra environments in the Canadian Arctic are subject to sustained northerly winds which rapidly redistribute and sublimate accumulation. Variation in vegetation structure and topography are also important attributes governing snowpack structure as they promote trapping of snow and sheltering from wind processes. Areas with standing vegetation such as shrubs, willows, and trees, generally trap more accumulation than graminoid dominated areas. In open Arctic and sub-Arctic environments, the limited height of graminoid vegetation does not provide sufficient surface roughness to counter the influence of wind redistribution. Therefore, snow depth is generally limited to the height of the short surface vegetation (e.g. < 30 cm in open tundra environments; Derksen et al., 2012b; Pomeroy and Li, 2010). Snow redistributed from open areas will accumulate where changes in topography or vegetation allow reduce wind velocity such as valleys or at the edge transition zones. Depositions found here constitute significant increases from the local mean known as drifts.

2.2 Dry snow metamorphosis

Once deposited, snow grains are found in a continuous state of transformation because of their presence near the triple point temperature of water (Colbeck, 1982a; Fierz et al., 2009; Miller and Adams, 2009). Seasonally observed changes in snowpack properties due to this are known as metamorphism. In dry snow, vapour transport and subsequent grain growth are the primary processes of metamorphism (Sturm and Benson, 1997). Common to each is regulation of the governing physical processes by snowpack temperature. As a result, seasonal metamorphic processes can be understood as a product of evolving snow thermodynamics and external environmental forcing.

Snow is an efficient thermal insulator as quantified by its low thermal conductivity (k). It is typical in snow to estimate this property as a measure of effective thermal conductivity (k_{eff}) in units of watt per meter Kelvin (W m^{-1} K^{-1}) by considering the heat transport mechanisms associated with solid, liquid, and vapour phases (Sturm et al., 1997). The k_{eff} of snow is driven by ice lattice conduction, pore space conduction, and latent heat transport occurring across the pore space. To a much lesser extent, radiative and convective heat transports also contribute to k_{eff}. In general, k_{eff} has a positive relationship with density and the development of a well bonded ice lattice (Yen, 1962). An empirical estimate of k_{eff} with known density can be as (Sturm et al., 1997):

$$\kappa_{eff} = \begin{cases} 0.0138 + 1.01\rho + 3.233\rho^2 & \{0.156 \leq \rho \leq 0.600 \text{ g cm}^{-3}\} \\ 0.023 + 0.234\rho & \{\rho < 0.156 \text{ g cm}^{-3}\} \end{cases} \tag{2.2}$$

From equation 2.2, density is found to exert influence on thermal conductivity over a wide range of k_{eff} (Figure 2.2). As snow density increases towards the density of ice ($\approx$ 916 kg m^{-3}), pore space is reduced and k_{eff} approaches values similar to ice itself ($\approx$ 2.18 W m^{-1} K^{-1}). In addition to density, k_{eff} is influenced by grain properties within the snowpack. Recent studies have demonstrated anisotropy of thermal conductivity as related to grain type in addition to density (Domine et al., 2013; Riche and Schneebeli, 2013).

The specific heat of snow (C_s) is also an important parameter in the transport of heat. The physical quantify of C_s describes the heat required for a unit mass to change in unit temperature in units of Joule per kilogram Kelvin (J/kg $\cdot$ K). As the C of air occupying inter-granular pore space is negligible, C_s is assumed be based on pure ice (C_{ice} = 2113 J/kg $\cdot$ K) (Mellor, 1977). Furthermore, effective C_{snow} is dependent on temperature and impurities within the ice matrix. In general, C_{snow} rises with temperature, demonstrating

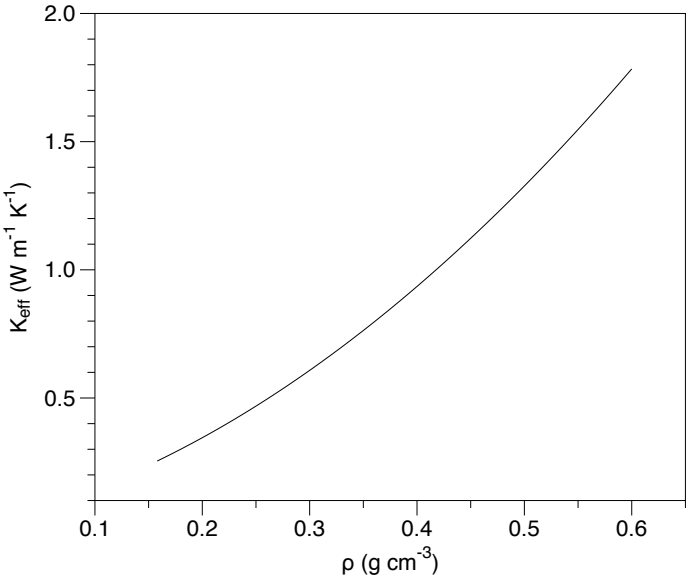

Figure 2.2: Effective thermal conductivity (k_{eft}) of snow as a function of density ρ (Based on equations from Sturm et al., 1997)

an increased requirement for energy and diminishing storage capacity. While empirical models exist, Mellor (1977) states that C_s can be approximated as 2120 J/kg $\cdot$ K. Snowpack specific heat is related to k_{eff} by thermal diffusivity (α):

$$k_{eff} = \rho C_s \alpha \tag{2.3}$$

In this relationship, increasing α dictates that a volume will conduct heat more rapidly. Snowpack responds by readily adjusting temperature in response to surrounding conditions. Thus, spatial differences in temperature coupled with significant α cause for movement of energy. Understanding the gradient of heat transport developed here is useful because, along with grain curvature, it identifies the conditions necessary for snow crystal growth.

2.2.1 Equi-temperature metamorphism

Equi-temperature (ET) metamorphism refers to changes in snowpack microstructure under isothermal conditions (Colbeck, 1980). Fresh accumulation, near surface layers, and snowpack where the air-soil temperature gradient is small, are conditions under which ET metamorphism is typical. This processes is also known as destructive metamorphism (e.g. Colbeck, 1982a, 1983; LaChapelle, 1969) and the resulting re-crystallizations as equilibrium form (e.g. Colbeck, 1982a, 1986). The common terminology "destructive" refers to the tendency of snow crystals to reduce their surface to volume ratio as they approach thermodynamic equilibrium under an ET regime.

Low temperature gradients under isothermal snowpack conditions are dominated by curvature-driven diffusion. The diffusion of water vapour under these conditions is described by Kelvin's Law (Arons and Colbeck, 1995; Colbeck, 1980):

$$p = p_s \exp \frac{2\gamma_i}{R_v T \rho_i r} \tag{2.4}$$

where, p is the saturation vapour pressure of a planar surface on the particle (in units of Pa), γ_i is the surface tension of ice in (units of kg $\cdot$ s^{-3}), ρ_i is the density of ice (in units of kg m^{-3}), T is temperature (in units of K), r is the particle radius. The law describes a standard relationship between snow crystal curvature and diffusion of vapour resulting from surface sublimation or deposition. Here, convex surfaces readily sublimate to meet equilibrium vapour pressure. Pointed crystal structures such as dendrite arms are readily depleted by this process. A rounded quality in snow grain structure is observed with ET metamorphism from these processes.

Figure 2.3 shows a conceptual snow grain evolution under ET metamorphism. The ET process shown here occurs at a long temporal scale, on the order of tens of days (Colbeck, 1980). As changes in snowpack temperature occur at much shorter scales (e.g. hours), isolated destructive metamorphism is rare under natural conditions. Mixed state layers are more common where multiple active processes define snow crystal metamorphosis (Colbeck, 1982a). In this context, recent research by Pinzer and Schneebeli (2009) has shown that the presence of rounded grains may cause for misinterpretation of active grain growth processes. By applying cycled temperature gradients of large amplitude, significant displacements of mass are possible while maintaining ET typical rounded grain shapes. Due to this identification of metamorphic processes is ideally completed with local scale climatic information in addition to visual interpretation.

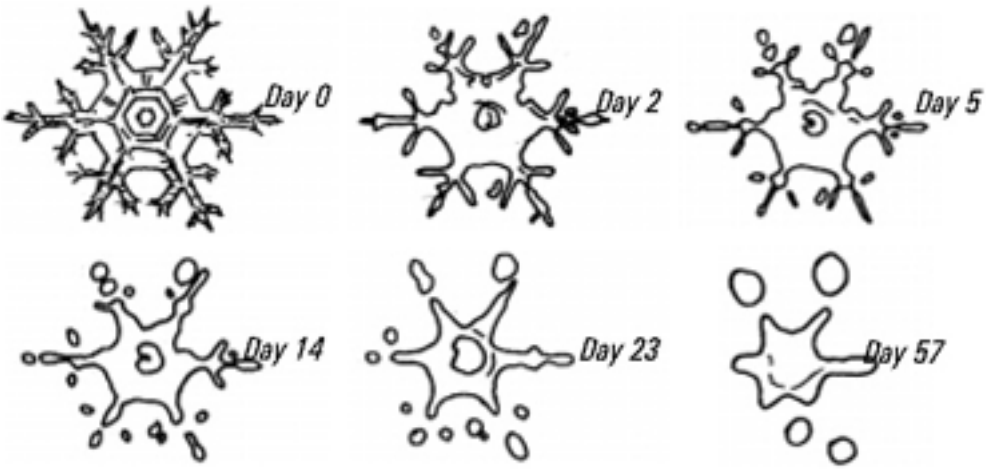

Figure 2.3: Destructive metamorphism of snow (Modified from LaChapelle, 1969)

The snow properties common to ET metamorphism can be summarized as increased density with rounding and compaction of individual grains. Additionally, under ET metamorphism grain size is generally maintained, despite increasing density. Vapour diffusion

dictates the movement of mass within the snowpack and without a significant gradient, distances of travel are small and grain size is conserved. Finally, ET metamorphism processes is also often accompanied by bonding of the ice lattice from associated processes of sintering.

2.2.2 Temperature gradient metamorphism

A vertical temperature gradient (TG) in excess of 10°C m^{-1} and available moisture within the snowpack are the general conditions required for kinetic grain growth. Under these conditions, faceted snow grains develop at a rate of growth proportional to the magnitude of the vertical TG (Armstrong, 1980; Colbeck, 1983). Subarctic winter snowpacks often have strong vertical temperature gradients with a concave shape because of sustained low air temperatures and shallow depth (Sturm and Benson, 1997; Sturm and Johnson, 1991; Taras et al., 2002). Under a sharp TG, physical snow temperatures are greatest near the bottom of the snowpack because of the aforementioned significance of thermal conductivity. Development of faceted crystals as a result of TG metamorphism is common to lower bounds of terrestrial snowpack where significant vapour transport produces the grain type know as depth hoar (Figure 2.4).

Yosida (1955) describes a "hand to hand" model whereby vapour transport under a TG regime is defined by deposition on concave grain surfaces in the direction of transport and sublimation from convex surfaces oriented in the opposite. Imbalances of transport by this process result in net gain or loss of mass ultimately realized as the physical process of grain growth. As a result of these imbalances, the number of grains under TG metamorphism is consolidated, thereby reducing density while maintaining equilibrium of mass. The movement of heat in this system is dependent on the previously discussed k_{eff} of snow.

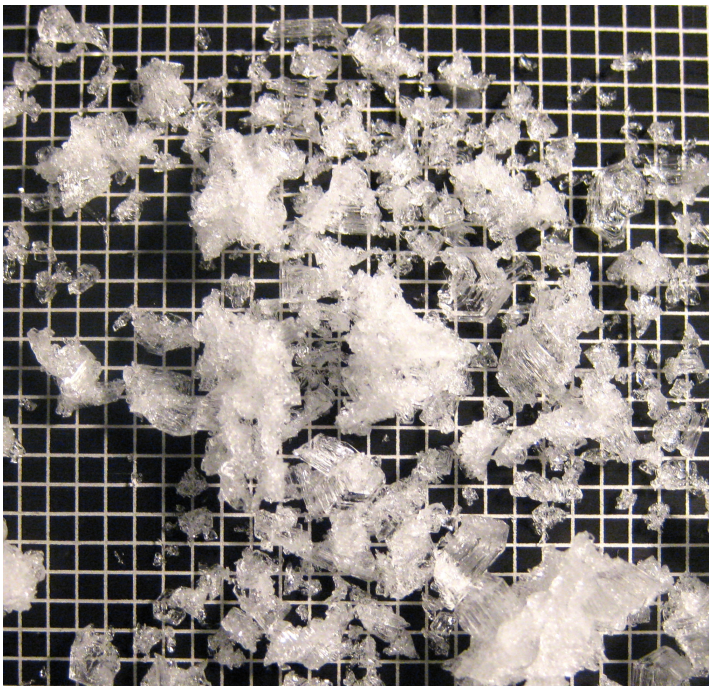

Figure 2.4: Depth hoar and snow grain aggregations resultant from temperature gradient metamorphosis. Grains were extruded from a mid-season tundra snow pack and are shown on a 2 mm grid.

Under a TG regime the primary component of heat transfer is latent heat across the pore space. Increasing porosity from grain consolidation provides the necessary air volume for this to occur as vertical flux. Heat is conducted through the ice lattice because of its increased conductivity relative to air. Due to this, protrusions of individual grains form cold spots where deposition or condensation can occur. In vapour limited snowpack, crystals will compete in this process to reach equilibrium. Diurnal cycling and spatial changes in the TG regime produce iterative periods of metamorphism and crystal striations. The resulting faceted crystals often diverge from random arrangement to form vertically preferential structures along the axis of vapour transport (Adams and Miller, 2003; Miller and Adams, 2009).

This brief overview of TG metamorphism does not address the formation of faceted layers above and below crusts (Colbeck and Jamieson, 2001; Domine et al., 2009), the aggregation effects of bonding (Colbeck, 1983; Legagneux et al., 2004), or wind slab conversion (Derksen et al., 2009). While important, these processes are complex warranting lengthy discussion. Despite this, the above discussion identifies several seasonally relevant metamorphic processes for the development of tundra snow.

2.3 Tundra snow

Periods of low air temperature, little precipitation, and high wind speed are the conditions needed for the development of tundra class snow and are common to Arctic regions. Tundra snow is characterized by its thin, wind influenced structure and typical composition of basal depth hoar layer overlain with multiple higher density wind slabs (Liston, 2004; Sturm et al., 1995). Depth in open tundra environments is generally limited by the lack of standing vegetation and exposure to sustained winds (see Table 2.1 for examples). When exposed to wind, snow is removed by processes of saltation or sublimation. Rapid redistribution of accumulation and wind rounding of grains produces layered wind slab features which vary in number and density by variations in wind speed and precipitation. Contrasting basal depth hoar develops as a result of sustained exposure to cold air temperatures and subsequent steep vertical temperature gradients through the shallow snowpack. Seasonally, temperature gradient metamorphosis and the development of depth hoar can be near continuous with grain sizes exceeding 6 mm in major axis length prior to snow melt. As a product of depth and density, tundra SWE is limited by the narrow range of depth encountered. In comparison to other snow cover types, only prairie snowpack where vegetation heights are lower, tend to have lower average SWE.

Table 2.1: Examples of nominal tundra snow properties

	Sturm et al. (1995)	Derksen et al. (2009)	Rees et al. (2013)
Region	Alaska	Canadian subarctic	Daring Lake, NWT
Depth (cm)	10–75	30–40	< 75
Density (kg m^{-3})	380	350	293
SWE (mm)	38–266	114-152	< 220

2.4 Summary

In this chapter, principles of dry snow accumulation, transport, and metamorphosis were reviewed for terrestrial environments. Thermodynamically unstable and subject to environmental forcing, snow is in a constant state of change. Beginning as atmospheric moisture, snow crystals develop from a complex set of interactions involving variation in temperature, moisture, and path of transit. Once on the ground, snow grains continue to change as wind transport and other external agents modify physical structure and thermodynamic properties of terrestrial snowpack. Successive iterations of accumulation, transport, and metamorphism lead to the development of distinctive snow cover properties and intricate layering of dynamic snow grains.

In tundra environments, sustained wind and lack of standing vegetation limit depth and SWE. Although shallow, tundra snow is a challenging target of analysis given its rapid but often subtle changes in structure related to wind transport and temperature gradient metamorphosis. The seasonal development of features including wind slab and depth hoar distinguish tundra snow from other snow cover types. Metamorphic processes present in tundra snow are important and have implications in remote sensing across a wide electromagnetic spectrum including microwaves (Fierz et al., 2009; Legagneux et al., 2004; Schwander et al., 1999). In the context of radar remote sensing, changes in the

physical attributes of snow over time will be represented by proportional changes in observed backscatter. This assumption forms the basis of radar snow property retrieval to be discussed at length in the following chapter.

Chapter 3

Radar remote sensing of snow

In active microwave remote sensing, energy returned from target media is known as backscatter. Changes in the dielectric and physical properties of a target can generate variations in backscatter which contain information about surface and volume interactions analogous to *in situ* sampled properties (Ulaby et al., 1981). In the context of terrestrial snow, seasonal processes of accumulation and metamorphosis drive backscatter variability related to evolving volumetric properties including depth, density, and SWE. Properties of the observing instrument such as wavelength, polarization and incidence angle also play a significant role in observed backscatter through dependent processes of scattering and absorption (Ulaby et al., 1984). Evaluation of backscatter response from snow covered terrain requires integrated knowledge of both the transmitting sensor and target properties to identify and separate snow scattering contributions from other signal sources (Shi and Dozier, 2000). In this chapter, microwave theory is introduced to elucidate interactions fundamental to the retrieval of tundra snowpack properties. The discussion is developed with emphasis on interactions at Ku- and X-band (17.2 GHz and 9.6 GHz) under conditions synonymous with the development of tundra snow.

3.1 Principles of backscatter measurement

Electromagnetic (EM) waves are oscillating perpendicular electric and magnetic component fields traveling in transverse self-propagation. These waves can be described by their length, frequency, amplitude, phase, and polarization. In the EM spectrum, microwaves are found at wavelengths (λ) between approximately 0.01 and 1 m. Here, wavelength refers to the spatial period of the wave. Frequency (f), an inversely proportional measure of events per unit of time, is also a common means of description. Converted from wavelength, $f = c/\lambda$ where c is the speed of light (299,792,458 m s^{-1}).

Microwave remote sensing instruments described as "active" refer to those with an onboard source of illumination capable of both transmission and reception in the microwave spectrum. Basic functionality of this sensor type provides the means to operate at known frequency or wavelength. Such functionality is important for Earth observation where particular ranges within the microwave spectrum are optimal for specific media or land cover applications. In general, observation of terrestrial media requires wavelengths smaller than 30 cm ($f \geq 1$ GHz) to approximate the incident wavelength to desired process scale (Woodhouse, 2006). In this research, wavelengths of 1.7 and 3.1 cm (17.2 GHz and 9.6 GHz), corresponding with frequency bands designated as Ku and X have been selected. Microwaves within the selected range approach the process scale of individual snow grains (0.1 to 10 mm) promoting interaction while remaining able to penetrate the volume of terrestrial snowpack. In addition to frequency, it is often advantageous to control the polarization of the transmitted and received electric fields. Much like frequency, target specific polarization response is typical of terrestrial media and can be used to derive additional information about the target. The orientation of a polarized electric field is described relative to the direction of travel. Radar systems commonly use linear polarization

in either the vertical (v) or horizontal (h) plane. Transmission and reception in the same polarization is known as co-polarized (hh and vv). Reception of a polarized field which is different than the transmitted field is refereed to as cross-polarized (hv and vh). Fully polarimetric sensors, including those used in this thesis, are capable of transmitting and receiving all four linear polarization combinations (vv, vh, hv, and hh).

3.1.1 The radar equation

Active microwave sensors, namely radar, measure the intensity of a returned electric field relative to the initial transmission. The monostatic radar equation resolves power (P_r) returned to the sensor as:

$$P_r = \frac{P_t G^2 \lambda^2 \sigma}{(4\pi)^3 R^4} \tag{3.1}$$

where, R is range, G is antenna gain, λ is wavelength, and σ is cross-section of the target. Variables other than σ in equation 3.1 are defined by the operating parameters of the observing instrument. Thus, if sensor properties are held constant, solving for σ determines the targets influence on backscattered power. As the snow surface and volume are distributed targets, it is common to normalize σ by the radar illuminated area (A) such that

$$\sigma^0 = \frac{\sigma}{A} \tag{3.2}$$

which is related to the radar equation by:

$$\sigma^0 = \frac{\sigma}{A} = P_r \frac{(4\pi)^3 R^4}{A P_t G^2 \lambda^2} \tag{3.3}$$

Application of equation 3.3 in Earth observation assumes that the radar range to target is well defined for the estimation of σ^0 (Baumgartner et al., 2002). For satellite based observation, this assumption is valid as the range to target from the sensor is far greater than the depth of snow. In ground-based applications, where the distance to the snow surface is comparable to the depth of snow, an estimate of effective range (R_{eff}) is needed:

$$R_{eff} = R_s + \delta R \tag{3.4}$$

where R_s is the antenna range to the snow surface and δR accounts for radar penetration into the snow volume.

Power received at the observing antenna declines by the fourth power of range in equation 3.3. Increasing distance between the antenna and target responds as a logarithmic function, quickly declining to very small values of linear power. In practical application, linear power estimates of σ^0 are often converted to decibel units (dB) for analysis:

$$\sigma^0_{dB} = 10\log_{10}(\sigma^0) \tag{3.5}$$

3.2 Backscatter from snow covered terrain

Characterization and evaluation of physical and dielectric processes contributing to σ^0 is intrinsic to the development of snow property retrieval methods. In a snow covered terrestrial environment free of standing vegetation, total observed backscatter (σ^t) in a particular polarization combination (pq) is conceptualized as series of surface and volume contributions:

$$\sigma^t_{pq} = \sigma^{as}_{pq} + \sigma^v_{pq} + \sigma^{gv}_{pq} + \sigma^g_{pq} \tag{3.6}$$

where σ^{as} is scattering at the air-snow interface, σ^v is scattering from within the snow volume, σ^{gv} is scattering resulting from multiple interactions between ground and the snow volume, and σ^g is backscatter directly from the snow-ground interface (see Figure 3.1). The magnitude and relative contribution of each component in equation 3.6 is determined by the dielectric and geometric properties of the observed media, and the parameters of the observing instrument (frequency, wavelength, and polarization) (Ulaby et al., 1984). Processes of microwave absorption and scattering specific snow and soil components are governed by these factors which in turn determine the amount of energy returned to the observing sensor.

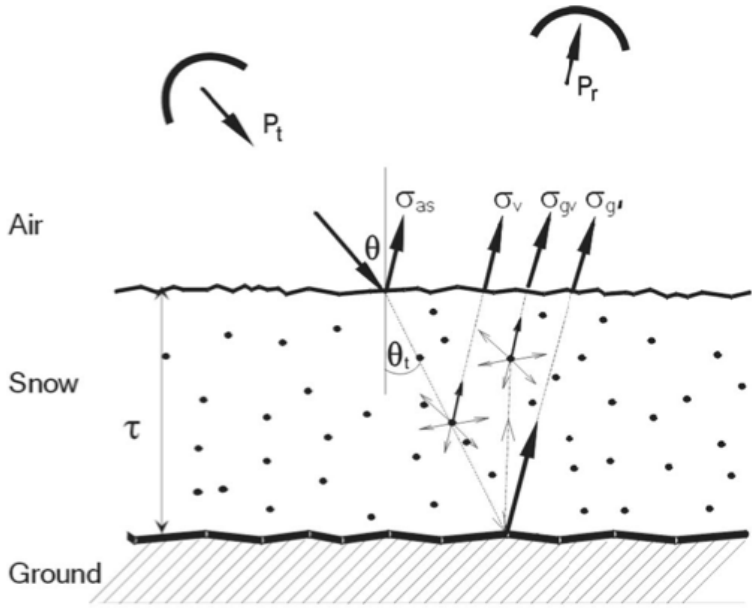

Figure 3.1: First-order scattering contributions from snow covered terrain (Modified from Rott et al., 2010). To improve diagram clarity, a bistatic radar configuration is shown where P_t is the transmitting antenna power and P_r is the receiving antenna power.

The remainder of this chapter will introduce processes of absorption and scattering as related to the seasonal evolution of terrestrial tundra snow. An integrated approach to the evaluation of snow-microwave interactions is developed with the introduction of dielectric properties (absorption), surface scattering, and volume scattering.

3.2.1 Snowpack dielectric properties and absorption

In snow, substantial changes to microwave absorption and scattering are observed with varied levels of liquid water content. The electric dipole structure of H_2O is responsible for this variation. While H_2O is electrically neutral, the distribution of positive and negative charges is asymmetric (Figure 3.2). The permanent polar structure of H_2O and significant separability of its charges causes it to be easily polarized when an electric field is applied (Glen and Paren, 1975). These qualities allow media composed of H_2O in multiple phases to be described as a dielectric.

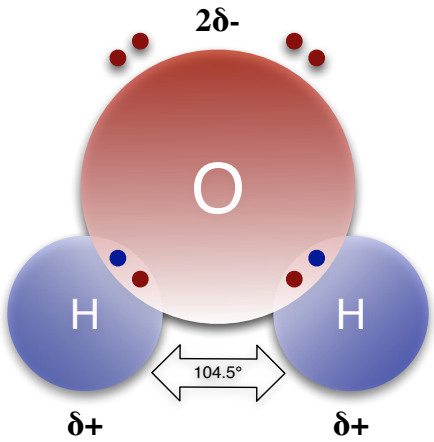

Figure 3.2: H_2O dipole structure and separability of electrical charges.

Dielectric materials are non-conducting and common to most solids encountered in remote sensing (Woodhouse, 2006). Not to be confused with wave polarization, dielectric polarization causes molecular reorientation when an electric field is applied (Baker-Jarvis, 2000). In the case of snow and water, positively charged hydrogen in H_2O attempts to reorient in the direction of the applied electric field to establish an electrically favourable configuration (Glen and Paren, 1975). Conversely, negatives charges found in oxygen will attempt to orient away from the electric field. When the electric field is removed, the molecules return to a stable arrangement. The causal relationship among the incident electric field and dipolar rotations is not instantaneous. Time elapsed between dipole reorientation and equilibrium is referred to as relaxation time (τ). In a dielectric, τ is dependent on viscosity, temperature, and the frequency of the applied electric field. Alternating lags induced by oscillating microwaves result in electric field losses dissipated as heat.

Electrical permittivity

The dielectric properties of snowpack are best introduced by discussing snow as a three component material (air, water, and ice). The components of snow and other dielectric materials are commonly described in terms of their relative permittivity (ε_r). This attribute characterizes the electrical storage of a material relative to a vacuum when exposed to an electrical field. In doing so, electric flux density (D) is related to the electric field (E) within a material (IEEE, 1998):

$$D = \varepsilon E \tag{3.7}$$

$$\varepsilon = \varepsilon_r \varepsilon_0 = (1 + \chi)\varepsilon_0 \tag{3.8}$$

where ε_0 is the permittivity of free space (8.85418782 x 10^{-12} $F \cdot m^{-1}$), and χ is electrical susceptibility, a measure of the materials polarizability. Extending upon the concept of permittivity, it is often convenient to use the complex form which explicitly defines magnitude and phase to describing the causal relationship between the applied electric field and dielectric polarization:

$$\varepsilon_r = \varepsilon^{'} - i\varepsilon^{''} \tag{3.9}$$

where, $\varepsilon^{'}$, the real part of complex permittivity describing ability of a material to be polarized and store energy and $\varepsilon^{''}$, the imaginary part, is a loss factor describing dissipation of energy. The magnitude of each component varies in relation to the physical properties of the media and frequency of the interacting wave. The permittivity of snow is balanced by variation of air, water, and ice composition, each having distinctive dielectric properties at microwave frequencies.

Air

Microwave propagation in porous air space is independent of frequency and equal throughout the snowpack (Mätzler, 1987). Complex relative permittivity of air within the snowpack is assumed to be the same as free space ($\varepsilon_{air} \approx 1 - i0$). Therefore, for the purpose of microwave remote sensing of snow, air is not considered a significant source of absorption or scattering.

Liquid Water

Liquid phase H_2O is weakly structured with intermittent hydrogen bonds between molecules. Therefore, it has a relatively low viscosity and is susceptible to polarization. In terms of complex relative permittivity, this is described by a high values of ε_r. First order dielectric behaviour of liquid H_2O can be estimated using Debye's equations for a single relaxation time (Figure 3.3; Debye, 1929; Stiles and Ulaby, 1982):

$$\varepsilon^{'} = \varepsilon_{\infty} + \frac{\varepsilon_0 - \varepsilon_{\infty}}{1 + (2\pi f\tau)^2} \tag{3.10}$$

$$\varepsilon^{''} = \frac{2\pi f\tau(\varepsilon_0 - \varepsilon_{\infty})}{1 + (2\pi f\tau)^2} \tag{3.11}$$

where, f is frequency, ε_{∞} is permittivity at the high frequency limit, ε_s is permittivity at the low frequency limit and τ is relaxation time. The relaxation time of liquid water in equations 3.10 and 3.11 can be approximated as:

$$\tau = \frac{4\pi nr^3}{kT} \tag{3.12}$$

where, r is molecular radius, n is viscosity and k is Boltzmann's constant (1.3806503 $\times 10^{-23}$ J $\cdot$ K^{-1}). Alternatively, τ can be replaced with relaxation frequency; the frequency at which $\varepsilon^{"}$ is maximized (Mätzler and Wegmuller, 1987). Here, relaxation frequency is related to relaxation time by:

$$f_0 = (2\pi\tau)^{-1} \tag{3.13}$$

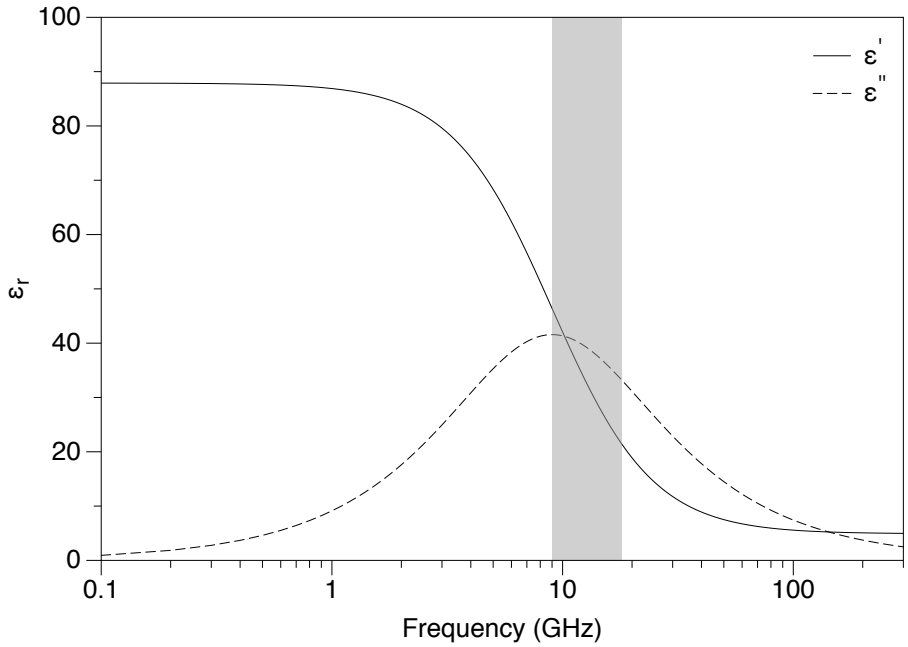

Figure 3.3: Complex components of relative permittivity ($\varepsilon^{'}$ and $\varepsilon^{''}$) for water as estimated using Debye's equations (3.10 and 3.11). Parameters: $\varepsilon_\infty = 4.9$, $\varepsilon_0 = 88.1$, $T = 0°\text{C}$.

Figure 3.3 demonstrates the frequency dependance of ε_r for liquid water at 0°C as estimated with Debye's equations. Maximum $\varepsilon^{''}$ and therefore relaxation frequency of liquid water is found in the microwave spectrum at approximately 9 GHz. This observation is critical for radar remote sensing as it identifies increased dissipation of microwave energy and high ε_r in liquid water. The Ku- and X-band frequencies used in this thesis are found in close proximity to the relaxation frequency of liquid water. Thus, retrieval methods can be expected to be significantly influenced by the presence of liquid water.

Ice

The crystalline structure of ice and stronger hydrogen bonding as a solid has a minimizing effect on the reorientation of H_2O when an electric field is applied. Without reorientation, microwave absorption is lowered by proxy of reduced molecular interaction. In real world observation, point defects in ice structure can account for small amounts of absorption (Glen and Paren, 1975). Bjerrum (1952) suggests these defects occur as free bonds or the formation of H_30 and OH^- ions. Positive and negative ions in ice cause a displacement of charge when an electric field is introduced. The resulting molecular interactions produce friction and dissipate energy as heat. Impurities introduced in the formation of ice contribute to ionizations which may increase ε_r. Regardless, interactions discussed here are magnitudes lower than reorientations observed in liquid water and producing much lower ε_r.

It is generally regarded that $\varepsilon^{'}$ can be approximated as 3.17 ± 0.03, independent of frequency (Colbeck, 1982b; Mätzler, 1996; Mätzler and Wegmuller, 1987; Stiles and Ulaby, 1982). The imaginary component ($\varepsilon^{"}$) of ice at microwave frequencies has a slight temperature and frequency dependancy, but is very small in magnitude (Cumming, 1952; Mätzler and Wegmuller, 1987). Like liquid water, lower temperatures in ice will cause $\varepsilon^{"}$ to drop as viscosity increases. Moreover, higher frequency microwaves decrease τ effectively elevating $\varepsilon^{"}$. Due to these factors, the relaxation frequency of ice is found in the kHz range. Ku- and X- band, found in the GHz range, are well beyond the relaxation frequency and are not subject to significant attenuation due to first-order dielectric effects of ice.

Snow

The complex relative permittivity of snow is a weighted summation of its components. Based on the early work of Cumming (1952), the permittivity of dry snow was found to be a function of density and independent of frequency. Typically, this is quantified by using either empirical or physically based mixing models describing snow as ice in an air background. Two commonly used mixing methods were developed by Polder and van Santeen (1946) and Tinga (1973) to explain the relationship with density. The model of Tinga (1973) describes two-phase mixing as:

$$\varepsilon_{ds} = 1 + \frac{2v_i(\varepsilon_i - 1)}{(2 + \varepsilon_i) - v_i(\varepsilon_i - 1)} \tag{3.14}$$

where, v_i is the ice volume fraction, and ε_i is the complex permittivity of ice. In Tinga's model, increasing ice fraction causes an increase $\varepsilon_{ds}^{'}$ as the lower permittivity air space is replaced with ice matrix. Alternatively, several empirical approximations exist such that $\varepsilon_{ds}^{'} = 1 + 2a\rho$ where $a = 2 \pm 0.09$ (e.g. Mätzler, 1996; Stiles and Ulaby, 1982; Tiuri, 1984). In general, values for $\varepsilon_{ds}^{'}$ are found between 1.2 and 1.8 for tundra snow conditions (200 to 450 kg m^{-3}, see Figure 3.4). Empirical approximations of $\varepsilon_{ds}^{"}$ are challenging because of low value in the range of 10^{-3} at microwave frequencies. In dry snow at microwave frequencies, $\varepsilon^{''}$ is typically disregarded in analysis.

Absorption

One of the most important uses of complex relative permittivity in snow is to describe microwave wave propagation by quantifying loss of incident energy. This loss is commonly identified as absorption and is related to a snowpack volume with the power absorption coefficient:

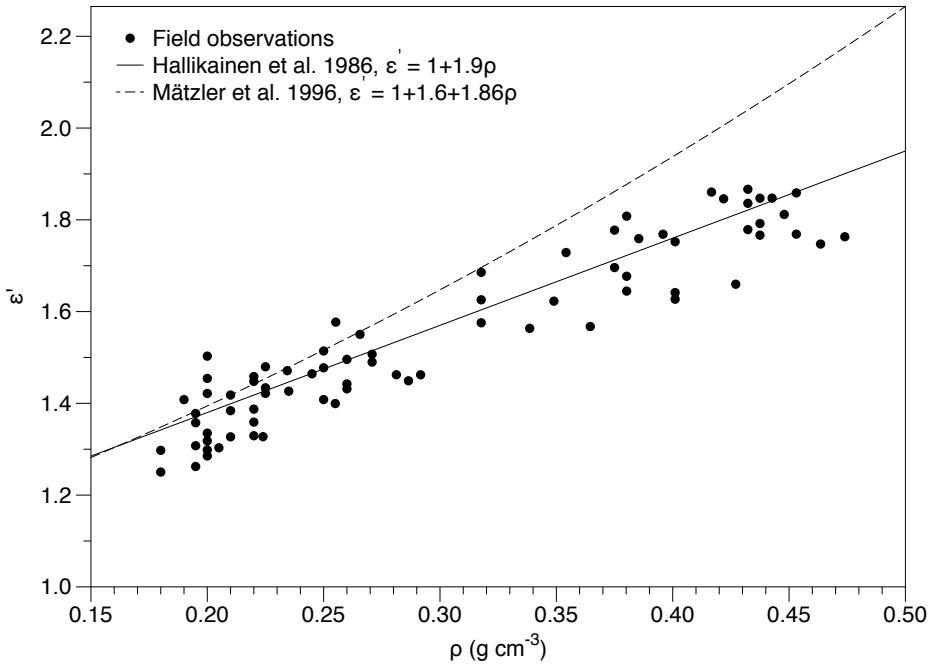

Figure 3.4: Field observations of $\varepsilon^{'}$ collected in tundra snow near Churchill, Manitoba, Canada. Fit lines show commonly used empirical relationships with density (Based on equations from Hallikainen et al., 1986; Mätzler, 1996).

$$k_a = (4\pi/\lambda)\left\{(\varepsilon'/2)\left[(1+tan^2\delta)^{1/2}-1\right]\right\}^{1/2} \tag{3.15}$$

Increasing relative permittivity and liquid water content (δ) in 3.15 promotes absorption of incident energy. The inverse of k_a reflects this by identifying sharp decreases in the distance over which average incident power is absorbed when liquid water content is increased (Williams et al., 1990). In other words, penetration depth ($1/k_a$) of the snow volume is significantly reduced with increasing absorption. Based on this, Ku-band in dry snow conditions can penetrate to depths between 3 and 5 meters while the longer wavelength

X-band can penetrate approximately 10 meters (Mätzler, 1987; Rott et al., 2010). Penetration depths are minimized when liquid water is found within the snow volume. At high frequencies, dry snow scattering losses dominate over absorption due to the low relaxation frequency of snow. To further characterize the propagation of waves within snow, it is then essential that the physical processes of surface and volume scattering are discussed.

3.2.2 Physical snowpack properties and scattering

Absorption and scattering are part of a system of physical interactions that determine the magnitude and polarization of backscatter from snow covered terrain. Given the demonstrated absence of microwave absorption in dry snow, primary consideration is given to processes of scattering which may occur at surfaces (e.g. air-snow or ground-snow) or within the snow volume. Microwaves directed towards snow covered terrain first interact at the air-snow interface where incident energy is divided into forward and backward scattering components known by their respective processes, transmission and reflection. The magnitude and direction of each component is determined by the geometry of the incident wave and characteristics of the interface including roughness and relative permittivity.

Surface scattering

Incident energy (E^i) of specified angle (θ) is partially reflected from smooth surfaces as coherent scatter in the specular direction (θ_r) (Figure 3.5; Fung et al., 1992; Woodhouse, 2006). The dynamics of this interaction are dependent on the roughness and dielectric mismatch between the two materials forming the surface. Radar roughness of the surface can be determined using a criterion such as Fraunhofer's

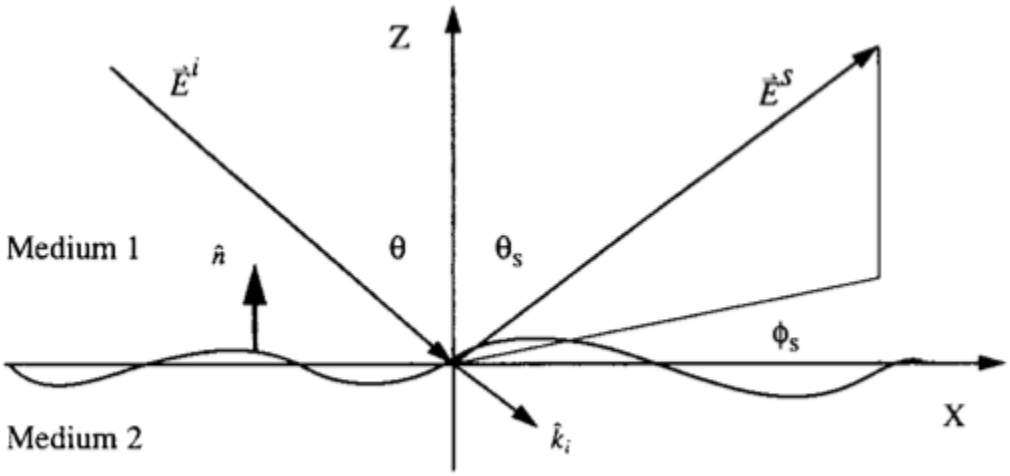

Figure 3.5: Geometry of microwave scattering at a surface (Modified from Fung et al., 1992)

$$\sigma_h = \frac{\lambda}{32\cos(\theta)} \tag{3.16}$$

where σ_h is the standard deviation of the surface height and is considered radar smooth when $\sigma_h < \lambda/32\cos(\theta)$. As σ_h increases, reflections becomes increasingly diffuse when wavelength and incident angle are held constant. Backscatter isotropy at a surface increases the amount of energy directed towards a receiving antenna, thereby strengthening the surface scattering contribution. Energy not reflected is subject to transmission and, in the case of an air-snow interface, is transmitted into the snow volume. During transmission, incident energy changes in velocity (v) and direction (θ_t) based on dielectric discontinuation between the upper (air) and lower (snow) media. The behaviour of this relationship is described by Snell's Law:

$$\frac{\sin\theta_i}{\sin\theta_t} = \frac{v_1}{v_2} = \frac{n_2}{n_1} \tag{3.17}$$

According to this law, $\Delta\theta$ is proportional to the ratio of each media's refraction index (n). The difference between the velocity of light in a vacuum and the velocity of light in the media defines n, which may also be approximated using permittivity where $\varepsilon = n^2$. In the case of an air-snow interface, the refractive index of the lower media, snow, is higher causing the incident wave to be redirected towards normal.

To quantify the directional components of incident energy at a surface, Fresnel's reflection coefficients (R) are used:

$$R_{vv} = \left(\frac{\varepsilon \cos\theta_i - \sqrt{\varepsilon - \sin^2\theta_i}}{\varepsilon \cos\theta_i + \sqrt{\varepsilon - \sin^2\theta_i}} \right)^2 \tag{3.18}$$

$$R_{hh} = \left(\frac{\cos\theta_i - \sqrt{\varepsilon - \sin^2\theta_i}}{\cos\theta_i + \sqrt{\varepsilon - \sin^2\theta_i}} \right)^2 \tag{3.19}$$

The absolute magnitude of R from 0 to 1 represents a transition from complete transmission to total reflection. Two equations are used to quantify R as the relationship with incident angle is defendant on polarization (Woodhouse, 2006). According to the equation set, horizontally polarized waves respond to incident angle with exponentially increasing reflectivity (Figure 3.6). In contrast, vertically polarized waves initially decrease in reflectivity to a minima known as the Brewster angle. Past this angle, vertical reflectivity increases and maximizes at the grazing angle (90°).

In practical application, differences in polarization response dictate the role of surface scattering in remote sensing of snow. As described in equation 3.18, vertically polarized

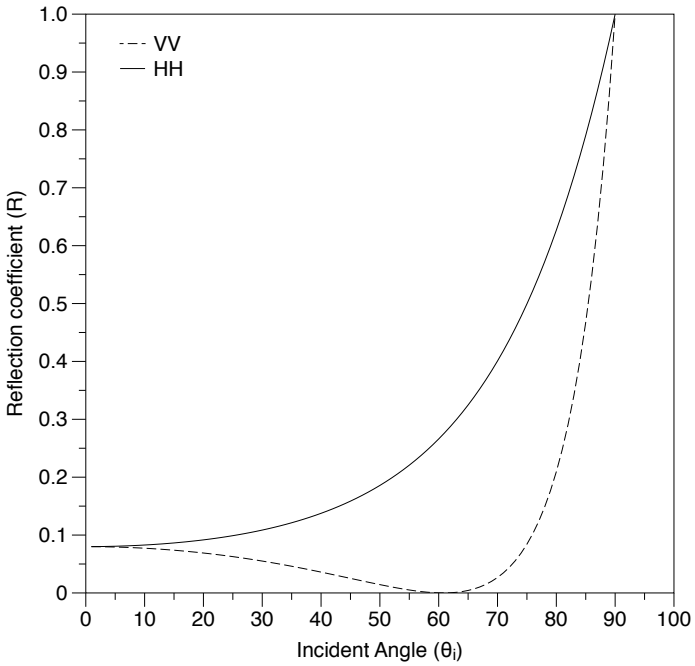

Figure 3.6: Fresnel's reflection coefficient (R) as a function of incidence angle (θ_i). Calculated using equations 3.18 and 3.19 where $\varepsilon = 3.2 - i0$.

waves have the tendency for increased transmission at surfaces. Studies concerned with snow volume may be inclined to exploit this relationship where surface information is unwanted. For example, to meet the observational requirements for snow retrieval of $CoReH_20$, only vv and vh polarizations were proposed to minimize the influence of air-snow and internal surfaces (Rott et al., 2010). Range resolutions of satellite-based sensors are much larger than snowpack depth and, therefore are inadequate to resolve individual layers or surfaces. In ground-based or airborne application where adequate range resolution is available, hh polarization may be desirable to identify reflections from individual surface features within the snowpack.

Air-snow surface reflections in the microwave spectrum are typically considered insignificant with power reflection coefficients ranging from 0.02 to 0.08 (Ulaby et al., 1981). Under

dry conditions, the air-snow interface (σ_{pq}^{as}) contributes less than 25% of total backscatter at Ku-band (Shi, 2004). Total contribution is further diminished with increase wavelength as a result of higher transmissivity. These interactions drastically change at both Ku- and X-band if the surface becomes wet. With increasing liquid water content, relative permittivity of snow increases and microwaves become subject to significant reflection in the specular direction at the snowpack surface. Previous studies in the microwave spectrum have shown a decrease in snowpack backscatter by as much as 5 dB at 3% wetness (Stiles and Ulaby, 1980). Complicating analysis, backscatter may also increase when the snow surface is wet if the interface is sufficiently rough. Accordingly, retrieval of volumetric snow properties is challenging once the air-snow surface has saturated and will not be addressed in this thesis.

Surface scattering in terrestrial environments also occurs when microwaves penetrate the snow volume reaching the soil surface. Changes in roughness and permittivity at the snow-soil interface define the magnitude and directionality of reflections backwards into the volume. Free water in soil plays an important role here as it increases reflection as a function of soil permittivity (Nghiem and Tsai, 2001). Due to this, ground contribution to the total energy returned to the sensor can be substantial and is influenced by seasonal freeze-thaw processes (Shi, 2004). It is therefore important to evaluate and separate ground scattering contributions to isolate the desired volumetric snow response. At Ku- and X-band, microwaves reaching the ground surface respond almost equally because it is radar rough for both wavelengths.

Volume scattering

At the beginning of this chapter, incident microwaves were shown to be transmitted at snow surfaces. The resulting forward scatter begins a complex series of interactions where

microwaves are subject to variation in propagation and are distorted within the snow volume. The strength of the observed distortion is proportional to the dielectric discontinuation and geometry of the scattering particles composing the snow volume (Mätzler, 1987; Ulaby et al., 1981). Physical attributes of snow grains including size, shape, and density govern interactions within the snowpack known volume scatter (σ^v and σ^{gv} in Figure 3.1).

Snow grains are rarely spherical, but because of their random orientation, net scattering closely resembles that of a sphere (Woodhouse, 2006). This generalization allows for the use of simple scattering models to describe re-emitted energy. Snow grains with diameters much smaller than the incident wavelength are described in this way as Rayleigh scatters. Particles of this type scatter quasi-diffusely with roughly equal forward and backward components (Ulaby et al., 1981). According to the Rayleigh model, the scattering cross-section of a sphere can be approximated as (Mätzler, 1987):

$$\sigma = 4\pi a^2 (ak_0)^4 \left| \frac{\varepsilon' - 1}{\varepsilon' + 2} \right|^2 \sin^2\chi \tag{3.20}$$

where, k_0 is the incident wavenumber ($k_0 = 1/\lambda$), χ is the angle between the incident electric field and the scattered wave vector, and a is the radius of a single sphere. If wavelength is maintained, the model shows sensitivity to grain size and snow permittivity. The former is of interest as it provides a starting point for characterization of scattering by physical snow processes. Changes in scattering resulting from the latter would only be influential under wet snowpack conditions where the range of permittivity is dynamic. By neglecting multiple interactions, volume scatter may be approximated by the product of the number of grains and the above calculated cross-section.

As the ratio between grain size and wavelength approaches unity, an alternative scattering model is needed. In this case, Mie type scattering is used to describe the physical

process. Under this model, phase front distortion behaves in such a way that scattering occurs more so in the forward direction due to diffraction and geometric optic effects (Mätzler, 1987). Scattering in this region is complex and small changes in size can cause coherent scattering effects. The effects of increasing grain size under the Mie model are not as clear as the Rayleigh model requiring accurate estimation of the effective wavelength in the media to determine contributions.

With increasing path length, the effects of scattering within the snowpack are pronounced. Waves propagating under these conditions are subject to increasing levels of interaction. Multiple scatter may occur when diffusely emitted energy from one snow grain interacts with a second grain. Multiple scattering is one of the most important conditions for depolarization of incident microwaves (Du et al., 2010). First-order depolarization within the volume results from coherent near-field interactions amongst grains (Zurk et al., 1996). The misalignment of the resulting dipole moment controls the magnitude of the depolarization event. Grain size and shape are also contributing factors in multiple scattering depolarization (Du et al., 2010). Multiple scattering is not restricted to direct volume contribution, but also occurs as ground-volume (σ_{pq}^{gv}) and volume-ground (σ_{pq}^{vg}) contributions. These interactions are complex and dominate high order scattering and depolarization.

In general, increasing backscatter contribution from the snowpack volume results from either increasing grain size or depth (Fung, 1994). Snowpacks dominated by constructive growth will display an increasing backscatter related to its seasonal evolution. The main cause of this increase is the change in the scattering regime as particle size approaches the incident wavelength. This is compounded by multiple scattering and the near field effect that occurs when distances between grains become smaller than the wavelength. Here, coherent scattering causes an increase in the backwards direction, effectively increasing

the volume cross-section. This phenomena is also related to the significant cross-polarized backscatter observed with increasing snow volume (Shi and Dozier, 2000). The effect of depolarizations resulting from multiple scattering in the volume is prominent at steep incident angles as the effective path of propagation is increased (Fung, 1994; Rees, 2001). In practical application, multiple scattering within the snow volume is observed as an increasing depolarization ratio (σ_{vh}/σ_{vv}) and direct volume scatter component ($\sigma^{v}_{vv}/\sigma^{t}_{vv}$) (Shi, 2004).

While the relationship between grain size and backscatter is well cited, few studies have focused on the estimation of scattering specific to temperature gradient growth types. Preferential orientation and elongated growth of depth hoar may produce favourable conditions for backscatter. Previous active microwave studies have shown these grains to contribute substantially at long wavelengths (e.g. Marshall et al., 2004; West, 2000). Research regarding the scattering effects of depth hoar have a long history in passive microwave observation (e.g. Hall, 1987; Hall et al., 1986, 1991). Here, the large scattering cross-section of depth hoar compared to grains of similar size is a source of uncertainty in SWE retrieval (Foster et al., 2005). The presence of depth hoar in passive microwave studies may lead to the overestimation of SWE, and a similar effect may be found in active microwave studies. Uncertainty related to depth hoar may be prevalent in tundra type snow where sustained temperature gradient metamorphosis is present.

Many of the useful insights into snow-radar interactions have come from physically based models. Figure 3.7 shows decomposed snow and ground backscatter contributions at Ku- and X-band as estimated with a dense media radiative transfer model (Xu et al., 2012). Under dry snow conditions, such models estimate that 60% of X-band co-polarized signals originate from within the volume (Shi, 2008). In contrast, Ku-band signal is near dominated by volume scatter (Shi, 2004; Shi et al., 2003; Xu et al., 2012). The remaining contribution

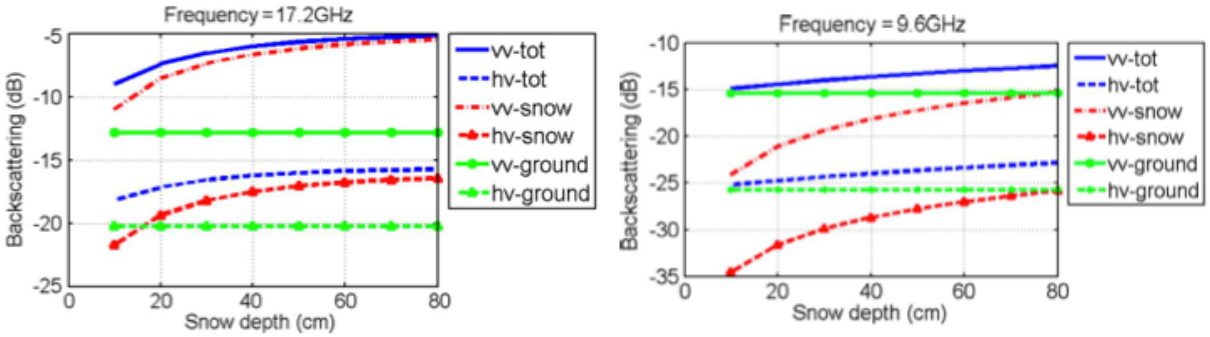

Figure 3.7: Total backscattering from snow covered terrain decomposed into snow and ground scattering components at Ku- (17.2 GHz) and X-band (9.6 GHz) with Biconti-nous/DRTM (Modified from Xu et al., 2012).

at each wavelength originate from first and possibly second order ground-snow scattering. The complexities arising from these interactions are noise to the property retrieval process. To remove noise and diminish uncertainty, the physical processes contributing to total backscatter must be then isolated and decomposed (Strozzi and Matzler, 1998).

3.3 Previous observations of snow at Ku- and X-band

Field studies relating *in-situ* snow properties to observed backscatter response are of great importance in the development of property retrieval methods and electromagnetic models (Strozzi and Matzler, 1998). Over the last four decades, a growing body of literature has evaluated snow-radar interaction with ground-based (Fujino et al., 1985; Kendra et al., 1998; King et al., 2013; Marshall et al., 2004; Morrison and Bennett, 2014; Rott et al., 1993; Ulaby et al., 1984; Willatt et al., 2010), airborne (Floricioiu and Rott, 2001; Hallikainen et al., 1993; Kern et al., 2009; Yueh et al., 2009), and satellite (Nghiem and Tsai, 2001; Pettinato et al., 2013) microwave sensors. Despite the increasing number of studies,

few have collected seasonal or coincident dual frequency (Ku- and X-band) backscatter measurements of terrestrial snow. Moreover, previous studies have not adequately addressed interactions specific to arctic snow cover types including those found in tundra environments.

Early investigation of snow-radar interaction was conducted by Ulaby and Stiles (1980) with a limited range of artificially manipulated snow conditions. In this experiment, snow was manually piled to replicate accumulation for SWE between 0 and 700 mm. As snow was manually added to the field of view, coincident backscatter measurements at 9 GHz were also collected. Across the range of observed SWE, an increase of approximately 8 dB was found with a majority of the increase observed at low SWE. Ulaby et al. (1984) expanded upon initial observations by conducting similar experiments over snow covered asphalt, concrete, grass, and bare ground with an extended set of observing microwave frequencies. Sensitivity to increasing SWE and depth was observed at both Ku (16.6 GHz) and X-band (9.0 GHz) as part of this experiment (Figure 3.8). As in the previous study, sensitivity to change in SWE and depth was strongest with shallow accumulation. The full range of SWE common to tundra snow was found within the range of sensitivity described by the study ($>$ 200 mm). In each study, the authors highlighted the need for further evaluation of the relationship between σ^0 and SWE under natural conditions. Additionally, the second study called for the investigation of multifrequency retrieval given the observed frequency dependent difference in backscatter.

More recently, a number of purpose built systems for radar observation of snow properties have been deployed as part of major field campaigns including the Cold Land Processes Experiment (CLPX) in Colorado, USA (Marshall et al., 2004), the Nordic Snow Radar Experiment (NoSREx) in Finland (Lemmetyinen et al., 2011), SAR Alps in Austria (Morrison et al., 2007), and the Canadian Snow and Ice Experiment (CASIX) in Mani-

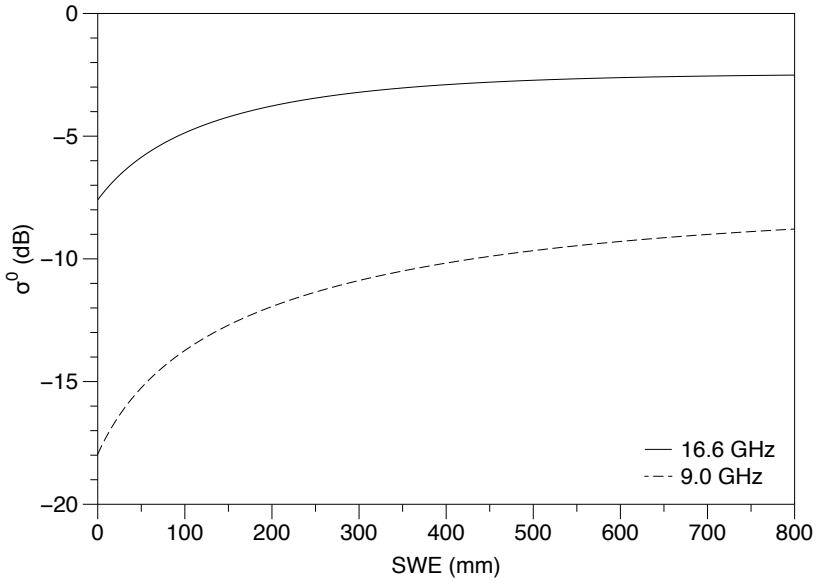

Figure 3.8: Empirical relationship between σ^0 and SWE at 16.6 and 9.0 GHz (Based on empirical models from Ulaby et al., 1984). The range of observed SWE was created artificially by adding snow to the field of view.

toba, Canada (King et al., 2013). Radar systems deployed in each campaign were done so in support of the proposed satellite based radar missions SLCP (Snow and Cold Land Processes) and CoReH$_2$O. Preliminary analysis presented in each study demonstrates Ku-band sensitivity to the presence of terrestrial snow and changes to properties within the snow volume. Using wideband FMCW radar Marshall et al. (2004) show that Ku-band (14–18 GHz) is able to penetrate dry snow volume to depths greater than 100 cm while returning considerable information about internal stratigraphy (Figure 3.9). Moreover, significant shifts in the dielectric properties of the snowpack observed as ice crusts and vertical shifts in grain properties, produced significant reflection at Ku-band. Dual frequency Ku- and X-band observations introduced in Morrison et al. (2007) and Lemmetyinen et al. (2011) demonstrated frequency dependancy and lateral heterogeneity in backscatter signal from terrestrial alpine snow targets. Finally, backscatter observations at Ku- and X-band

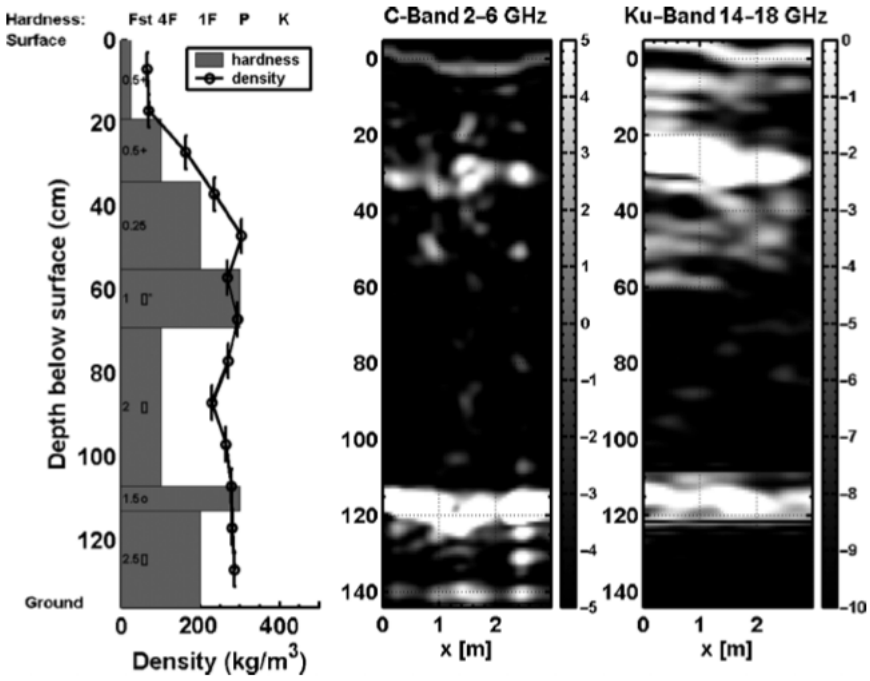

Figure 3.9: Wideband FMCW measurements at C- and Ku-band of terrestrial snow in Colorado as part of CLPX (Modified from Marshall et al., 2004). White colour in the radar images show strong reflection and black indicates no reflection. Strong reflections from stratigraphy and from the depth hoar layer are found at Ku-band.

evaluated in King et al. (2013) demonstrated seasonal sensitivity to SWE in a wetland environment. The remaining chapters of this thesis will provide detailed analysis of tundra snow backscatter observation made as part of CASIX.

In addition to ground-based studies, airborne campaigns have been conducted to explore the spatial scaling of backscatter and observed relationship with SWE. Coincident Ku- and X-band measurements were made as part of the Helisnow campaign in the Austrian Alps using Multi^{3}Scat, a helicopter-based scatterometer operating at L, S, C, X and Ku-bands (1, 2.4, 5.3, 10, and 15 GHz) (Kern et al., 2009). To date, there has been no formal analysis of the terrestrial snow measurements made but recent publication indicates that

the dataset has been incorporated in the validation of electromagnetic models used in the CoReH$_2$O retrieval method (Rott et al., 2010). Additional airborne acquisitions were completed using NASA's polarmetric scatterometer (POLSCAT) as part of the CLPX (Yueh et al., 2009). Ku-band (13.95 GHz) backscatter measurements were collected over snow covered terrain along with an extensive ground validation campaign. The findings of this study support the feasibility of Ku-band property retrievals in dry snowpack. POLSCAT measurements made revealed increases in co-polarized backscatter between 0.15 to 0.5 dB for an increase of 1 cm in SWE (Figure 3.10). The strength of the relationship between σ^0 and SWE was spatially dependent where local vegetation, terrain, and, snow conditions were found to influence backscatter. The seasonal evolution of cross-polarized backscatter was shown to be influenced by seasonal metamorphic processes including snow grain grown and the development of ice lenses. The effective increase in backscatter attributed to non-spherical grain geometry was noticeable over multiple land cover types. While PolSCAT has no X-band sensor, coincident TerraSAR-X acquisitions were completed over several sites. The images along with the Ku-band observations have since been used in physical model validation and SWE retrieval development (see Rott et al., 2009, 2010).

Satellite based study at Ku- and/or X-band has been limited by the lack of civilian Earth observation platforms. At Ku-band, now defunct satellite scatterometer platforms including NSCAT (Nghiem and Tsai, 2001) and QuickScat (Hallikainen and Sievinen, 2007; Yueh et al., 2009) have demonstrated feasibility for observing snow processes. The coarse spatial resolution of each sensor makes it difficult to equate findings to current studies. Despite this, large-scale Ku-band sensitivity to snow physical properties identified by these studies is relevant to the development of SWE retrieval algorithms. At X-band, SAR systems including COSMOS-SkyMed (Pettinato et al., 2013) and TerraSAR-X, have demonstrated plausible potential for retrieval of snowpack properties under a selective set of

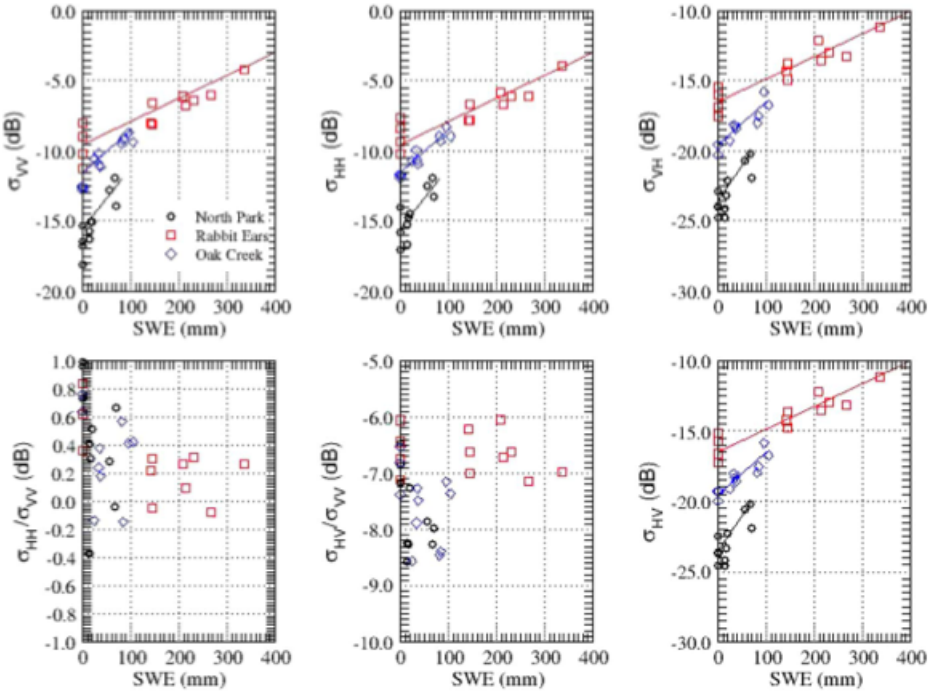

Figure 3.10: Comparison of POLSCAT (13.95 GHz) radar data and *in situ* SWE collected three different test sites in Colorado (Modified from Yueh et al., 2009). The observed relationships vary with local snow and vegetation, but in general show strong co- and cross-polarized sensitivity to increasing SWE.

conditions. Currently, there is no satellite mission or combination of missions that meet the temporal and spatial requirements to retrieve SWE or other derivative hydrological variables at scales of ground observed variation.

3.4 Summary

Microwave backscatter from snow covered terrain is governed by a complex set of interactions dependent on the physical and dielectric condition of the target. Given the potential

of terrestrial snow for significant change through a winter season, observations of dry terrestrial snow can be expected to exhibit a wide range of σ^0 related to local processes of accumulation and metamorphosis. Table 3.1 provides a summary of snow properties influencing backscatter in terrestrial environments. Of critical importance for the retrieval of snow properties is the absence of liquid water in the snow volume. Drastic increases in relative permittivity in the presence of liquid water limit penetration to very shallow depths at microwave frequencies. In dry snow conditions, seasonal accumulation will increase backscatter at a rate in some proportion to the increase of volume. As depth increases and multiple scattering becomes prevalent, co- and cross-polarized backscatter components will also respond to seasonal processes of metamorphosis influencing grain shape and size. In particular, temperature gradient metamorphosis and subsequent grain growth will promote increased backscatter as grain size approaches the observing wavelength. Sequential processes of accumulation and metamorphosis serve to produce complex interactions within the snow volume by creating dielectric discontinuities and potential sources of reflection. Total backscatter from a snow covered terrestrial target will be determined by a combination of the above attributes specific to local snow and environmental conditions.

Shi (2008) describes two critical requirements for radar retrieval of snow properties: (1) signal must be able to penetrate the volume and (2) backscatter from the volume must be strong enough to provide first-order information (Shi, 2008). Discussion in this chapter has shown that Ku- and X-band observations will satisfy these requirements based upon their theorized interaction with seasonal dielectric and physical properties of a terrestrial snowpack. Ku-band and X-band have been identified as high value frequencies for retrieval of terrestrial SWE because of their proximity in wavelength to snow processes scale (Marshall et al., 2004; Rott et al., 2010). The remainder of this thesis will introduce field based experiments used to evaluate snow-radar interaction in tundra environments across a range of typical snow conditions controlled by seasonal and spatial influences.

Table 3.1: Influence of seasonal snow properties on backscatter in terrestrial environments

Factor	Description
Permittivity	Microwaves penetrate snow to significant depths in dry conditions. The presence of liquid water reduces penetration depth and therefore limits ability to retrieve volumetric properties as a result of increasing relative permittivity.
Depth	Increasing path length within the snow volume provides additional opportunities for microwave scattering. As depth increases, a proportional increase in σ^0 may be observed if full penetration of the snowpack is achieved.
Density	Increasing density is linearly related to increasing permittivity. Large discontinuations in density can produce backscatter at transitions.
Stratigraphy	Layering in terrestrial snow can introduce dielectric discontinuities with large changes in density. Internal reflections may complicate backscatter analysis.
Grain size	As grain size increases its size relative to the observing wavelength decreases and scattering increases. Seasonal metamorphic processes allow for significant variation in grain size and potentially backscatter.

Chapter 4

UW-Scat - A ground-based dual frequency scatterometer for observation of snow properties

4.1 Introduction

Snow extent and mass in the Northern Hemisphere will fluctuate throughout the 21^{st} century with an increasingly complex response to climate variability (Brown and Mote, 2009; Frei and Gong, 2005). This response is significant as changes in the physical properties of terrestrial snow cover have implications in the Earth system. By effectively moderating atmospheric and surface heat exchanges, the thermal and optical properties of snow are strong modifiers of the cryospheric energy balance. Multi-scale variability in the duration, extent, and mass of terrestrial snow cover is a significant element of this balance (Brown, 2000; McCabe and Wolock, 2010; Mote, 2006; Serreze et al., 2000). In addition to modu-

lating climate, snow is an important freshwater storage which can dominate regional runoff (Barnett et al., 2005). Changes in regional snow hydrology can impact the livelihoods of northern communities who depend on winter conditions for subsistence hunting, overland travel, and water security. As a result, quantifying snow properties from local to global scales has become important for understanding multi-scale climate systems and regional hydrology. A key factor to improving our understanding of the physical role of terrestrial snow in Earth systems is the retrieval of local scale properties that convey mass and energy, specifically snow water equivalent (SWE).

Existing Earth observation systems do not have the capacity to resolve SWE at the scale of variation found on the ground. Recent field and theoretical investigations (Du et al., 2010; Kern et al., 2009; Morrison et al., 2007; Werner et al., 2010; Yueh et al., 2009) have shown microwaves in the range of 8 to 18 GHz to be particularly sensitive to snow volume and potentially SWE at scales of interest. The promise of these studies has been recognized by the European Space Agency Earth Explorer candidate mission, CoReH$_2$O (Cold Regions Hydrology High-Resolution Observatory) which seeks to observe cryospheric variables at high spatial resolutions ($\leq$ 50 m x 50 m) using a dual-frequency (17.2 and 9.6 GHz) synthetic aperture radar (Rott et al., 2010). While a number of studies have evaluated sensitivities at each of the proposed frequencies to snow properties, few have explored the potential for coincident dual-frequency observation and retrieval. Moreover, no previous studies have attempted to characterize interactions in tundra and wetland environments.

To evaluate the potential for dual-frequency observation of seasonal snowpack processes, ground-based polarimetric scatterometers were deployed in tundra and wetland environments near Churchill, Manitoba, Canada during the winters of 2009-2010 and 2010-2011. This letter introduces the University of Waterloo scatterometer (UW-Scat) system which

was deployed during each campaign to collect spatially distributed dual frequency observations. Data collected with UW-Scat contributes local scale observations relevant to future space-borne missions such as CoReH$_2$O. The datasets may also aid in the development of SWE retrieval algorithms by furthering our understanding of snow-microwave interactions in northern environments. The remainder of this letter describes system design, data processing, and provides examples of unique data sets obtained during field deployments of UW-Scat.

4.2 UW-Scat Instrument

UW-Scat is a pair of dual-polarization, frequency modulated continuous wave radars operating at centre frequencies of 17.2 and 9.6 GHz. The centre frequencies are found within the band designations Ku- and X-band. The scatterometers are physically separate allowing for user-specified single frequency or coincident dual-frequency operation. Each scatterometer consists of three subsystems: (1) A radio frequency (RF) unit which integrates system antennas and RF hardware, (2) an environmental enclosure housing data acquisition, temperature control and AC power distribution, and (3) a two axis positioning system (Figure 4.1). An overview of the UW-Scat sensor parameters is provided in Table 4.1.

Each RF unit employs a dual antenna design for application specific operation. In near-field application, a single narrow beam antenna is used to transmit and receive, avoiding parallax at short distances. This configuration is designated as narrow beam mode and produces a half power beam width of 5.6° at Ku-band and 4.3° at X-band. To achieve greater sensitivity at longer distances, a corrugated flood beam antenna is used for transmission, greatly improving transmit-receive isolation. Broader beam widths of 7.2° at Ku-band

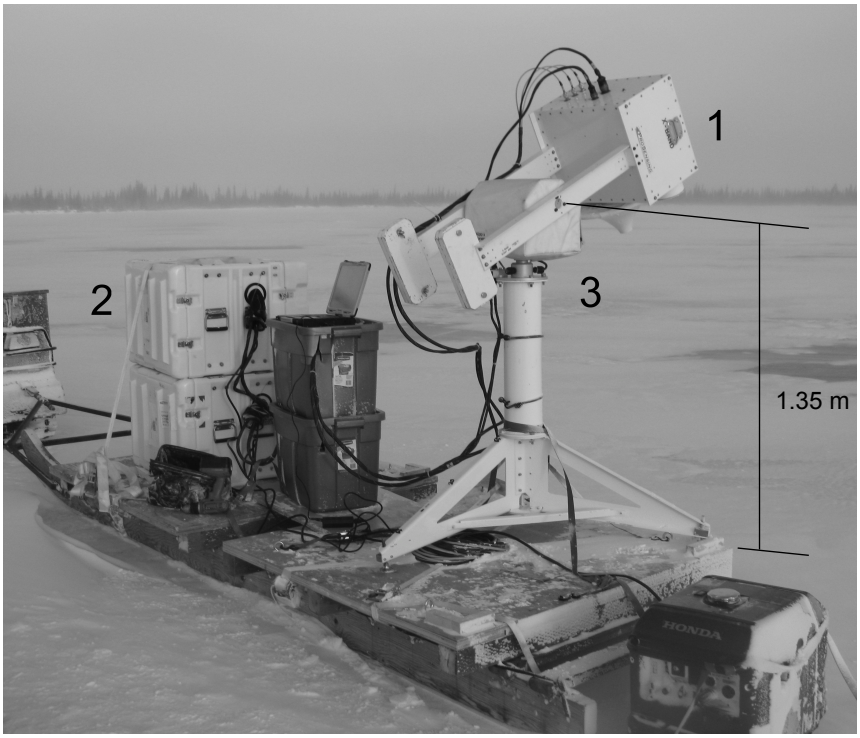

Figure 4.1: UW-Scat in a mobile deployment configuration with the X-band RF unit mounted. The scatterometer subsystems include a (1) RF Unit, (2) Environmental enclosure, and (3) a 2-axis positioning system / base 1.35 m, above the platform.

and 5.8° at X-band are found in this configuration, designated as flood beam mode. At a standard operating height of 1.6 m, the footprint dimension for all beam modes is <1 m in the range direction at elevations <60°. The availability of narrow and flood beam modes allows UW-Scat to adapt to a variety of field conditions without physical reconfiguration.

The RF units house a custom designed waveform generator to produce a software programmable linear FM chirp with direct digital synthesis.[1] The X-band chirp waveform nominally sweeps from 69.58-90.41 MHz and is upconverted to 389.58-410.41 MHz. Using a frequency multiplier, the chirp waveform is increased to 4675-4925 MHz before passing

[1]Complete RF block diagrams are available in Appendix A Figures A.1 and A.2.

Table 4.1: UW-Scat sensor parameters

Parameter	X-band	Ku-band
Output frequency (GHz)	9.35–9.85	16.95–17.45
Transmit bandwidth (GHz)	0.5	0.5
Transmit power (Flood, Narrow dBm)	9.5, -11.8	3.5, -8.0
Range resolution (m)	0.3	0.3
Cross-polarization isolation (dB)	>30	>30
Sensitivity (dB m^2/m^2)	-50	-50
Antenna beamwidth (Flood, Narrow °)	5.8, 4.3	7.3, 5.6
Transmit/receive polarizations	VV, HH, VH	VV, HH, VH

through a frequency doubler to create the 9350-9850 MHz linear FM sweep. The X-band chirp waveform is then amplified and split by a power divider for use in transmission and reception. The Ku-band RF unit replicates the X-band chirp waveform before upconverting to 16950-17450 MHz and feeding the power divider. To complete transmission, a switch directs signal from the power divider to an antenna and polarization port.

Transitioning to reception, each RF unit is switched to select one of four inputs. The initial two states select vertical or horizontal polarization. The remaining states select either a 20 ns delay line used to monitor system drift or a 50 Ohm load to monitor noise. The received signal is filtered and amplified before it is directed to a receiver mixer where it is converted to baseband. The previously split transmission waveform is used by the mixer as the local oscillator signal. The baseband signal is then fed to the data acquisition system over a 10 m long coaxial cable. The data acquisition system is housed in a temperature controlled enclosure where a shock mounted host computer receives the baseband signal with a GaGe 1602 digitizer. Acquisitions of baseband data are processed in data blocks where one sweep of the FM waveform is collected for each of the four transmit polarization combinations, the calibration loop, and the noise signal. Combined, the six data blocks form a single data record which is saved to the host computer for offline post-processing.

A shock mounted temperature controller is co-located with the data acquisition system to drive conduction heaters in the environmental enclosures and RF units. When powered, the temperature controller sets each enclosure to a consistent 35°C. This allows UW-Scat to stabilize temperature sensitive RF components in extreme conditions typical of the Canadian sub-arctic. A rack mounted uninterruptible power supply and power conditioner ensure that irregularities in AC power are minimized. The entire system can be operated with a wireless client laptop or from a distance over a network where infrastructure exists to do so.

4.3 Operation and Data Processing

The modular design of UW-Scat allows it to be easily transported and assembled by a team of two within 30 minutes of arrival at a remote location. UW-Scat can be deployed on top of a permanent platform or aboard a sled towed by a snow-machine. In general, the latter is preferable for field operation as it allows for deployment across a variety of snow, ice, and ground targets over a short period of time. Once a site has been selected, UW-Scat uses a modified Kipp and Zonen 2AP sun tracker to direct the radar beam across the target. In operation, a series of azimuthal sweeps is completed based on a user specified angular width and range of elevation angles.

A typical azimuthal sweep moves the RF unit through a 60° translation, left to right. Once an azimuthal sweep has been completed the positioning system is incremented in elevation, sweeping again in the opposite direction. This process is repeated until all prescribed elevations angles have been swept. Elevation angles are typically incremented in steps of 3° above 21° to provide overlap between scan lines while minimizing correlation, especially at near nadir angles. One full scan takes approximately 24 minutes to complete.

4.3.1 Calibration

Data collected with UW-Scat is calibrated with a combination of internal and external procedures to monitor system drift. Each data block is associated with an internal calibration loop measurement from the transmission delay line. Under field conditions this is an important measure as temperature sensitive components may produce variations if subjected to extremes or thermal gradients. The internal calibration loop provides a method to quantify variation in gain and generate an appropriate correction in post-processing.

An external calibration procedure similar to that implemented by Geldsetzer et al. (2007) is used to estimate transmit and receive distortions with an in-scene reference target. To complete the external calibration procedure a trihedral corner reflector with known radar cross-section is placed in the scatterometer far-field (17 m). Prior to each scan, observations of the calibration target are recorded in each polarization combination. In post-processing, observed differences in polarimetric phase and gain are used to derive distortion matrices from the reference target backscatter. The derived matrices are related to the target complex scattering voltages to produce a time series of corrections. This procedure is often challenging in the field as movement of the reference target or of the sensor itself can introduce significant uncertainties. Consequently, in-scene external calibration is not completed under windy conditions. Calibration data acquired under optimal conditions can be stored for use with scans lacking an in-scene calibration target.

4.3.2 Data Products

Digitized samples of the baseband signal are multiplied by a Hanning window to reduce range sidelobes and converted into the range domain using a fast Fourier transform. At each range gate, the data are averaged into covariance matrices containing 16 possible cross

products amongst the four transmit and receive polarization states for each elevation angle. To characterize range dependent transmit leakage, a set of sky observations are collected at the start of each scan. Sky observations are averaged and coherently subtracted from the target range profiles to isolate main beam backscatter. Once completed, the baseband data are ready for analysis and can be used to calculate normalized radar cross section (σ^0) and other polarimetric quantities.

Snow target σ^0 is calculated from the averaged range profiles and calibration data based on a formulation from Geldsetzer et al. (2007) such that

$$\sigma^0 = \frac{8\ln(2) R_t^2 \sigma_c \cos(\phi_{inc})}{\pi R_c^4 \theta_{3dB}^2} \left(\frac{\tilde{P}_r}{\tilde{P}_{rc}} \right) \tag{4.1}$$

where θ_{3dB} is the one-way half power beamwidth of the observing antenna; ϕ_{inc} is the incidence angle; σ_c is the frequency dependent corner reflector cross section; R_t is the range to the target; R_c is the range to the corner reflector; $\tilde{P}_r$ is the recorded power from the scene; and $\tilde{P}_{rc}$ is the recorded power from the corner reflector.

Total power returned from the scene, $\tilde{P}_r$, is estimated as the sum of power within a system specified number of range gates, N_g, around the peak return. Selection of an appropriate value for N_g requires that it be large enough to capture a majority of the incident beam and target impulse. This must be carefully considered as overestimation of N_g may introduce bias by sampling noise from range gates surrounding the target impulse. Experimentation found that 99% of the signal power is retrieved at a range interval of 0.8 m when observing a surface scattering point target. Volume scattering targets, such as snow, extend the range over which energy is returned. Field testing established that a range of 1.4 $\pm$ 0.4 m for shallow tundra snow is adequate to capture the returned signal

power. Based on this, N_g is estimated numerically along with the sensor elevation angle and antenna height to adjust for the elliptical shape of the antenna footprint.

4.3.3 Data Quality

Uncertainties in the estimation of σ^0 are largely a product of the number of independent samples and errors in the calibration procedure.[2] Other sources of error may include the signal-to-noise ratio (SNR) and approximations used to estimate sensor and target geometry. In post-processing, steps have been taken to estimate the influence of these variables so that uncertainties may be quantified and monitored.

An estimate of beam-limited independent samples is obtained by dividing the scan angular width by half the antenna beamwidth. When the major axis of the footprint exceeds the range resolution of the sensor (∼30 cm), the number of independent samples becomes a multiple of the number of gates within the footprint. A 60° azimuthal width produces a minimum of 21 Ku-band independent samples at 21° and a maximum of 567 at 81° in narrow beam mode. Using the same scan parameters, a minimum of 28 independent samples at 21° and maximum of 586 at 81° are observed at X-band. Flood beam observations produce a larger number of independent samples due to the increased azimuthal width. Logistical restraints including the height of the sensor prevent the practical collection of additional independent samples in sled based operation.

UW-Scat maintains a high SNR across a large range of elevation angles, decreasing as the sensor increments towards steeper angles. For example, averaged over 10 scans, a minimum Ku-band SNR of 8.2 dB was observed with a snow target σ^0_{HH} of -19.7 dB at an elevation angle of 81°. The same target produces an X-band minimum SNR of 8.8 dB

[2]Error metrics for UW-Scat are detailed in Appendix A.

with a σ^0_{HH} of -22.1 dB at 81°. At elevations angles closer to nadir, co-polarized SNRs are observed to be >13 dB at both frequencies. Cross-polarized returns also show SNR well above the noise floor at elevations angles >75°. Ku- and X-band SNRs of 9.7 dB and 8.8 dB were observed with σ^0_{HV} of -21.8 dB and -27.4 dB at 75°.

4.4 Experimental Deployments

4.4.1 Can-CSI 2009-2010

As part of the Canadian CoReH_2O Snow and Ice Experiment (Can-CSI), UW-Scat was deployed near Churchill, Manitoba, Canada to evaluate the potential for dual frequency observation of sub-Arctic snow in previously untested environments. Snow targets in tundra, fen, and lake ice environments were selected for seasonal observation and visited at regular intervals. UW-Scat was carefully positioned at the same location each visit to establish consistent viewing geometry amongst all observations. Coincident snow and scatterometer observations were obtained to characterize the seasonal evolution of the target backscatter and snow properties.

Table 4.2 presents the seasonal evolution of SWE and σ^0 at a fen site (58.7533 N, 93.8580 W) as observed across four investigation periods. The fen is a distinct wetland environment with a periodic cover of saturated frozen soil, low-lying vegetation, and basal ice. Snow cover in the fen is typical of a sub-Arctic environment consisting of a high density wind slab underlain with depth hoar of considerable radius (>2 mm). Mean SWE along a 100 m transect adjacent to the scatterometer increased from 61 mm on January 8 to 122 mm on April 11. The observed increase in SWE was driven primary by wind process

as density increased from 249 kg/m^3 to 306 kg/m^3 with a modest increase in depth of 29–40 cm.

Ku- and X-band σ^0 in each polarization combination trended positively over the course of the season, reaching a maximum at the time of largest observed SWE. Of note during the evolution were differences in σ^0 between the final two observations where larger increases in X-band were found in comparison to Ku-band. The gradual loss of Ku-band sensitivity at a higher SWE agrees with previous forward model estimates Rott et al. (2010) and highlights the synergistic benefits of a dual frequency approach under field observed conditions. Variation in the polarimetric response of the fen snow target was observed as co-polarization discrepancies throughout the campaign. The development of a significant depth hoar layer with preferential vertical grain alignment may be responsible for the elevated late season σ^0_{VV} response. Finally the magnitude of the observed σ^0 at the fen site is generally higher than previously reported values such as those found in Yueh et al. (2009) and Kern et al. (2009). Modelling experiments such as Du et al. (2010) suggest that multiple-scattering effects will be pronounced with the presence of large grains. The unique conditions found at the fen site promote such interactions and may drive an enhanced backscatter response from this snow target.

4.4.2 CASIX 2010-2011

A number of questions were generated during the inaugural deployment of UW-Scat and a second campaign was undertaken in the winter of 2010-2011 to address these. Known as the Canadian Snow and Ice Experiment (CASIX), this campaign again selected Churchill, Manitoba, Canada to investigate Ku- and X-band interactions with tundra and wetland snow targets. Seasonal experiments were modelled after Can-CSI and complimented with

Table 4.2: Observed fen site σ^0 at elevation angles of 30° and 45°. Values at each elevation angle are listed as VV/HH/VH in decibels.

Date	SWE	Ku-band		X-band	
(ISO/IEC 8601)	(mm)	30°	45°	30°	45°
2010-01-13	73	-3.8 / -3.9 / -15.9	-5.0 / -6.0 / -16.3	-5.1 / -5.8 / -19.3	-9.8 / -10.8 / -20.3
2010-02-13	67	-2.5 / -4.3 / -13.5	-4.8 / -5.6 / -14.3	-5.6 / -5.3 / -18.9	-9.1 / -9.6 / -19.4
2010-03-23	81	1.9 / 0.2 / -10.7	-2.2 / -3.7 / -11.7	-3.1 / -3.2 / -17.8	-5.6 / -7.6 / -19.2
2010-04-11	122	1.6 / 0.4 / -7.8	0.3 / -1.4 / -12.6	-1.3 / -1.3 / -13.0	-1.9 / -3.2 / -16.0

a range of destructive experiments to characterize variability within the scatterometer field of view. Experiments also attempted to address the influence of intra-regional variability in snow properties and develop an understanding of the scattering components unique to different land coverage types.

One such experiment was conducted on February 25, 2011 to gauge the influence of dense shallow tundra snow and organic soils on Ku- and X-band backscatter. UW-Scat was used to scan a tundra snow target (58.7364 N, 93.8244 W) with 39 ± 18 mm of SWE underlain with ground covering vegetation and frozen organic soil. Extensive snow sampling characterized variability within the scatterometer field of view immediately after the scan. Snow in the field of view was removed and the target was then scanned again. While efforts were made to remove all the snow in scene, small residual amounts remained. Moreover, removal of the snow from the target revealed a heterogeneous ground cover with distinct microtopographic elements. As a result it was expected that variation in backscatter would be a function of topography and SWE local to each elevation angle.

Figure 4.2 shows σ^0 at each frequency across elevation angles between 30° and 60°. Significant reductions in mean Ku-band co-polarized (6.3 ± 2.4 dB) and cross-polarized (4.0 ± 2.1 dB) backscatter were observed when snow was removed. Conversely, removing the shallow snowpack was observed to have little influence on X-band co- and cross-polarized backscatter. This experiment demonstrates a dominating X-band soil scattering contribution under shallow snow conditions. Future studies will address the influence of organic soils to aid in signal decomposition under shallow conditions typical of the Canadian tundra.

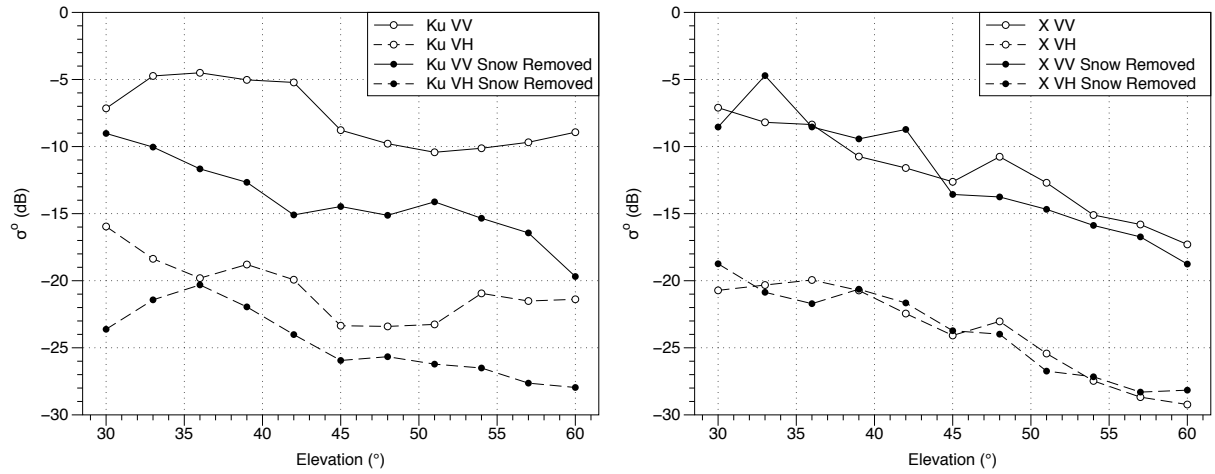

(a) Ku-band VV VH

(b) X-band VV VH

Figure 4.2: Backscatter response of snow at a tundra observation site. When snow is removed from the scatterometer field of view a significant decrease in co- and cross-polarized σ^0 is observed at Ku-band. X-band σ^0 is comparable under both conditions. The experiment was completed in a shallow tundra snow pack (39 mm SWE).

4.5 Summary

UW-Scat is a versatile platform for investigation of dual-frequency interactions with terrestrial snow and ice. It can be rapidly deployed in remote locations to collect backscatter measurements in four polarization combinations with two antenna configurations. A positioning system allows collection of observations across a user programable range of azimuth and elevation. For typical snow cover UW-Scat co-polarized SNR exceeds 13 dB while cross-polarized SNR exceeds 8 dB at elevation angles $< 75°$. Using the sled mounted configuration and a standard set of scan parameters, a minimum of 21 independent samples is obtained at 21° elevation. Collected baseband data is calibrated with internal and external methods to quantify variation in system gain and phase. Once calibrated, science ready polarimetric products including σ^0 are derived in post-processing.

Over two field campaigns UW-Scat was operated in the harsh conditions of the Canadian Tundra, collecting a novel dataset of polarimetric snow target backscatter measurements. During Can-CSI 2009-2010 repeat observations of an undisturbed snow target demonstrated sensitivity to increasing SWE in a fen environment. This experiment has shown UW-Scat to be a useful tool for investigation of seasonal backscatter trends in relation to evolving snow properties. Frequency dependent sensitivity to SWE was observed during a destructive experiment of CASIX 2010-2011. Upon removal of a shallow snowpack from the scatterometer field of view, a significant reduction in co- and cross-polarized Ku-band σ^0 was observed. A similar reduction in σ^0 was not observed at X-band indicating a lack of sensitivity to shallow snowpacks. These observations will be useful for the development of SWE retrieval algorithms in tundra environments. The dataset also contributes novel observations important to future space-borne missions such as a $CoReH_2O$. Future papers will describe in detail the influence of the seasonal scattering components using tundra and wetland study sites established during CASIX 2010-2011.

4.6 Acknowledgements

The authors would like to thank the Churchill Northern Studies Centre and the field crews of Can-CSI/CASIX for their support in the field. Special thanks to Chris Derksen, Arvids Sills, Peter Toose, Steve Howell, Nick Rutter, Ken Asmus, Andrew Rees, Kevin Kang, Jason Oldham, Nic Svacina and Alec Casey for their efforts in data collection.

The University of Waterloo scatterometer system was acquired with funding from the Canadian Foundation for Innovation and the Ontario Ministry of Research and Innovation (PI: C. Duguay, co-PI: R. Kelly). The scatterometer system was developed and built by ProSensing, Inc., Amherst, MA, in 2009. Field activities were supported in part by the

Canadian Space Agency, European Space Agency and Environment Canada. The work of J.M.L. King, G. Gunn, R. Kelly, and C. Duguay is supported by the Natural Sciences and Engineering Research Council.

Chapter 5

Seasonal dual-frequency scatterometer observation of a shallow tundra snowpack

5.1 Introduction

Innovative methods for practical retrieval of snow properties have become a priority for climatological and hydrological research communities. Evidence of this need can be found in the increasing number of studies identifying evolving physical phenomena related to snowcover variability (e.g. Cohen et al., 2012; Derksen et al., 2012a; Shi et al., 2013). Snow plays an important role in the Earth system by modulating energy flux and driving regional hydrology (Barnett et al., 2005; Cook et al., 2007). The ability to retrieve key physical properties, such as snow water equivalent (SWE), at appropriate spatial scales ($<$ 200 m), is an important step towards characterizing the role of seasonal changes in snow

mass and energy. Existing ground-based observation networks are sparse, generally lacking spatial density to characterize variability in SWE and other derivative hydrologic properties (Derksen et al., 2005; Dyer and Mote, 2006). In the absence of reliable monitoring networks, readily available satellite observations have become an important source of data in the advancement of snow property retrieval over the past 30 years.

While significant progress has been made in multi-scale observation of snow cover extent (e.g. Brown and Robinson, 2011; Hall et al., 2010), satellite-based retrieval of volumetric properties remains a challenge. Existing operational approaches, such as microwave radiometry, are inherently limited by course spatial resolution, sub-pixel mixing, and snow self-emission (Derksen, 2008; Foster et al., 2005). Active microwave remote sensing, namely radar, has emerged as an attractive compliment in the development of snow property retrieval. Much like microwave radiometry, radar at similar frequencies can penetrate dry snow volume to substantial depth (e.g. > 1 m when < 40 GHz; Mätzler, 1987). With an onboard source of illumination, radar systems benefit from improved spatial resolution, enabling time and weather independent observation at or near the spatial scale of ground measured variability. These characteristics are ideal for observing dynamic cryospheric environments where clouds, polar darkness, and complex scales of variation may otherwise render alternate approaches ineffective.

Early investigations of snow-radar interaction demonstrated backscatter sensitivity to volumetric properties under a limited set of conditions at microwave frequencies (e.g. Kendra et al., 1998; Stiles and Ulaby, 1980; Strozzi and Matzler, 1998; Ulaby and Stiles, 1980). More recently, radar technology advancement has facilitated deployment of purpose built systems to characterize interactions across a variety of previously untested terrestrial surfaces (e.g. Kern et al., 2009; Marshall et al., 2005; Morrison and Bennett, 2014; Yueh et al., 2009). Such studies have shown backscatter from terrestrial dry snow targets to be

dominated by signal originating from within the volume and/or from the underling soil surface. Changes in the dielectric and stratigraphic properties of snowcover as a result of seasonal accumulation and metamorphosis drive backscatter variability, which in principal, can be exploited for property retrieval. Commonly chosen frequencies between 8 and 18 GHz balance penetration with sensitivity to properties such as depth, density, and grain size. To leverage sensitivity across the microwave spectrum, proposed satellites missions including the European Space Agency Cold Regions Hydrology High-resolution Observatory (CoReH$_2$O) have opted for a dual-frequency (17.2 and 9.6 GHz) retrieval approach (Rott et al., 2010).

Despite global interest in radar-based retrieval, there is a distinct lack of field data to assess interactions specific to many types of seasonal snow cover. Furthermore, there have been few field studies which attempt to characterize backscatter as part of a seasonal evolution (e.g. Mätzler, 1987; Pettinato et al., 2013; Strozzi and Matzler, 1998). In response to these data gaps, the Canadian Snow and Ice Experiment (CASIX) was initiated to collect seasonal backscatter measurements across a number of previously untested Canadian sub-arctic land cover types. This paper discusses a CASIX experiment where a ground-based dual frequency (17.2 and 9.6 GHz) scatterometer system was deployed to an undisturbed snow covered tundra target. A method for repeat co-incident snow and backscatter measurements is presented. Analysis of the novel dataset is used to (1) demonstrate seasonal and spatial variation in the properties of the tundra snowpack, (2) evaluate backscatter contributions related to observed accumulation and metamorphic processes, and (3) discuss decomposition of the soil scattering contribution by removing snow from the observation site.

5.2 Data and methods

To evaluate understanding of snow-radar interactions and demonstrate seasonal response specific to a tundra environment, a dual-frequency scatterometer system was deployed near Churchill, Manitoba, Canada during the winter of 2010-2011 (Figure 5.1). Situated in the Hudson Bay Lowlands, Churchill lies at the coastal intersection of the northern treeline and southern continuous permafrost (Duguay et al., 2002; Rouse, 1991). With a multitude of sub-arctic land cover types accessible over short distances, Churchill was an ideal location to accomplish the terrestrial objectives of CASIX. Graminoid dominated tundra environments found near Churchill possess a number of distinctive features including deep organic soils, periodic surface elements (hummocks), and clustered vegetation. Snow deposition in this environment is generally shallow ($<$ 30 cm) characterized by the development of dense wind slab underlain with depth hoar of significant diameter. This combination of unique features presents an opportunity to evaluate radar interactions across a set of previously untested conditions representative of high latitude snow cover.

Between November 15, 2010 and March 3, 2011, 13 discrete backscatter observations of a terrestrial tundra target were collected along with coincident measurements of snow physical properties (58° 45' 11 N, 93° 51' 30" W). In an effort to minimize complexity, the selected site had only short standing grass vegetation ($<$ 10 cm) and was relatively flat (Figure 5.2). In doing so, sub-scan terrestrial conditions were kept as close to homogeneous as possible. A mean revisit time of 9 days was achieved over the observation period, comparable to that of a potential satellite radar mission. These measurements, coupled with continuous meteorological observations, provide the basis for evaluation of physical interactions driving seasonal variation in backscatter. The following section presents a methodology for repeat observation of local meteorological conditions, snow properties, and backscatter of an undisturbed target.

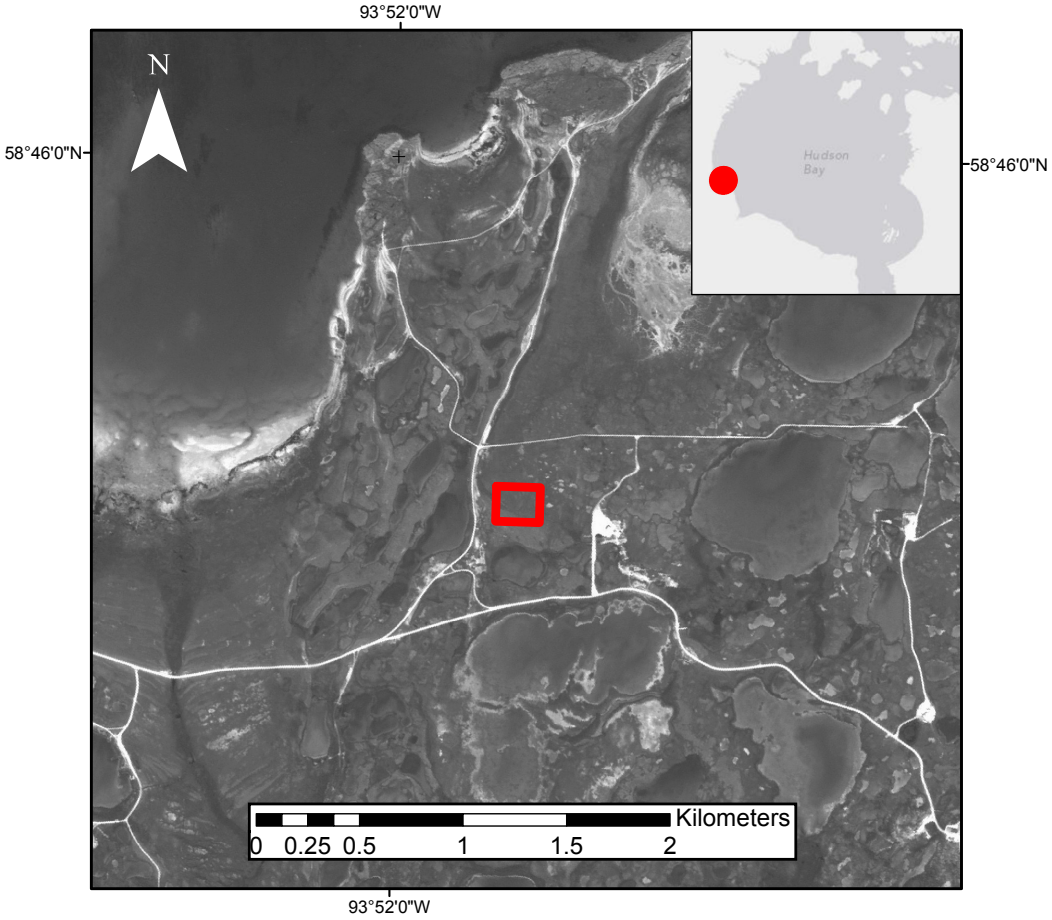

Figure 5.1: Location of tundra study site location along the Hudson Bay coast.

5.2.1 Meteorological measurements

A meteorological tower was erected 10 m northwest of the tundra observation site. Measured parameters including air temperature, wind speed, and wind direction were averaged as a 30 minute mean. An ultrasonic snow depth sensor was installed to monitor accumulation between site visits. Meteorological parameters were collected continuously from November 5 onward.

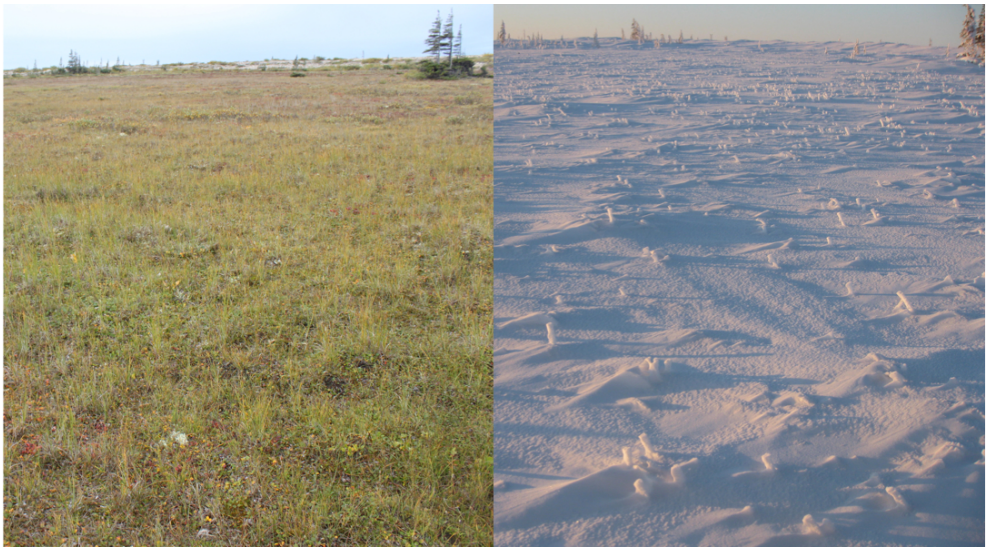

Figure 5.2: Snow free (Left) and snow covered (Right) conditions at the tundra observation site. Photographs were taken on September 5 and January 16.

5.2.2 Snow measurements

Comprehensive snow surveys were completed throughout the observation period to characterize local snow properties as a function of seasonal accumulation and metamorphosis. In order to facilitate the continuous observation of an undisturbed snowpack, surveys were carried out in an area adjacent to the scatterometer field of view, hereafter refereed to as the pit farm. A complement of pit excavation and transect sampling methods enabled description of both horizontal and vertical variability local to the observation site. Sequential sampling within the pit farm was arranged along the dominant wind direction to minimize contamination from drifting.

A standard protocol involving visual inspection and physical survey was used to excavate snow pits during each site visit (Fierz et al., 2009). Stratigraphy was assessed by describing major discontinuities in structure and hardness noting layer thickness. Density

was estimated along continuous vertical transects using a 100 cm^3 cutter and digital scale. Concurrent with density, snow temperature was measured at 2 cm intervals along the same profile. Temperatures at the air-snow and ground-snow were also recorded. Snow grain properties were estimated in field with a stereoscopic microscope and grid comparator card. Samples extracted from each layer were shaken lightly to isolate individual grains. The axial diameter of prevailing grains were estimated with a 1 mm grid.

A 100 m snow survey transect was established adjacent to the pit farm to assess horizontal variation and determine the representative nature of each pit at the local scale. Snow depth measurements were made every 0.5 m along the transect using a GPS enabled depth probe (Snow-Hydro Magnaprobe). Bulk density and SWE were estimated with pairs of ESC-30 snow core measurements made at 25 meter intervals. In total, 201 snow depth and 10 ESC-30 measurements were collected each site visit along the transect.

To evaluate heterogeneity within the scatterometer field of view, the previously undisturbed snow target was directly sampled on March 3. Two snow pits were completed at 3 and 6 m outward from the scatterometer using the standard protocol. Complex relative permittivity ($\varepsilon^{'}$ and $\varepsilon^{"}$) of the final snow pits was also measured using a Toikka Snow Fork operating at frequencies between 0.5 and 0.9 GHz (Sihvola and Tiuri, 1986). Measurements of permittivity were made vertically at two centimetre intervals. A grid of 220 snow depth and 12 ESC-30 measurements were also collected within the scatterometer footprint to determine local variability in bulk snow distribution. Snow within the field of view was then removed to expose the frozen vegetation and soil surface. The scatterometer system was redeployed to collect a backscatter measurement of the bare ground.

5.2.3 Scatterometer measurements

To measure backscatter response, a sled-mounted dual-frequency system known as the University of Waterloo Scatterometer (UW-Scat) was deployed to the tundra observation site (Figure 5.3). The polarimetric frequency modulated continuous-wave radars operated at centre frequencies of 17.2 GHz (K-Band) and 9.6 GHz (X-Band), each with a bandwidth of 0.5 GHz. During site visits, the sled mounted system was positioned and levelled within a set of survey stakes to establish consistent viewing geometry. Aboard the sled, the system operated at a height of 1.6 m, resulting in a surface projected footprint less than 1.0 m in range at elevations less than 60°. Additional UW-Scat operational parameters can be found in Table 5.1 and in King et al. (2013).

Scatterometer measurements were collected as a series of azimuth sweeps using a two-axis positioning system to direct the incident beam across the snow target. A complete set of observations consisted of 21 sweeps collected at elevations between 21° and 81° in increments of 3°. Range profiles from each azimuth sweep were averaged to leverage an increased number of independent samples, minimizing radar fade. A minimum of 45 independent samples were collected from each sweep. Co-polarized (σ°_{hh}, σ°_{vv}) and cross polarized (σ°_{vh}, σ°_{hv}) backscatter was then estimated in post-processing using the averaged range profiles and system geometry to produce a normalized radar cross section for each elevation angle observed.

Scatterometer calibrations were conducted in field using internal and external measures. Prior to each scan, a trihedral corner reflector was placed in the scatterometer far-field and isolated from its mounting hardware using microwave absorbing material. A time series of observations were collected and used to derive distortion matrices following a procedure described in Geldsetzer et al. (2007). The distortion matrices were used in post-processing

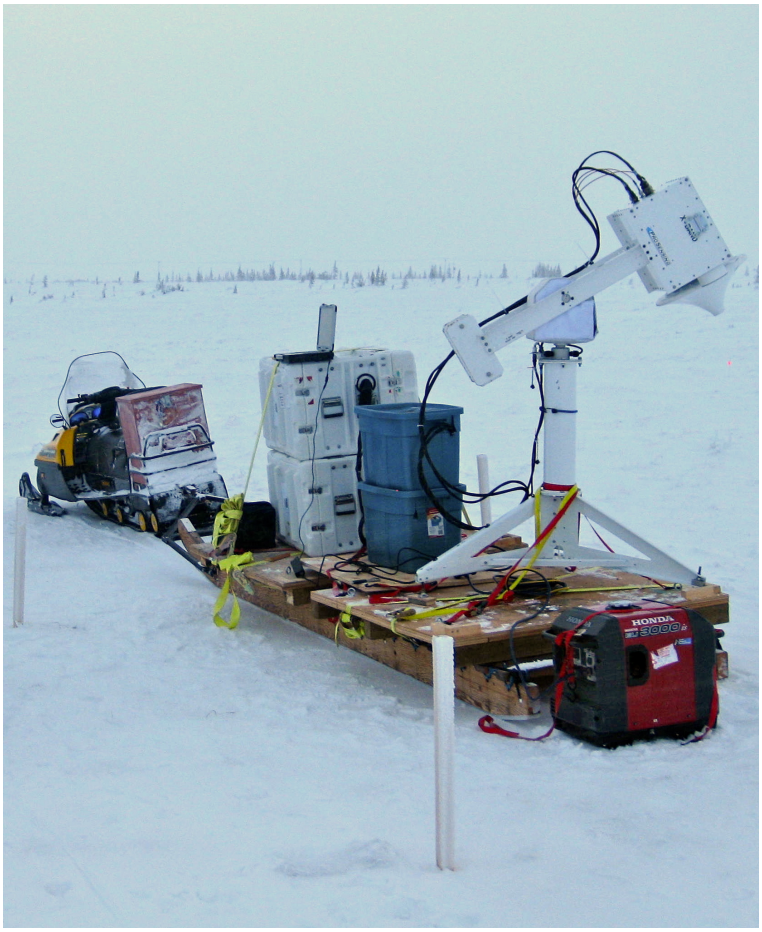

Figure 5.3: The University of Waterloo Scatterometer system (UW-Scat) deployed at the tundra site with the X-band radio frequency unit mounted.

to correct for differences in polarimetric gain and phase against reference target backscatter. In addition to the corner reflector, an internal calibration loop continuously monitored transmission gain and hardware temperature. Regardless of best efforts to stabilize the radio frequency signals, small variations in transmission gain were observed during the experiment. Observed systematic bias in transmission gain was corrected in post-processing using known coefficients derived from environmental chamber testing. Worst case estimates

Table 5.1: UW-Scat operational parameters

Parameter	X-band	Ku-band
Frequency (GHz)	9.6	17.2
Beamwidth (°)	4.3	5.6
Bandwidth (GHz)	0.5	0.5
Range resolution (m)	0.3	0.3
Sensitivity (dB m^2/m^2)	-50	-50
Polarization	VV, HH, HV, and VH	

of total error calculated from the calibration process are dependent on elevation ranging from ±2.0 dB at 21° to ±1.6 dB at 81°. Reduced errors at higher elevations are a result of the increasing number of independent samples as the ground-projected radar footprint extends in the range direction.

5.3 Results

5.3.1 Seasonal snow characterization

Seasonal evolution of the observed snowpack was driven by two primary agents: sustained winds and strong vertical temperature gradients. The result of these interacting elements was a dynamic shallow snowpack where periods of sustained grain growth were found throughout the winter. Although shallow, the snowpack provided a challenging target of analysis given its rapid but often subtle change in structure through time and space. Characterizing variation in local meteorological and metamorphic properties was an important step towards decomposing physical interactions influencing backscatter at the tundra site.

Local snow properties

With minimal vegetation and no surrounding relief, the tundra site was exposed to Arctic winds across Hudson Bay. As a result, blowing snow was an important consideration where sustained events are known to modify tundra class snow over short periods of time (Pomeroy and Li, 2000; Sturm et al., 1995). At the meteorological station, prevailing North-West winds averaged 5.0 m s^{-1}, frequently exceeding 10.0 m s^{-1}. Threshold speeds for dry snow transport range from 4.0 to 11.0 m s^{-1} placing a majority of the experiment period in plausible territory for rapid redistribution and sublimation (Li and Pomeroy, 1997). The record of accumulation measured at the meteorological tower demonstrates the influence of local wind where precipitation events were quickly eroded and total depth was limited to approximately 10.0 cm (Figure 5.4). Conversely, notable increases in depth were few in number and associated with low wind speed in late December and early January. The demonstrated redistribution of snowfall is consistent with tundra environments where vegetation height is a primary driver of retention (Clark et al., 2011; Essery and Pomeroy, 2004). Lacking structure beyond ground covering vegetation or significant variation in topography, accumulation around the meteorological tower was restricted to the shallow depths observed with the sonic depth sounder.

Extending from the point to plot scale, depths along the 100 m transact were also moderated by wind processes. In agreement with meteorological tower measurements, the largest increases in depth occurred in late December and early January, coinciding with periods of relative calm (Table 5.2). The observed increase plateaued shortly thereafter and was sustained through the end of the experiment. During this final period, mean depth along the transect reached a seasonal maximum of 17.1 cm. Changes in depth along the transect largely corresponded with variation in dynamic wind features and topography,

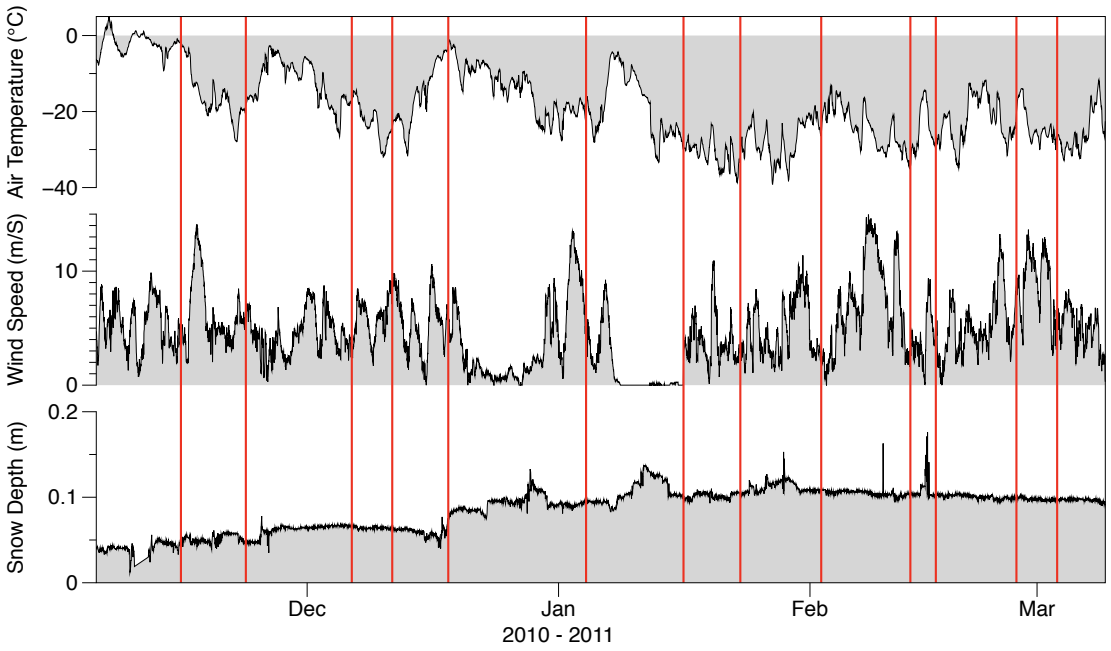

Figure 5.4: Air temperature (top), wind speed (middle), and snow depth (bottom) as measured at the co-located meteorological tower. Red lines indicate timing of site visits.

especially hollows between hummock structures. Accumulation around these features often exceeded the observed mean by double (Figure 5.5). Snow depth standard deviations ranged from 2.5 to 6.5 cm over the 13 observation periods, increasing linearly with depth ($R^2 = 0.76$, $n = 13$, $p < 0.0001$). As a whole, these measurements demonstrate the presence of significant variations relative to total depth over short distances.

As this study relies on a seasonal observation approach, variability in density was expected given the seasonal metamorphosis of terrestrial snow. Individual measurements of bulk density collected over the course of the experiment fit this expectation ranging from 103 kg m^{-3} in November to 371 kg m^{-3} by March. Together, the 120 bulk density measurements comprise a normal distribution with a mean of 226 kg m^{-3} and standard deviation of 54 kg m^{-3}. While early measurements extended the distribution range, a steady state

Table 5.2: Bulk snow properties measured along the 100 m sampling transect. During each site visit depth was measured every 50 cm (n=201) along the transect and density was measured in pairs every 25 m (n=10). SWE_c was estimated using only ESC-30 measurements and SWE_t was estimated using transect mean depth and density.

Date	Pit	Depth				Density	SWE_c	SWE_t
		Mean (cm)	St.Dev (cm)	Max (cm)	Min (cm)	Mean (kg m^{-3})	Mean (mm)	Mean (mm)
2010-11-15	A	7.7	3.9	20.4	1.7	—	—	—
2010-11-23	B	5.4	2.8	17.9	0.0	160	8.9	8.6
2010-12-06	C	6.7	2.5	12.5	2.3	190	16.8	12.1
2010-12-11	D	7.6	3.1	20.3	1.8	239	16.4	18.1
2010-12-19	E	12.1	4.0	24.1	4.0	233	24.5	28.2
2011-01-04	F	14.6	4.4	27.4	5.0	247	28.4	36.1
2011-01-16	G	16.2	5.1	30.2	5.9	227	28.6	36.9
2011-01-23	H	16.2	4.4	29.5	6.7	234	26.9	37.9
2011-02-02	I	16.5	4.4	27.2	6.9	227	31.5	37.6
2011-02-13	J	16.4	5.1	34.8	7.0	225	34.7	36.9
2011-02-16	K	16.4	6.2	34.5	5.4	234	30.9	38.4
2011-02-26	L	17.1	5.1	31.8	6.2	239	34.1	39.4
2011-03-03	M	16.1	5.1	33.5	5.7	265	29.4	42.5

was quickly established along the transect as shown in Table 5.2. Rapid conversion of early accumulation (< 150 kg m^{-3}) to wind slab (> 200 kg m^{-3}) and lack of new snowfall were primary drivers of this process. This conversion dominated as early as December 11 where the transect mean density entered a range of narrow values for the remainder of the experiment (227 to 265 kg m^{-3}). Spatial variability was conservative where standard deviations along the transect were consistently less than 70 kg m^{-3}, accounting for variability between 6% and 29% of mean bulk density. These measurements agree with variability described in larger datasets by Jonas et al. (2009) and Sturm et al. (2010) but fail to reach mean densities reported in Derksen et al. (2009) and Rees et al. (2013) for tundra snow at higher latitudes.

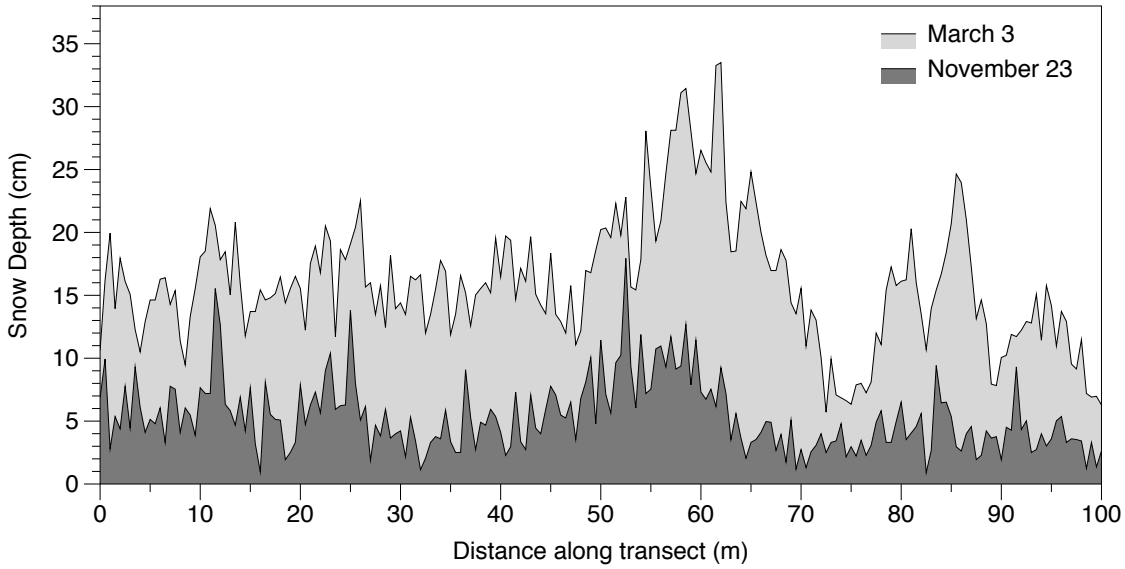

Figure 5.5: Snow depth along the 100m sampling transect on November 23 and March 3.

SWE is product of depth and density, and at the tundra observation site, was limited by the range of its quotients. A strong functional relationship was found between SWE and depth along the transect at the tundra site ($r = 0.98, n = 288, p < 0.0001$). Given this relationship, separate estimates of SWE were made using individual ESC-30 cores (SWE_c) and mean transect density (SWE_t). The latter exploits the strong relationship between SWE and depth in order to convert each point along the transect such that:

$$SWE_i = 0.01 \cdot d_i \cdot \overline{\rho_s} \tag{5.1}$$

where i represents ith measurement along the transect, d is depth, $\overline{\rho_s}$ is the mean bulk density from ESC-30 cores and ρ_w (Sturm and Wagner, 2010). To directly compare the stand alone ESC-30 measurements against estimates made with mean transect density, SWE_i along the transect was averaged to produce SWE_t for each date.

Both estimates of SWE increased over the course of the experiment reaching a maximum near its conclusion. Here SWE_t was the larger estimate for a majority of the experiment with a maximum of 42.5 mm. Operator bias in the placement of ESC-30 measurements was likely responsible for lower estimates of SWE_c where wind features may have been interpreted as outliers. For this reason quantitative descriptions of SWE hereafter will refer to SWE_t as derived with the combination of mean ESC-30 density and transect depths.

5.3.2 Stratigraphy and metamorphism

Excavations within the pit farm featured a shallow, yet complex, arrangement of layers stratified by iterations of wind action and temperature gradient metamorphosis. Horizontal structure and layer thickness were temporally and spatially variable because of the dominance of redistribution processes rather than precipitation input. Pits excavated within the farm increased in depth from slightly less than 5 cm to a maximum of approximately 20 cm (Figure 5.6). When compared with corresponding transect means, each pit depth falls within 1 standard deviation of the mean transect depth. Changes in topography and ground covering vegetation within the pit farm reproduced variation similar to the transect and ultimately influenced layering based on pit placement. This lateral heterogeneity is common to tundra environments where wind and microtopography can produce stratigraphic variability at scales of up to 100 m (Sturm and Benson, 2004).

Layering excavated within the pit farm increased with depth to a maximum of 8 layers, consistent with end of season tundra snow conditions (Table 5.3; Derksen et al., 2009). Consistent amongst the excavated pits was a basal layer composed entirely of depth hoar. This layer accounted for, on average, 59% of total depth and was established as a prevalent feature from November 23 forward. Initial precipitation events trapped by vegetation and

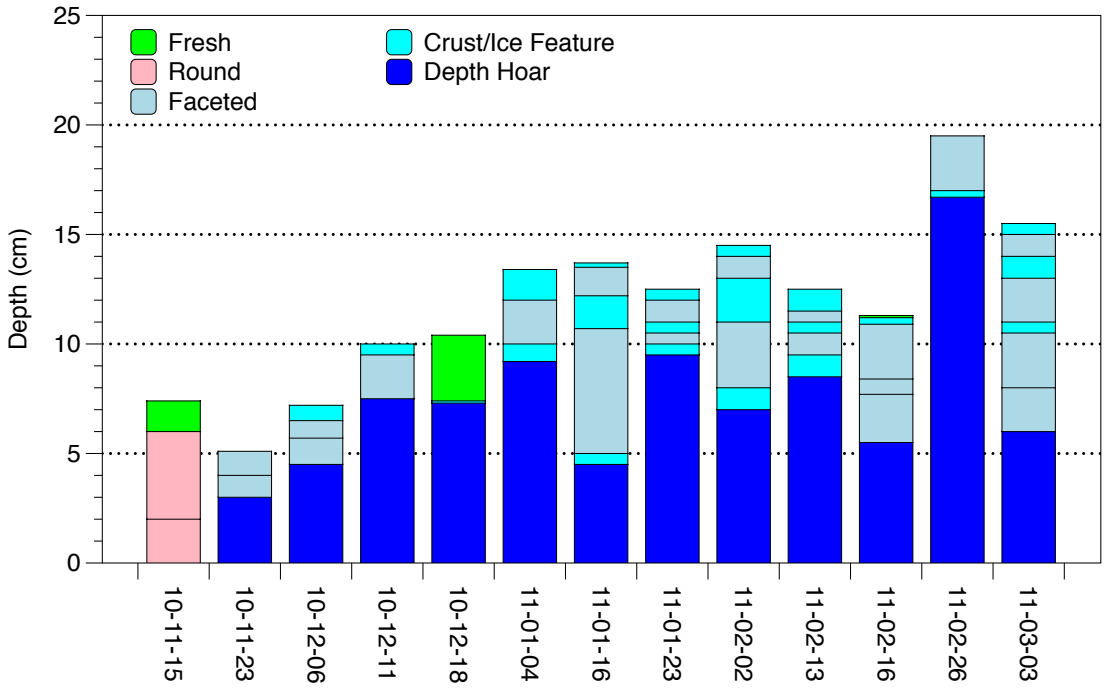

Figure 5.6: Snow stratigraphy excavated within the pit farm.

microtopography quickly converted to depth hoar as air temperatures rapidly decreased. Gradients in excess of -0.2°C cm^{-1} between the air and ground interfaces were common, leading to sustained periods of kinetic grain growth (Sturm et al., 1995). Grain structures within the basal layer often presented as chains with preferential vertical orientation as a result of substantial vapour transport. Columnar and cup shaped depth hoar composing the layer ranged in major axis diameter from 0.5 mm in the early season to over 6.0 mm by the end. Based on depth hoar residency observations made by Pinzer et al. (2012) and the sustained temperature gradients observed throughout the experiment, it can be assumed that nearly each observation of the basal layer was a unique permutation of arrangement and structure.

Table 5.3: Summary of stratigraphy and snow properties observed within the pit farm. See labels in 5.2 for corresponding pit dates.

	A	B	C	D	E	F	G	H	I	J	K	L
Layers	3	3	4	3	3	4	6	7	8	8	5	4
Depth (cm)	7.5	5.1	7.2	10.0	10.5	13.4	12.5	13	14.5	12.5	8.9	19.5
Avg layer (cm)	2.5	1.7	1.8	3.3	3.5	3.4	2.1	1.9	1.8	1.5	1.8	4.9
SWE (mm)	13.9	6.9	13.0	18.5	22.3	28.9	24.8	26.5	30.5	29.1	21.7	45.2
ρ (kg m^{-3})	185	135	180	185	210	235	202	210	207	228	258	226
New fraction	1.00	0.00	0.00	0.00	0.29	0.00	0.00	0.00	0.00	0.00	0.01	0.00
Slab fraction	0.00	0.41	0.28	0.20	0.00	0.25	0.58	0.24	0.41	0.20	0.34	0.13
Hoar fraction	0.00	0.59	0.63	0.75	0.69	0.69	0.36	0.72	0.48	0.68	0.62	0.86
Icy fraction	0.00	0.00	0.09	0.05	0.02	0.06	0.06	0.04	0.11	0.12	0.03	0.01

Depth hoar in the pit farm was overlain with a number of thin slabs initially composed of wind rounded grains (0.1-0.5 mm). As the season progressed, a sequence of alternating high density crust and softer slabs developed representing periods of varied wind speed and accumulation. Thickness and texture of these features changed drastically from start to end as a result of the snow metamorphic processes. Gradients were so strong that these features often metamorphosed into layers of cohesive faceted crystals. Such so called slab-to-hoar conversions have been referred to as indurated, as they are distinguished from basal depth hoar by their increased hardness and distinct lack of porosity (Derksen et al., 2010). By this process, wind rounded grains became faceted but remained higher in density than the underlying layers. Unlike the basal depth hoar layer, preferential orientation of the grain structure was not observed. Overall, the snowpack was nearly entirely metamorphosed into faceted forms by temperature gradient growth from an early point in the experiment.

5.3.3 Relating local snow properties to the scatterometer field of view

At the conclusion of the experiment, snow in the scatterometer field of view was sampled to evaluate sub-scan variability in relation to the previously collected measurements adjacent to the field of view. Across the 15 m by 20 m sampling grid 220 measurements were collected with a mean depth of 15.1 cm and standard deviation of 2.9 cm. Across the same spatial domain a mean density of 246 kg m^{-3} was estimated from 12 ESC-30 cores. These observations place the bulk properties of the scatterometer snow target within the local distributions described by proxy pit and transect observations on March 3 (Table 5.4). More importantly, variation of bulk properties measured within the field of view are comparable with levels observed along the transect.

Table 5.4: Comparison of snow properties measured within the scatterometer field of view (FOV) and along the adjacent snow survey transect on March 3.

	Depth (cm)				Density (kg m^{-3})			
Location	Mean	Min	Max	St Dev	Mean	Min	Max	St Dev
FOV	15.1	6.5	23.1	2.9	246	208	269	19
Transect	16.0	5.7	33.5	5.2	265	205	308	28

Snow pits excavated within the field of view revealed features similar to those observed in the pit farm including contrasting slab and depth hoar components. Figure 5.7 shows horizontal variability in stratigraphy, density, temperature, grain size, and ε' as observed at 3 m into the field of view. As expected, the basal depth hoar layer within the field of view represented a substantial portion of the total depth. Within the basal layer, grains were found with major axis diameters of up to 6 mm oriented in vertical chains along the direction of vapour transport. Density and hardness in the depth hoar layer were not

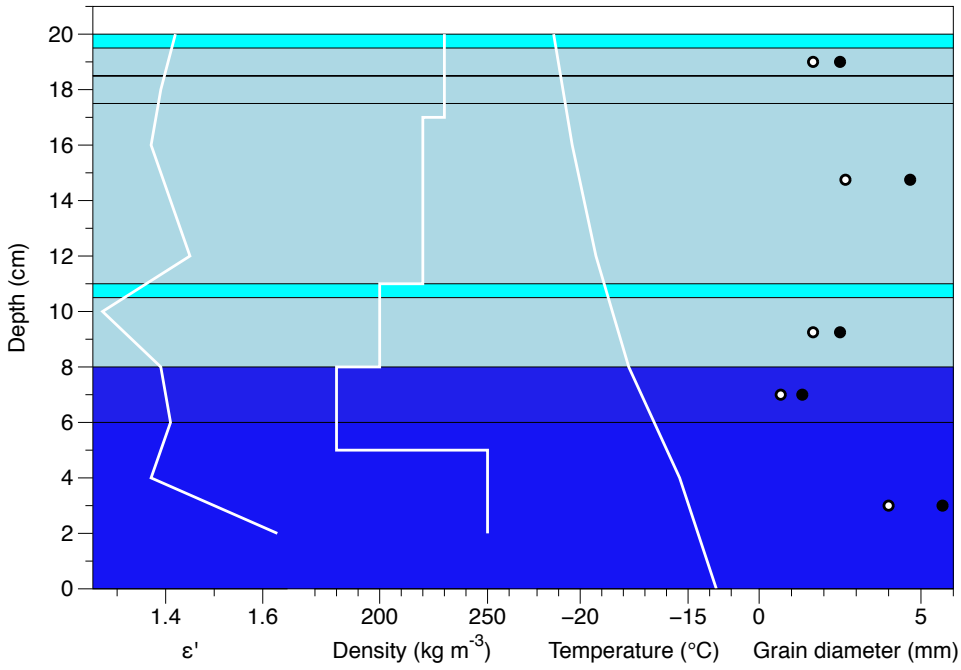

Figure 5.7: Stratigraphy and snow properties excavated 3 m into the scatterometer field of view on March 3. Grain diameters show major (Solid) and minor (Hollow) axis measurements. See Figure 5.6 for description of colours.

uniform, increasing significantly with depth. Towards the base of the pack an increase in permittivity was observed because of the coupled influence of the increased density and integrated soil surface ε'. The overlying slab layer contained several discontinuities of density and texture interpreted as relic wind crusts. While these features may not have been captured by the larger density cutter, a discontinuation in ε' was identified mid pack surrounding a buried wind crust. The snow volume as a whole contains numerous elements which present as distinct changes in permittivity, density, and stratigraphy all of which have potential to influence backscatter as a result of the dielectric discontinuities and variability they induce.

5.3.4 Backscatter response and relationship with *in situ* snow properties

Angular response

Backscatter described in this study is a function of the properties of the observing instrument and the evolving physical condition of the target. To demonstrate the cumulative influence of these properties, the angular response of σ^0 is first evaluated for contrasting target conditions at the start of the campaign and at maximum SWE (November 15 and February 26). The four panels in Figure 5.8 show backscatter signatures for each date, frequency, and polarization combination (e.g. Ku- and X-band σ^0_{vv}, σ^0_{vh}, σ^0_{hv}, σ^0_{hh} as a function of elevation angle). The gentle elevational response of σ^0 common to each plot is indicative of an electromagnetically rough target, typical of a snow covered terrestrial surface (Ulaby et al., 1984). Upon initial observation of the snow target, slope and magnitude of the co-polarized response at both frequencies were comparable at elevations of $< 51°$. At greater elevation angles, the slope of X-band response increased relative to Ku-band for the initial shallow snow conditions.

By February 26, a larger volume of snow was present, the underlying soils surface was frozen, and the backscatter signatures from the target had changed. Given that the operating parameters and geometry of the scatterometer were held constant, measured variation in σ^0 can be expected to contain information about the physical and dielectric properties of the snow covered terrain. An observed increase in Ku-band co-polarized backscatter provides the strongest point of contrast between the two dates. Across elevation, mean differences of 4.2 and 3.4 dB, easily separated each the co-polarization responses. Differences in magnitude were largely independent of elevation with a modest standard deviation of 1.6 dB across the full range. A smaller observed difference in σ^0_{hh} corresponded with a

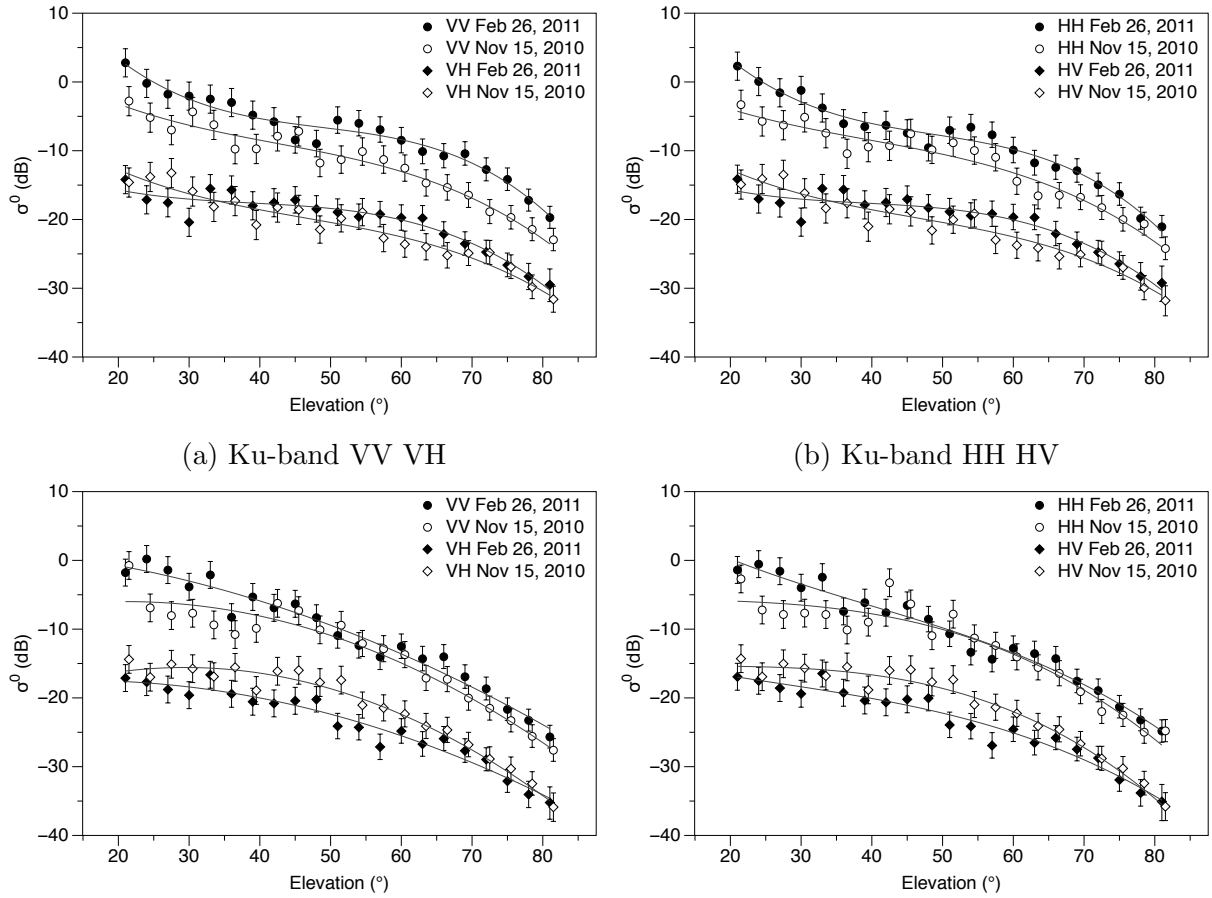

(a) Ku-band VV VH

(b) Ku-band HH HV

(c) X-band VV VH

(d) X-band HH HV

Figure 5.8: Angular response of σ^0 measured February 26 (Soild) and November 15 (Hollow). Error bars show worst case total error at each elevation angle. Cubic fit lines have been added for illustrative purposes.

positive co-polarization ratio ($\sigma^0_{vv}/\sigma^0_{hh}$) at the time of the second observation. Lower σ^0_{hh} was particularly apparent at elevations $> 50^\circ$ where specular reflection from horizontal elements including the soil surface appear to dominate the response rather than the snow volume.

Co-incident X-band measurements made at the tundra site did not replicate the distinct co-polarized separability observed at Ku-band. The largest difference in σ^0 appeared closer to nadir, rapidly decreasing with elevations greater than 40°. With declining co-polarized σ^0 at steeper elevations, an elevational dependent relationship appeared between frequencies where the shorter wavelength Ku-band was consistently higher than X-band with the deeper snowpack. Unlike the slightly positive co-polarization ratio measured at Ku-band, the X-band response was again measured near unity despite the changes in snow volume and soil status.

Cross-polarized returns from the terrestrial target were much smaller in magnitude at both frequencies. Ku-band σ^0_{vh} and σ^0_{vh} were on average 9.4 dB lower than the co-polarized response at the start of the experiment. At max SWE, this separation increased to 12.7 dB highlighting the much stronger increase in co-polarized response despite limited accumulation. Between the two observation dates, the Ku-band cross-polarized response increased by approximately 1 dB. Separability of the cross-polarized response was elevation dependent, maximizing near 60° before quickly levelling. Shallow depths relative to wavelength were a likely a limiting factor to depolarization (Kendra et al., 1998). Cross-polarized X-band signatures showed that early season observations depolarized in greater magnitude than at maximum SWE. With known increases in snow volume and therefore scattering centres, the observed reduction in cross-polarized σ^0 suggests a complex X-band interaction involving not only snow properties, but likely also a significant sensitivity to underlying soil conditions.

Seasonal backscatter response

A time series of radar observations were collected to evaluate the seasonal co-evolution of backscatter with snow properties at the tundra site. In an effort to simplify analysis

and reduce unwanted variation resulting from target inhomogeneities, estimates of σ^0 were averaged for elevational ranges between 30° and 45°. In Figure 5.9, the seasonal evolution of σ^0 was split into two time series representing each of the collected frequencies and polarization combinations (σ^0_{vv}, σ^0_{vh}, σ^0_{hh}). Error bars were added to show standard deviation within the described elevation range.

Much like in the angular responses, distinct trends in σ^0 were found at each frequency in the seasonal evolution. At Ku-band, a positive trend in co- and cross-polarized backscatter persisted throughout the experiment. Averaged Ku-band σ^0_{vv} ranged from approximately -8.6 dB to a maximum of -2.9 dB on February 13. Similarly, σ^0_{hh} ranged from -8.5 dB to -3.5 dB over the same period. Despite only a small seasonal change in depth ($\approx$ 11 cm), a large dynamic range of σ^0 was measured at nearly 5 dB. The observed increase in σ^0_{vv} responded linearly to the relatively small change in depth ($r^2 = 0.84$, n = 13 , $p < 0.001$). Measurements at σ^0_{hh} were also sensitive to depth, albeit with lower coefficient of determi-

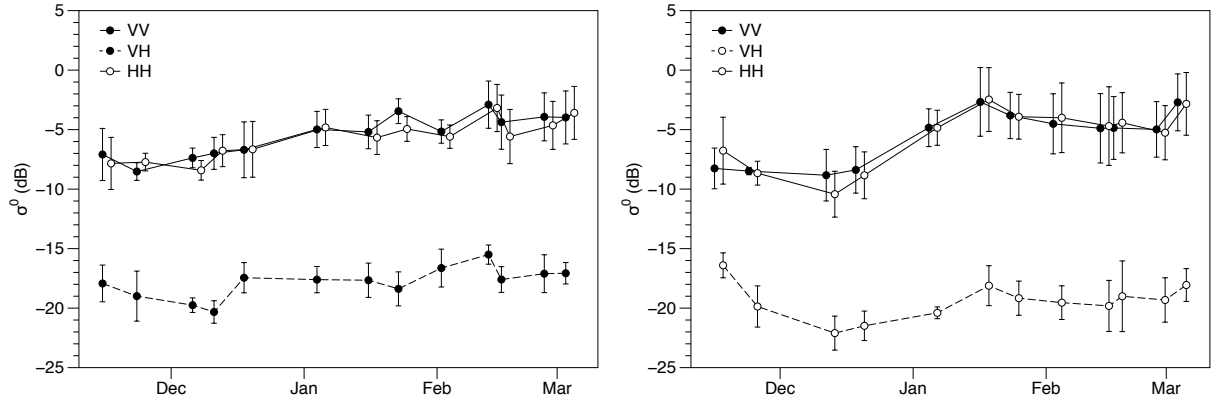

(a) Ku-band VV HH VH

(b) X-band VV HH VH

Figure 5.9: Seasonal Ku- (a) and X-band (b) backscatter response of the snow-covered tundra terrain. Bars show standard deviation within the averaged elevation angle range. Measurements of σ^0_{vv} and σ^0_{hh} are offset by one day to improve readability. Only cross-polarized σ^0_{vh} is shown as σ^0_{hv} was consistently within 0.1 dB of agreement.

nation ($r^2 = 0.74$, n = 13 , $p < 0.001$). The reason for increased sensitivity in vertical polarization was not immediately clear, but observations showed a consistent positive co-polarization ratio indicating preferential vertical scatter throughout the experiment. This finding was contrary to an expected increase in σ^0_{hh} where observed increase in snow layers could have produced a significant response (Du et al., 2010). The higher σ^0_{vv} visible in the latter part of the experiment may be related to the development of depth hoar chains preferentially oriented as a result of sustained vertical vapour transport.

Cross-polarized Ku-band σ^0_{vh} from the snow target was measured across a much smaller range of values between -20.4 dB to -18.7 dB. Nevertheless, a moderate linear relationship with depth was also found across the muted range of cross-polarized backscatter values ($R^2 = 0.57$, n = 13 , $p < 0.001$). As only a small increase in depth was measured, seasonal variation in depolarization could be attributed to the significant and sustained growth of grains in the the prevalent depth hoar layer (Du et al., 2010; Tsang et al., 2007; Xu et al., 2010). Such conditions could provide for increased multiple-scatter as non-spherical depth hoar grains approach the relative size of the interacting wavelength.

In contrast to the distinctive Ku-band evolution, X-band backscatter was characteristic of a series of discrete response periods. The time series of observations was separated into three general period characterized by early season stability, a strong increase during January, and a gradual decline through February into March. From the start of the study to December 18, σ^0_{vv} was measured across narrow range of values between -9.2 and -8.5 dB. Small decreases in σ^0_{hh} over the same period resulted in a extended range between -10.7 and -7.3 dB. By January 4, co-polarized backscatter had risen substantial by approximately 4 dB from the previous measurement. After reaching a maximum on January 16, co-polarized backscatter decreased for several weeks before stabilizing below the January 16 maximum.

Of note during the final period were large X-band backscatter standard deviations across elevation and a co-polarization ratio near unity. This was a departure from early season observations where a mix of positive and negative co-polarization ratios were observed in addition to much smaller standard deviations. The X-band cross-polarized evolution also provides additional information about the previously discussed elevated early season observations. Here, a rapid decline in σ^0_{vh} occurred, descending to a minimum in early December. Over the same period, surface soil conditions rapidly changed from an initial isothermal state with visible water to temperatures below -20° in early December. Rapid freezing of saturated organic surface soils and the observed decline in backscatter point toward a significant influence of early season soil properties. Lacking measurements of ground permittivity a definitive conclusion cannot be made about the influence of soil properties on backscatter.

The seasonal evolution of backscatter at the tundra site contained a wealth of information at both frequencies that may assist in the retrieval of high value snow properties including SWE. A strong linear relationship was observed in each Ku-band polarization combination as SWE increased at the tundra site (Figure 5.10). Ku-band σ^0_{vv} and σ^0_{hh} responses showed an increase of approximately 1.3 dB ($R^2 = 0.80$, n = 13, $p < 0.001$) and 1.2 dB ($R^2 = 0.79$, n = 13, $p < 0.001$) for every 1-cm change in SWE. The Ku-band cross polarized response was less sensitive to the shallow accumulation with 0.8 dB for every 1-cm change in SWE ($R^2 = 0.50$, n = 13, $p < 0.001$). These results demonstrate Ku-band sensitivity to small changes in SWE across a narrow range of depths. This is very encouraging for the development of Ku-band tundra snow property retrievals where lack of significant accumulation requires sensitivity to small changes produced by other environmental agents including wind. Unsurprisingly, linear regression was not appropriate to describe the X-band co-polarization response in relation to SWE. The complex relationship

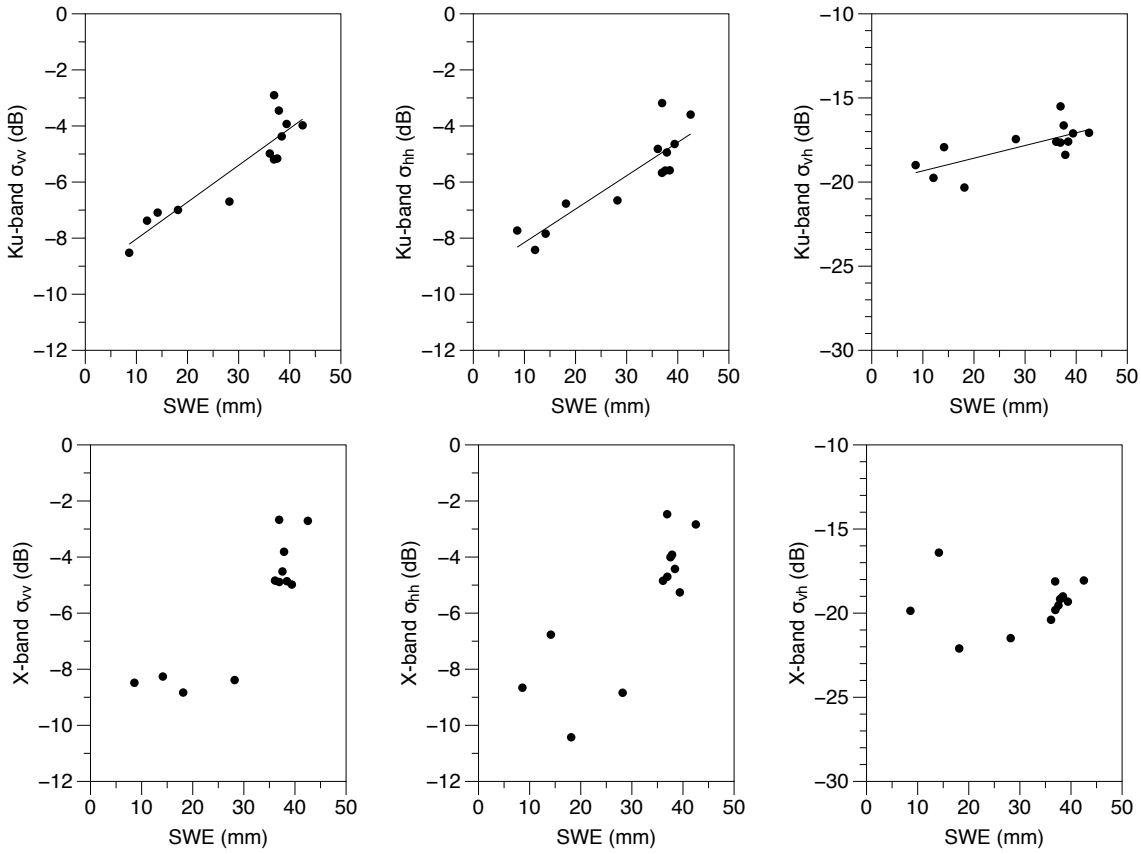

Figure 5.10: Comparison of mean 30° to 45° backscatter and *in situ* measurements of SWE. Fit lines are linear.

with SWE presents two distinct sub-populations before and after the increase observed in January. With known changes in temperature and frozen status of the underlying soil, the longer X-band wavelength likely varied to a larger degree with changes in soil until snow grains had grown sufficiently. Without detailed knowledge of the soil properties a strong conclusion cannot be made about magnitudes and timing of the change in scattering components.

Snow excavation

While the diagnostic utility of the seasonal observation approach is demonstrated above, it did not inherently lend itself to decomposition of scattering components from the snow covered terrain. To separate snow and soil contributions, a practical experiment was completed where snow was excavated from the field of view at the end of the experiment. In doing so, a volumetric response was quantified for each frequency and polarization combination. While time consuming to undertake, this experiment provided definitive evidence of scattering contributions which otherwise could only be addressed with speculation. In execution, it was not practical to remove snow for the full elevation range, limiting observations to those between 20° and 57°.

Snow free measurements made on March 3 confirmed co- and cross-polarized sensitivity to a snow volume at the tundra observation site (Figure 5.11). When the snow was removed, Ku-band σ^0_{vv} was reduced on average by 6.4 dB across elevation with a similar reduction in σ^0_{hh}. A substantial cross-polarized reduction of 6.0 dB in σ^0_{vh} was also observed. Each reduction in backscatter accounted for more than 70% of the linear power returned from the target in their corresponding polarization channels. When compared with the early season radar observations, the bare frozen ground observations were found to be lower in magnitude than the end of season excavated response. The change in backscatter between the two observations suggests sensitivity to the full range of snow conditions encountered and agrees with the previously discussed Ku-band rates of sensitivity. Additional study will be needed to quantify the influence of soil moisture and roughness in these early season interactions.

At X-band a smaller decrease σ^0_{vv} of 4.9 dB was observed when snow was removed from the tundra target. Cross-polarized returns were reduced by 3.8 dB. The reduction in co-

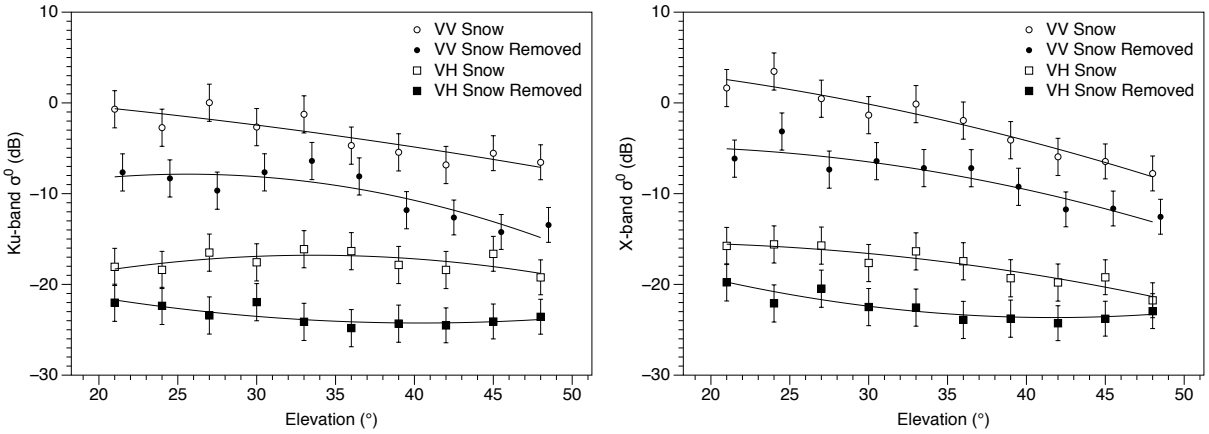

Figure 5.11: Ku- and X-band backscatter measured at the static tundra site before and after snow was removed on March 3. Error bars show total positive and negative error. For clarity only vertical polarization channels are shown. Cubic fit shown for illustrative purposes.

and cross-polarized backscatter shows a stronger sensitivity at X-band to the snow volume than in a similar experiment reported in King et al. (2013). The excavated late season snowpack consisted of a larger volume than the previous experiment, but perhaps more importantly possessed a substantial depth hoar layer composed of larger grains (> 6 mm). These findings suggest that X-band sensitivity to snow properties including SWE and depth may change as a result of seasonal metamorphic processes.

5.4 Discussion and conclusions

To accomplish the first objective of this paper, a methodology for seasonal study of an undisturbed snow target was presented. Using proxy pit and transect methods, a time series of measurements was made to characterize evolving snow properties within a protected scatterometer field of view. The coastal location and open nature of the site provided

ideal conditions for rapid wind transportation and iterative layering of the accumulated pack. The resulting configuration was characterized as a shallow yet complex arrangement of snow stratigraphy controlled by contrasting wind and temperature gradient processes similar to other measurements in the area by Kershaw and McCulloch (2007) and Derksen et al. (2012b). Steep temperature gradients observed from an early point in the experiment drove the rapid development of a prevalent basal depth hoar layer. Sustained exposure to these environmental conditions produced grains of significant diameter ($>$ 6 mm) in addition to faceted grains throughout an overlying wind slab (indurated hoar). The snow conditions characterized in these observations provided a unique opportunity to evaluate radar-snow interactions under natural conditions previously unaddressed in literature.

The second objective sought to compare co-incident backscatter and snow measurements made over the course of a winter season to improve understanding of snow-microwave interactions in a natural tundra environment. The deployed scatterometer system was used to collect 13 independent observations of an undisturbed snow covered terrestrial target. Analysis of the angular and seasonal response showed variation related to the evolving target and potentially desirable sensitivity to accumulation and metamorphic process. Despite the shallow range of snow depth and SWE encountered, a large dynamic range of σ^0 was observed at both frequencies. Of particular interest were the co- and cross-polarized Ku-band responses which showed strong seasonal relationships with depth and SWE. While few studies were available for comparison, sensitivity to SWE and the magnitude of Ku-band σ^0 were higher at similar depths than those reported in airborne 13.5 GHz measurements made as part of CLPX-II in Colorado and airborne 15 GHz measurements collected as part of HeliSnow 2007-2008 in Austria (Kern et al., 2009; Yueh et al., 2009). The unique snow conditions encountered may explain the amplified response where various models have consistently suggested that grain size and shape are significant modifiers of microwave

backscatter (Du et al., 2010; Xu et al., 2010, 2012). With grain diameters larger than 6.0 mm in the lower layers of the pack, clustering of those grains, and a dominant hoar fraction, conditions were ideal for a strong Ku-band volumetric response from the shallow tundra target. Further study and modelling efforts will be needed to quantify the influence of grain size and to determine the potential for saturation of the Ku-band signal under shallow snow conditions with a large depth hoar fraction which is typical of tundra environments.

At X-band, the response from the snow-covered tundra lacked a consistent seasonal trend. After a period of early season stability, the X-band co-polarized response increased considerably in January before declining through the end of the experiment. This response contrasted with the positive linear Ku-band seasonal progression, indicating additional interaction complexities not previously considered. In theory, the longer X-band wavelength should have penetrated the shallow tundra snow with ease soliciting a dominant response from the vegetation and soil. In previous satellite-based X-band study, this assumption was shown to be valid where depths of 60 cm or greater were required to generate volume scattering sufficient for the retrieval of snow properties in an alpine environment (Pettinato et al., 2013). The large increase of σ^0 in January suggests that sensitivity to scattering components may vary seasonally as residual soil moisture freezes and snow metamorphic processes produced grains of significant diameter. Without *in-situ* measurements of the soil dielectric properties, it was not possible to decompose the scattering contributions. In the future, seasonal thermodynamic shifts of the underling soil will become a key consideration when observing shallow snow targets.

The final objective of the study required removal of snow from the scatterometer field of view to delineate volume and surface responses. When snow was removed, Ku-band and X-band backscatter dropped significantly in all polarization combinations. This result

provided conclusive evidence of the previously hypothesized snow volume sensitivity at the tundra observation site. The largest reduction in backscatter was observed at Ku-band σ^0_{vv}. A smaller but significant reduction in X-band co-polarized σ^0 was also observed. This observation at X-band again highlighted the complex interaction involved with the longer wavelength where late season snow properties created conditions for increased volume interaction.

The results presented here provide novel snow and backscatter observations for a previously unevaluated environment. The seasonal approach used in this study allowed repeat observation that emulated the revisit frequency of a potential satellite mission and allowed observation of seasonal accumulation and metamorphic processes. Analysis of the seasonal backscatter evolution support the ground-based retrieval of depth and SWE using Ku-band (17.2 GHz) co- and cross-polarized responses in tundra environments. Despite the observed complexities at X-band, multi-frequency approaches are still favourable when the expected range of snow properties is wide by providing contrasting ranges of sensitivity, avoiding saturation (Koh et al., 1996; Marshall et al., 2004). Future studies will be needed to explore X-band observations over a larger range of snow properties with detailed soil observations to definitively explore its utility in tundra environments. Moreover, exploration of polarimetric decompositions may help to refine understanding of snow volume contributions.

5.5 Acknowledgements

Field activities completed as part of CASIX were supported by the European Space Agency, Natural Sciences and Engineering Research Council, and Environment Canada. Thanks to Arvids Silis, Chris Derksen, Chris Fletcher, Cristina Surdu, Dave Halpin, Homa Kheyrol-

lahpour, Jason Oldham, Mel Sandells, Nic Svacina, Nick Rutter, Niina Luus, Peter Toose, Ryan Ahola, Shaojie Zhao and Steve Howell for their efforts in the field. Logistical support was provided by the Churchill Northern Studies Centre. Thanks to Chris Derksen (Environment Canada) for helpful comments on an earlier version of this manuscript. UW-Scat was developed with funding from the Canadian Foundation for Innovation and the Ontario Ministry of Research and Innovation. The work of J.M.L. King, R. Kelly, and C. Duguay was supported by the Natural Sciences and Engineering Research Council of Canada.

Chapter 6

Spatiotemporal influence of tundra snow on Ku-band backscatter

6.1 Introduction

In the microwave spectrum, changes to the dielectric and physical properties of snow can influence directional scattering components, providing tangible quantities from which to derive information (Ulaby et al., 1984). Given the dynamic nature of terrestrial accumulation and metamorphosis, the measured microwave response is not only a function of aggregate snow properties such as snow water equivalent (SWE), but often of layer order and lateral snowpack heterogeneity (Colbeck, 1991). In practical application, the complexity of these interactions are compounded when scales of horizontal variation are considered. The influence of snow property variability local to an observing instrument can be significant where placement and thickness of dielectric discontinuities can dominate observed backscatter or brightness temperature (e.g. Marshall et al., 2004; Montpetit

et al., 2013). Improving understanding of these local scale interactions specific to distinct snow cover types is an important step towards the development of robust methods for microwave-based snow property retrieval.

Complex spatiotemporal scales of ground-observed variability are common to snow around the world (Deems et al., 2008; Jonas et al., 2009; Scipión et al., 2013), but tundra environments in particular present a challenging target of analysis with numerous environmental agents acting on shallow depositions (Derksen et al., 2009; Domine et al., 2012; Sturm and Wagner, 2010). In general, tundra environments north of the tree line are characterized by strong temperature gradients, exposure to high wind, and little precipitation input (Sturm et al., 1995). Under these conditions, tundra snowpack in open areas form with contrasting components of depth hoar and wind slab. Dry snow subjected to large temperature gradients will undergo metamorphosis, redistributing mass by processes of vapour transport and subsequent grain growth (Sturm and Benson, 1997). Basal layers in tundra environments are often dominated by this process, composed of dynamic recrystallizations of substantial diameter and preferential orientation. When sustained winds are present, subsequent deposition is quickly redistributed, forming crust and slab features. Over short distances, changes in wind and topography can produce lateral heterogeneity at scales up to 100 m (Sturm and Benson, 2004). Electromagnetically, these local variations in bulk and stratigraphic properties have the potential to generate diverse microwave responses from outwardly simplistic targets of similar bulk characteristics (e.g. depth, density, snow water equivalent).

A number of purpose-built systems for ground-based radar observation of snow and ice have been introduced in recent years to address questions regarding local scale interaction (e.g. King et al., 2013; Marshall et al., 2004; Morrison and Bennett, 2014; Willatt et al., 2010). These systems have been successfully deployed in support of large field campaigns,

including CLPX (Marshall et al., 2004), and under-flight testing of proposed satellite missions, such as CoReH$_2$O (Rott et al., 2010). Despite recent advancement in snow-radar observation, evaluation of tundra specific response remains incomplete. During the winter of 2010-2011, the Canadian Snow and Ice Experiment (CASIX) was initiated to collect coincident backscatter and snow property measurements in previously unevaluated sub-arctic environments near Churchill, Manitoba, Canada. The acquired field-observed dataset provides a unique opportunity to examine radar sensitivity to snow properties under conditions of potential uncertainty, including shallow depth and prevalent depth hoar.

In this study, we present two destructive sampling procedures to evaluate backscatter against *in-situ* snow properties for the purpose of quantifying and evaluating Ku-band (17.2 GHz) sensitivity in a unique terrestrial tundra environment. As a first case, traditional pit and bulk snow measurements are made within the field of view of an observing radar instrument at a spatially distributed set of snow covered open tundra targets. Summary and statistical analysis are used to identify and discuss potential drivers of backscatter variability and to quantify Ku-band sensitivity to selected snow properties, including snow water equivalent (SWE). A second case study presents an enhanced observation protocol using trench excavation data to characterize snow stratigraphy within the radar field of view. Observed lateral and horizontal heterogeneity of snow properties and stratigraphy are discussed in relation to coincident radar returns measured across the length of the trench. Two sites of contrasting snowpack composition are used to identify potential drivers of backscatter variability and discuss future direction for study.

6.2 Study area

Churchill, Manitoba, Canada (58.7692°N, 94.1692°W) is located on the south-west shore of Hudson Bay at the mouth of the Churchill River. Proximity to the arctic treeline divides the local environment into a number of distinct tundra-forest transition zones, each with characteristics typical of a larger domain within the circumpolar north (Kershaw and McCulloch, 2007). Accessibility of a number of distinct cryospheric environments over short distances made Churchill an ideal location to satisfy the diverse observational requirements of CASIX. Measurements collected as part of this study were made in an area to the east of Churchill, primarily composed of open areas (62%) with smaller portions occupied by forest (27%) and lake (11%) features (Derksen et al., 2012b). Large expanses of graminoid and shrub tundra were found throughout the study area with limited vegetation height, little topographic relief, and underlying organic soils common amongst them. The prevailing climate conditions in Churchill were best described as subarctic, where strong wind (6 m s^{-1}), low air temperature (-25°C), and limited snowfall (201 cm) were defining characteristics of the winter accumulation period (Environment Canada, 2013).

Backscatter measurements were made between November 15, 2010 and March 1, 2011 at a distributed set of snow covered open tundra sites along the Hudson Bay coast (Figure 6.1). In total, 28 independent observations were collected along with a suite of coincident snow property measurements to characterize physical processes and variability within the bounds of the observing instrument footprint. By standardizing these methods, a framework for evaluation of inter- and between-site backscatter was established. The mixed land cover environment local to Churchill provided access to a variety of tundra class snow conditions, limited in depth by wind exposure and lack of standing vegetation. To minimize environmental and observational complexities, sites were kept free of standing

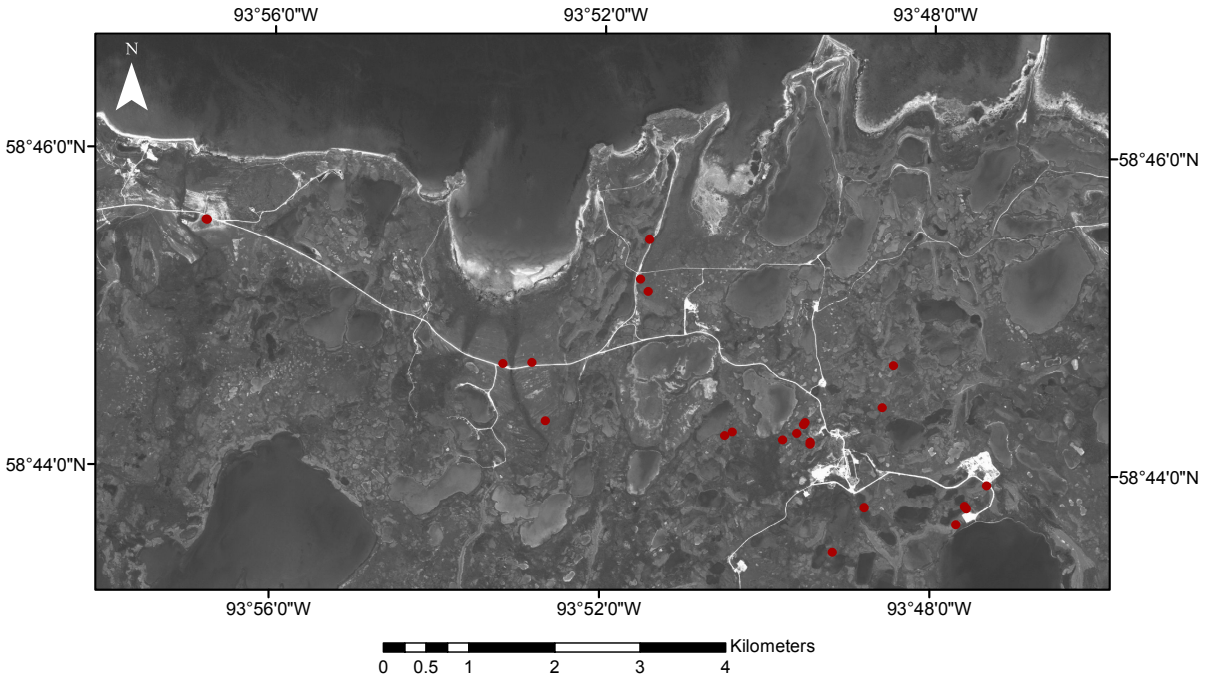

Figure 6.1: Churchill study area shown with measurement locations indicated in red.

vegetation and anthropogenic modifiers. As such, observations were primarily collected in graminoid-dominated environments where such complexities could be minimized. The following provides a brief overview of theory and methodology used to characterize the local dynamics of Ku-band radar interaction for the explicit purpose of evaluating sensitivity to tundra snow properties.

6.3 Data and methods

6.3.1 Background

Radar-based snow property retrieval exploits subtle changes in backscatter resulting from variations in accumulation and metamorphosis to derive snowpack information without physical contact. In terrestrial environments, a simple conceptualization of total backscatter (σ^t) can be made with snow and soil scattering contributions in a particular transmit and receive polarization combination (pq) (Rott et al., 2010; Ulaby et al., 1984):

$$\sigma^t_{pq} = \sigma^{as}_{pq} + \sigma^v_{pq} + \sigma^{gv}_{pq} + \sigma^g_{pq} \tag{6.1}$$

where the air-snow interface (σ^{as}), snow-ground interface (σ^g), snow volume (σ^v), and upper order interactions amongst the ground and snow volume (σ^{gv}) contribute to total backscatter (Figure 6.2). The magnitude of each contribution in equation (6.1) is determined by the local dielectric and physical state of the snow covered terrain and the parameters of the observing instrument. With parameters of the observing instrument held constant, seasonal changes in SWE can be expected to exert significant influence on backscatter because of its inherent relationship with both physical and dielectric properties of the snowpack.

Dielectric properties of target media are commonly described using the complex form of relative permittivity ε_r:

$$\varepsilon_r = \varepsilon' - i\varepsilon'' \tag{6.2}$$

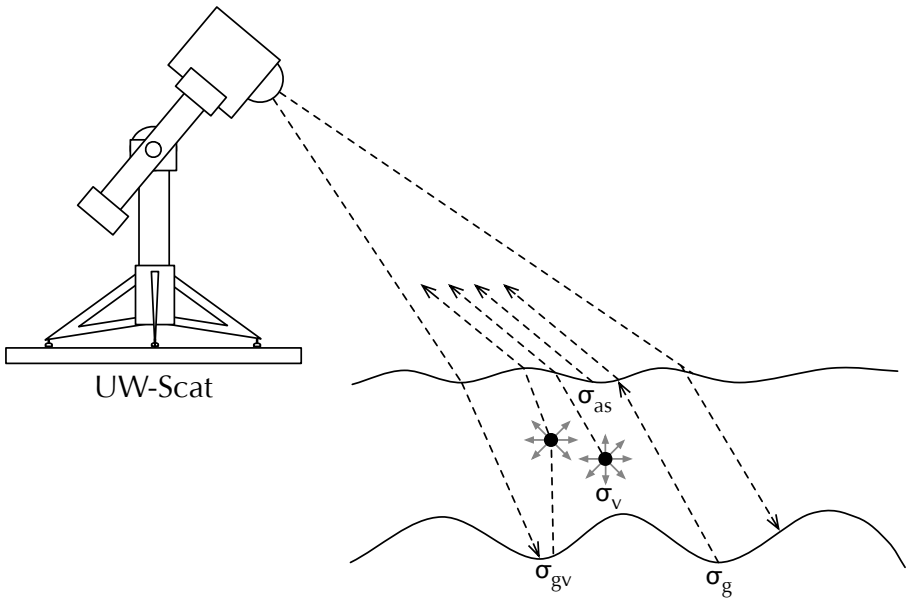

Figure 6.2: Setup of UW-Scat illustrating first-order backscatter elements for snow covered terrain. Diagram adapted from Rott et al. (2010).

where the real component $\varepsilon^{'}$ describes the ability of a material to polarize and store energy and, the imaginary component ε'' is a loss factor, describing dissipation of energy. For dry snow, values of complex permittivity are generally low at microwave frequencies ($\varepsilon' < 1.6$ and $\varepsilon'' < 10^{-3}$) resulting in negligible absorption of incident energy, dominant scattering losses, and significant potential for penetration. If the observed snow becomes wet, the presence of liquid water ($\varepsilon' \approx 80$) drastically reduces penetration depth and, therefore, the potential to retrieve volumetric snow properties at microwave frequencies.

Incident energy from a radar system directed towards a dry snowpack first interacts at the air-snow interface where it is divided into forward and backward scattering components. The magnitude of each component depends on the dielectric mismatch between the surface media and roughness at the interface. In the case of dry snow, a vast majority of incident energy propagates forward into the volume at angles greater than nadir because of the small

difference in permittivity between the media (Air $\approx 1 - i0$). As a result, σ_{as} is generally considered to be a minor contributor to dry snow backscatter and can be neglected.

Within the snow volume, variability in σ_v results from changes in physical properties including depth, density, grain size, and layering (Du et al., 2010; Fung, 1994). As a mixed media, snow consists of ice crystals in an air background, the combined effect of which facilitates volume scattering at microwave wavelengths. As depth increases, the path length of the propagating wave is extended, increasing the potential for scattering within the volume, and therefore increasing σ_v. Changes in snow density (ρ) contribute to σ_v through a functional relationship with permittivity where $\varepsilon' = 1 + 1.9\rho$ independent of frequency in the microwave spectrum (Hallikainen et al., 1986). According to this relationship, tundra snow conditions occupy a relatively small range of ε' between 1.19 and 1.70 (100 and 400 kg m^{-3}). Despite the limited range, variation in snow permittivity resulting from changes in density can contribute internal reflections and therefore influence σ_v. The influence of snow grain metamorphosis on scattering is dictated by a complex set of interactions controlled by size and shape (Du et al., 2010). In this case, seasonal processes of vapour transport and subsequent grain growth exert significant influence on volume scatter as the ratio between wavelength and grain size is increased. The complexity of the volume signal is exacerbated by seasonal processes of snow accumulation and transport which contribute intricate layering and thereby evolving vertical and horizontal heterogeneity of the reflections within the snowpack.

If incident microwave energy successfully traverses the snow volume it is again subjected to reflection at the ground surface because of the the dielectric mismatch in material properties. Unlike σ_{as}, a large σ_g contribution is common to terrestrial observations where local soil properties can exert influence on total backscatter. Soil moisture and state plays an important role in determining reflection from the underlying surface where a larger por-

tion of incident energy may be returned into the snow volume under early season saturated conditions. Spatially, variation in scattering results from differences in surface roughness. Energy reflected back into the snowpack may interact within the volume creating upper order scatter, contributing to σ_{gv}. Based on this basic set of interactions, a dynamic range of backscatter from terrestrial snow targets can be expected at Ku-band where seasonal and spatial snow processes can generate a diverse set of snow properties known to modify backscatter.

6.3.2 Backscatter measurement

To characterize backscatter response, a frequency modulated continuous wave radar system known as the University of Waterloo scatterometer (UW-Scat) was deployed (see King et al., 2013). Pulled by snow machine, the Ku-band unit of UW-Scat was transported in a sled based configuration to terrestrial locations and configured to collect backscatter measurements in less than 20 minutes. In the microwave remote sensing of snow, choice of frequency is often a compromise between penetration depth and sensitivity to desired snow properties. At Ku-band (12-18 GHz), the corresponding wavelengths are able to penetrate dry snow to depths in excess of 1 m (Marshall et al., 2004; Mätzler, 1987). For the purpose of observing tundra class snow, Ku-band was therefore sufficient to penetrate the expected range of depths (0.10 to 0.75 m; Sturm et al., 1995). Moreover, the proximity of the observing instrument wavelength to the process scale of individual snow grains was close enough to solicit a large volume response without saturating within the upper bounds of the snowpack. Backscatter measurements made with UW-Scat were collected at a centre frequency of 17.2 GHz across a narrow bandwidth of 0.5 GHz. The narrow bandwidth produced an operational range resolution of approximately 30 cm. From the sled mounted

position, the antenna and radio frequency hardware operated at a height of approximately 2.0 m with a narrow beamwidth of 4.3°. The resulting ground projected radar footprint was less than 30 cm in azimuth and range directions. Additional operational parameters of use during the experiment can be found in Table 6.1.

Table 6.1: UW-Scat operational parameters

System parameter	Operational value(s)
Height (m)	≈ 2.0
Transmit power (mW)	≈ 10
Centre frequency (GHz)	17.2
Bandwidth (GHz)	0.5
Range res. (m)	0.3
Beamwidth (°)	4.3
Incident angle (°)	30-45
Footprint at 30° (m)	0.15 x 0.17
Footprint at 45° (m)	0.20 x 0.28
Independent samples	> 16
Polarization	VV,VH,HV,HH

Once an observation site was selected, the scatterometer was levelled to the local terrain and radio frequency hardware allowed to stabilize in temperature to 35°C. A two-axis positioning system was then used to direct the radar antenna hardware through a series of azimuth sweeps to collect measurements at elevation angles between 30° and 45° in 3° increments. Measurements at each elevation angle were integrated over a 60° azimuth sweep to improve the number of independent samples and ensure an adequate signal to noise ratio. In post-processing, the backscattering coefficient, *sigma nought* (σ^0), was estimated to express the ratio of power reflected to power transmitted as normalized to the ground projected radar footprint. Copolarized vertical (σ^0_{vv}), horizontal (σ^0_{hh}) and cross-polarized (σ^0_{vh}) backscatter coefficients were derived based on the averaged range profiles

and system geometry. Detailed discussion of signal processing procedures can be found in Geldsetzer et al. (2007) and King et al. (2013).

To calibrate the scatterometer system, an accompaniment of internal and external procedures were used. Prior to each site scan, a trihedral corner reflector was erected in the field of view and observed to collect a short time series of measurements. Differences between the observed polarimetric measurements and reference target backscatter were corrected offline using a procedure described in Geldsetzer et al. (2007). To characterize system and platform noise, open sky measurements were collected after each corner reflector measurement. Sky measurements were coherently subtracted from target range profiles to reduce the influence of system noise and isolate the desired target signal. Estimates of worst case measurement error from the post-processing procedure were on average $\pm$ 2.0 dB including a 0.5 dB addition for random error. In general, the observed errors were a function of the limited number of independent samples collected under the beam limited conditions of the sled based configuration. Estimates of total error also included bias introduced by human and environmental inaccuracies introduced with mis-estimation of the deployed sensor height and wind buffing of the reference target.

6.3.3 Snow measurements

Destructive sampling within the scatterometer field of view was completed immediately after each scan to gather information about local snow properties and to evaluate snow variability at the sub-scan level. A standard procedure was used where horizontal heterogeneity in depth, density, and SWE was quantified in addition to point measurements of vertical snow properties. On completion of the scatterometer measurement, a 15 m x 20 m box was measured within the field of view of the scatterometer to bound a snow sampling

area (Figure 6.3). Within the sampling area, a grid of snow depth measurements were collected using a GPS enabled Snow-Hydro MagnaProbe. Each grid collected a minimum of 200 measurements spaced across several transects parallel to the scatterometer range direction. Pairs of ESC-30 snow core measurements were also collected at six locations within the sampling area to estimate bulk density and SWE. Using a hand-held spring scale, the weight of each snow core was recorded along with the depth at the measurement site.

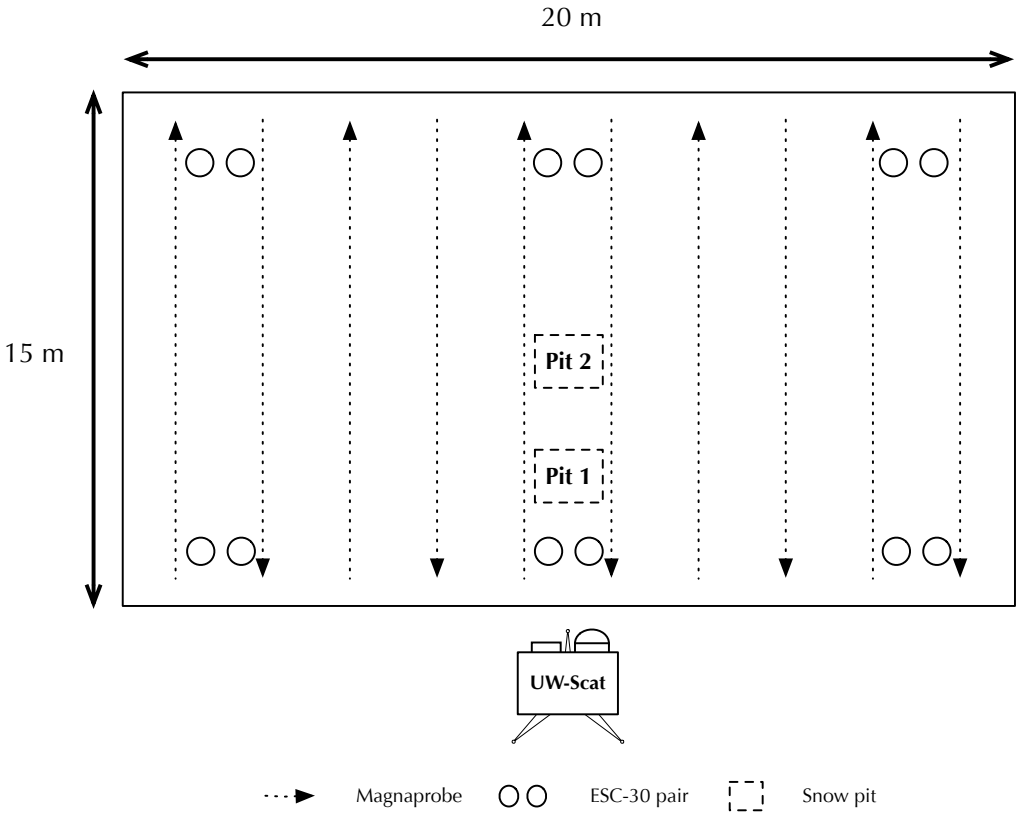

Figure 6.3: Destructive snow sampling protocol plan view. At each site a distributed set of bulk and stratigraphic measurements were made to quantify variability within the scatterometer field of view.

In addition to bulk snow measurements, two snow pits were excavated at 3 m and 5 m outwards from the scatterometer. Multiple pits were completed to avoid mischaracterization related to pit placement and large variations in topography (e.g. hollows between hummocks). Once excavated, structural and textural discontinuities were used to define and record layer locations, thickness, and general composition. A snow sample from each layer was extracted and placed on a grid comparator card for visual analysis. Using a stereomicroscope, grain origin types were identified and estimates of axial length were recorded. Density within each snow pit was measured along two continuous vertical profiles extracted from the pit face using a 100 cm^3 wedge style cutter and digital scale. Temperature profiles were constructed using a string of thermistors inserted into the snowpack with a vertical spacing interval of 4 cm.

6.3.4 Trench measurements

To evaluate the influence of lateral heterogeneity on backscatter, detailed measurements of snowpack stratigraphy were excavated within the scatterometer field of view. Following a protocol detailed in Tape et al. (2010), 5 m trenches were dug approximately 3 m outwards from the scatterometer across the azimuth look direction to correspond with scatterometer measurements collected at elevations between 30° and 45°. The excavated face was prepared manually with hand tools to create a flat surface perpendicular to the ground. Once prepared, 850 nm centre frequency near-infrared (NIR) photography was completed along the length of the trench using a linear rail system to maintain constant distance to the trench face. Sequential photographs taken along the length of the trench were georeferenced using an in-scene centimetre scale Crane measuring staff positioned horizontally above the trench face. A single continuous image was stitched together from the collected

set of photographs and stratigraphy was manually extracted using visual interpretation at a 1 cm horizontal resolution (Figure 6.4). In addition to NIR photography, inter-layer snow properties were characterized with a set of 5 snow pits completed at 1 m intervals along the trench. Transects of density, temperature, and grain size were measured using standard snow pit protocol.

Figure 6.4: A series of 850 nm NIR photographs taken along the length of an excavated 5 m snow trench. Photographs were referenced and stitched together for analysis. Black lines show manually identified snow stratigraphy.

6.4 Results

6.4.1 Seasonal and spatial snow properties

Accumulation within the Churchill study area evolved with spatiotemporal complexity related to variations in vegetation, topography, and climate. Given the selected land cover composition of flat open terrain and dominant graminoid vegetation, observation sites were exposed to a common set of sub-arctic environmental agents including strong wind and sustained low air temperature. The majority of accumulation within the study area was deposited between December and January with a limited number of precipitation events

occurring thereafter. In the observed open areas, snowpack development was heavily influenced by sustained winds, where average speeds exceeded 5 m s^{-1}, which rapidly redistributed accumulated snow. Mean snow depth in the observed tundra sites was shallow, ranging from approximately 4.0 to 25.0 cm, generally increasing through the season (Table 6.2). Examples that deviated from this range were associated with changing land cover characteristics found in close proximity to the observation site (e.g. forest transition zones situated near sites 12 and 13). Inter-site standard deviation of snow depth ranged between 20% and 59% of the mean, in most cases declining with increasing depth (R = -0.5, n = 26)[1]. At the open tundra sites, micro-topographic elements, including hollows between hummocks, trapped early season snow and created deviations by up to double the inter-site mean. The influence of these features on total depth was reduced as accumulation increased relative to variations in surface height, effectively masking the smaller ground features. Despite the sustained influence of wind, bulk snow density remained low (< 250 kg m^{-3}) and did not vary substantially through the season. In comparison to depth, inter-site variability of density was minimal with standard deviations accounting for less than 20% of the observed mean. As a product of depth and density, the observed range of SWE was seasonally and spatially small, reaching a maximum of 70.0 mm near the end of the experiment. At the tundra observation sites, variation in SWE showed a strong linear relationship with depth as a result of the narrow range of bulk density encountered (R^2 = 0.98).

Snow stratigraphy excavated within the scatterometer field of view increased in complexity from an early point in the experiment. Sequential periods of accumulation and wind transport created between 2 to 7 distinct horizontal layers of varied thickness and texture. A basal depth hoar layer was the most consistent feature excavated amongst the

[1]All presented correlations and coefficients of determination were significant at the 0.05 level.

Table 6.2: Average inter-site snow properties measured at each of the tundra observation sites. Dates of observation are presented as day of year (DOY) spanning the 2010-2011 observation period. ESC-30 measurements were not available on DOY 60.

		Depth (cm)		Density (kg m^{-3})		SWE (mm)
Site	DOY	Mean	SD	Mean	SD	Mean
1	310	5.7	2.9	104	10	5.9
2	319	5.0	2.9	139	40	6.9
3	320	5.3	1.8	129	51	6.9
4	320	3.9	1.0	154	54	6.0
5	322	3.5	1.3	139	40	4.8
6	324	4.0	1.5	155	71	6.3
7	328	6.2	2.7	258	70	15.9
8	328	6.9	2.8	262	41	18.1
9	329	3.9	1.4	112	26	4.3
10	329	4.1	1.4	130	31	5.3
11	334	8.1	1.9	206	41	16.7
12	337	11.6	3.7	288	91	33.3
13	337	10.9	4.6	211	32	22.9
14	346	23.2	6.7	302	40	70.0
15	346	24.1	6.6	207	29	49.9
16	352	14.0	3.6	186	22	26.0
17	4	16.2	4.3	253	30	41.0
18	16	20.5	5.2	163	41	33.3
19	17	14.0	3.6	219	33	30.8
20	24	16.9	4.6	264	43	44.6
21	33	19.0	6.0	248	42	47.0
22	44	16.8	6.0	280	34	46.9
23	49	19.2	7.2	233	36	44.6
24	50	21.9	6.0	216	34	47.2
25	56	15.2	4.3	209	29	31.8
26	60	25.0	5.0	—	—	—

open tundra sites. In the 50 pits completed, depth hoar comprised on average 52% of total depth. The rapid development of the basal hoar layer was driven by a sharp early season decline in air temperature sustained through the end of the experiment with limited increases in depth. Vertical temperature gradients measured through the shallow snowpack exceeded 20°C m^{-1} in 40 of 50 open tundra pits, a strong indicator of sustained kinetic growth. By the end of the observation period, mean grain size within the depth hoar layer had exceeded 3 mm in diameter with poly-aggregates reaching 6 mm or larger. Thickness of the basal depth hoar layer was heavily influenced by inter-site changes in ground surface height. As a result, the thickness of the basal hoar layer between inter-site snow pits was found to vary by up to 10 cm where periodic hummock features were present.

Contrasting surface features were heavily influenced by wind transport, featuring numerous slab layers separated by hard thin crusts. Grain sizes within surface slab layers were generally small ($<$ 1 mm) due to persistent wind action and subsequent rounding of grains with transport. A vertical gradient of grain size through the snowpack became apparent in the latter part of the experiment where wind rounded grains transitioned into faceted grains with sustained temperature gradient metamorphosis. In several of the late season snow pits, large faceted grains could be found intermixed all the way to the surface of the snowpack. Few ice features were identified with those found being very thin snow-ice layers situated at the base of the pack from early season melt processes. Rapid redistribution of snow accumulation limited the number of fresh snow observations collected during the experiment; in most cases, surface layers identified with fresh snow were generally thin and intermixed with wind rounded grains.

Overall, the rapid and often subtle changes within the shallow tundra snowpack provided a challenging target of analysis and a unique opportunity to evaluate distinctive features previously unaddressed at Ku-band. The predominant local processes of wind

redistribution and temperature gradient metamorphism were characteristic of conditions previously described along the Hudson Bay coast and of the generalized conditions present with tundra type snow (Kershaw and McCulloch, 2007; King et al., 2013; Sturm et al., 1995). Electromagnetically, the observed snowpack structure and basal hoar layer had the potential to create large increases in backscatter as seasonal and spatial processes of metamorphosis progressed.

6.4.2 Comparison of backscatter and snow property measurements

To evaluate spatiotemporal backscatter sensitivity, snow property measurements collected at each site were compared against coincident estimates of integrated σ^0. In an effort to reduce the influence of sub-scan variations in micro-topography, estimates of σ^0 were averaged across a small range of incident angles between 30° and 45°. In the averaged scatterometer observations, a large dynamic range of σ^0 was found to be more than 8 dB. Copolarized σ^0_{vv} and σ^0_{hh} ranged in magnitude from approximately -13 to -5 dB while cross-polarized σ^0_{vh} and σ^0_{hv} responses were measured across a narrower range between -26 and -15 dB. For the entirety of the experiment period, cross-polarized σ^0_{vh} and σ^0_{hv} were found to be in agreement of less than 0.1 dB and therefore were considered reciprocal for the purpose of analysis. The large dynamic range of backscatter in each polarization channel suggested sensitivity to the evolving physical and dielectric properties warranting discussion of the involved interaction space.

The observed relationships between depth, SWE, and σ^0, as shown in Figure 6.5, indicate Ku-band sensitivity to evolving snow properties at the 26 open tundra sites. Across the small range of encountered mean depth, a clear linear relationship with σ^0_{vv} emerged

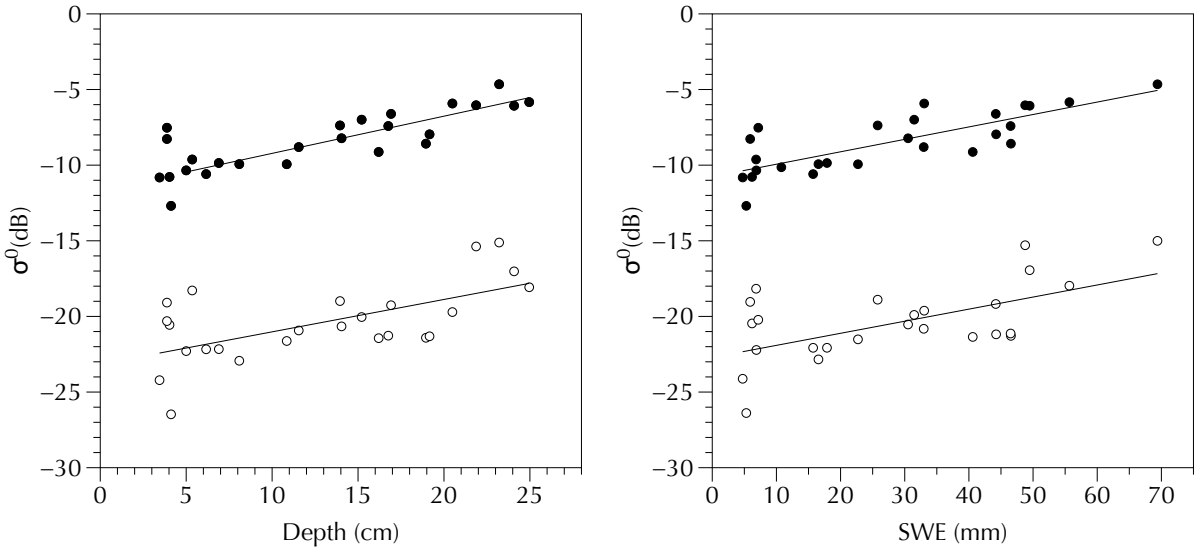

Figure 6.5: Comparison of average σ^0 against snow depth (Left) and SWE (Right) at the open tundra observation sites. Solid circles show σ^0_{vv} response and hollow circles show σ^0_{vh} response. Measured σ^0_{hh} and σ^0_{hv} responses not shown improve readability. Fit lines are linear.

where vertically polarized backscatter increased by approximately 0.22 dB for every 1-cm increase in depth ($R^2 = 0.67$). A less sensitive σ^0_{hh} response, not shown in Figure 6.5, increased by 0.17 dB for every 1-cm in depth ($R^2 = 0.44$). Preferential vertical scattering was apparent throughout the experiment in which only 8 of 26 observations demonstrated a positive copolarization ratio ($\sigma^0_{hh}/\ \sigma^0_{vv}$). The cross-polarized σ^0_{vh} response was comparable in slope to the copolarized channels, increasing by approximately 0.17 dB for every 1-cm increase in depth ($R^2 = 0.39$). Unsurprisingly, the observed cross-polarized sensitivity to depth σ^0_{vh} was strongly correlated with increases in copolarization response at the same site.

As a whole, the observed increase in Ku-band backscatter response agrees with theory in which increasing path length generates additional first and upper order interactions within

the snow volume. The copolarized linear fits applied in Figure 6.5 produce root mean squared errors (RMSE) of 4.1 and 5.6 cm for σ^0_{vv} and σ^0_{vh} respectively. This result was encouraging as it demonstrated a strong potential to retrieve snow depth with sensitivity to small changes in the local tundra environment. Uncertainties in the potential retrieval of depth appears to be greatest with accumulation less than 5 cm where a large dynamic range of σ^0 was observed. Under these very shallow conditions, co- and cross-polarized interactions were dominated by the response of the underlying soil rather than the snow volume. Analysis of variability of the shallow outliers was complicated by the seasonality of the measurements where all observations less than 5 cm were collected in shoulder season conditions where large differences in local soil moisture were likely influential. Without detailed inter-site measurements of soil properties it was not possible to evaluate differences found between the early season Ku-band observations and the full range of response. In spite of the large residuals observed under extremely shallow conditions, measured co- and cross- polarization backscatter demonstrated a coherent response with increased depth and potential for the retrieval under shallow tundra conditions.

Similar to snow depth, SWE accumulation in the open tundra environment was limited by persistent wind action and negligible precipitation input. Given that inter-site variations in SWE were found to be strongly related to depth, a response similar to the above result was expected between SWE and σ^0. Figure 6.5 shows the strong Ku-band σ^0 response identified with increasing SWE at the open tundra sites. Sensitivity to SWE was the strongest with σ^0_{vv}, increasing by 0.82 dB for every 1 cm in SWE ($R^2 = 0.62$). Similar to the observed relationship with depth, σ^0_{hh} showed weak sensitivity to SWE at 0.62 dB for every 1 cm increase ($R^2 = 0.42$). Finally, the cross-polarized σ^0_{vh} sensitivity was observed at 0.80 dB for every 1 cm increase in SWE ($R^2 = 0.36$). The observed increase in σ^0 was large relative to the small range of observed SWE. Again, this result was encouraging for

the retrieval of tundra snow properties where strong sensitivity across a small range of SWE demonstrated potential to resolve subtle changes in snow mass.

In the observed relationship between SWE and σ^0, backscatter variability separated sites of similar aggregate composition in some instances by several decibels. Seasonality and metamorphic state of the observed snowpack appeared to play a role in the backscatter diversity where increase in grain size was strongly correlated with increased copolarized backscatter response (R = 0.61). While this finding was of interest, the seasonality of the measurements and as a result, covariance of depth and grain growth, made it difficult to decompose causation between the evolving snow properties. Moreover, the previously demonstrated spatial variability in stratigraphy made it extremely difficult to interpolate the inter-site snow pits in the context of the larger scatterometer field of view. Overall, the distributed measurement protocol was able to show desirable Ku-band sensitivity to bulk snow properties, but did not provide the means to resolve the role of stratigraphy or grain size in observed backscatter diversity.

6.4.3 Evaluation of trench backscatter response

Direct comparison of *in situ* sampled snow properties and σ^0 revealed Ku-band sensitivity to increasing snow volume. Despite the positive result, snow pits completed within the scatterometer field of view yielded insufficient information to evaluate the influence of sub-scan lateral heterogeneity on observed backscatter. To address this open question, two 5 m trench experiments were completed on January 7 and 8 to characterize variation in stratigraphy within the scatterometer field of view. Collocated radar returns measured across the azimuth range of the scatterometer were compared with excavated snow stratigraphy to evaluate potential sub-scan influences on backscatter. The first trench was excavated

in an open area adjacent to a transition zone, hereafter referred to as the forest edge site. The forest edge site possessed snow features common to the previous open tundra sites including limited depth, predominant wind slab-depth hoar composition, and a rough underlying ground surface. The second trench was completed within a sparsely populated tree stand where the sheltered snowpack was composed of a larger number of lower density layers. Comparison of the two targets provided an opportunity to evaluate a range of snow conditions and their influence on backscatter at scales local to the observing instrument.

A complex arrangement of internal layers with several discontinuous features was observed at the forest edge site (Figure 6.6; top panel). Within the shallow snowpack, 3 to 5 distinct layers were found at any given horizontal position and, in total, 6 unique layers were identified. Total snow depth along the trench varied between 16.4 and 37.2 cm with a standard deviation of 5.6 cm (Figure 6.6; middle panel). The observed variation in depth was in agreement with inter-site measurements completed at the previous open tundra sites where large changes in total depth were encountered over short distances. The most prominent change in snowpack composition was associated with a protruding hummock feature centred at the mid-point along the trench. Prior to excavation, the smooth surface of the mid-season snowpack provided no indication of the heavy influence of this feature on both total depth and stratigraphy.

Internal stratigraphy of the forest edge snowpack consisted of several wind influenced features underlain with a continuous layer of depth hoar (Table 6.3). A number of thin wind crusts (< 0.5 cm), harder in texture than the surrounding snow, separated the larger internal layers of the snowpack. The upper and most recent feature, noted as layer 6 in Figure 6.6, was a smooth continuous surface layer composed of small wind rounded grains intermixed with decomposing needle-like precipitation (0.1 to 0.4 mm). Beneath layer 6, a set of thin soft slabs, noted as layers 4 and 5, surrounded the apex of the prominent

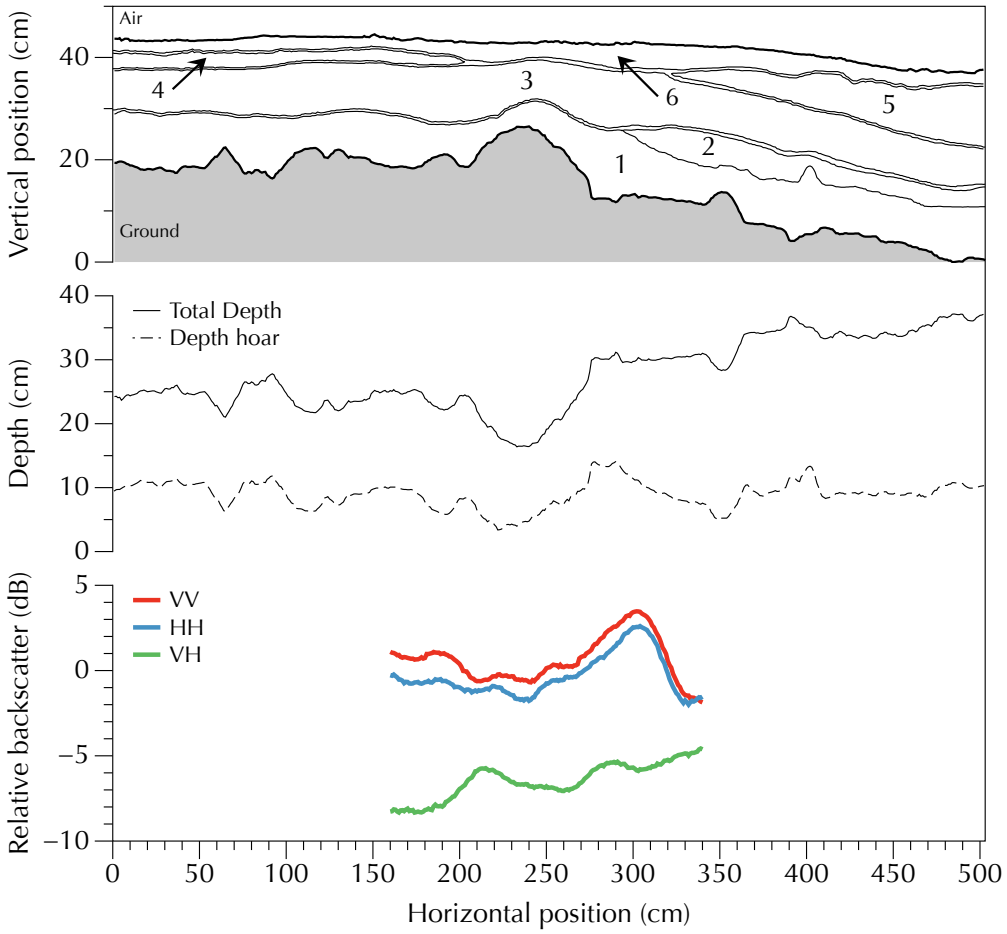

Figure 6.6: Stratigraphy (top), depth (middle), and relative backscatter (bottom) observed along the length of the forest edge trench. Layer notation in the top panel corresponds with description in Table 6.3.

hummock feature where wind scouring had created a notable horizontal discontinuity. Each slab was composed of slightly larger wind rounded grains (0.4 to 1.0 mm) and were similar in density to the surface slab layer (220 kg m^{-3}). The largest continuous feature identified within the trench was a mixed type layer composed primarily of faceted grains identified as layer 3. Within this large continuous layer, a wide range of grain sizes were found

between 0.2 and 1.5 mm. On the right hand side of the trench, a hard relict wind slab was identified as layer 2 (between 300 and 500 cm) in which densities were the greatest within the snowpack, increasing to approximately 280 kg m^{-3}. The basal surface of layer 5 was composed of high density indurated hoar with well developed cup structures exceeding 1 mm in diameter. Finally, the basal depth hoar layer, noted as layer 1, contained striated cup shaped grains and large poly-aggregates ranging in diameter from 1 to 4 mm. As a fraction of total depth, the depth hoar layer composed on average 33% or 9.0 cm of the snowpack (Figure 6.7; middle panel). The thickness of the basal layer was controlled by the ground surface height and location of the buried hard slab.

Table 6.3: Description of stratigraphy excavated at the forest edge site. Layer numbers correspond with Figure 6.6.

Layer	Description
6	Recent mixed layer with wind rounded grains and decomposing needles
5	Mixed soft slab layer composed of mostly wind rounded grains
4	Mixed soft slab layer composed of mostly wind rounded grains
3	Mixed soft slab layer with wind rounded and faceted grains
2	Buried hard slab. Mixed composition of indurated hoar.
1	Depth hoar. Large faceted cups and poly-aggregate structures.

The excavated trench revealed an interesting target for radar observation where large changes in snowpack properties were found over short distances. Radar measurements collected as part of the forest edge scan were processed as individual returns relative to response of the collocated corner reflector and given approximate horizontal positions in relation to the trench face (Figure 6.6; bottom panel). As a general limitation of the observation protocol, uncertainty in the estimated horizontal radar position was greatest near the edges of the scan due to the arc of ground projected scatterometer sweep. The measured copolarization response across the trench showed variability in relation to changing snow

and soil conditions. In particular, variability was noted in relation to the previously identified hummock feature where copolarized vertical backscatter decreased by 16% relative to the deeper accumulation situated at horizontal positions to the left of the feature. The horizontal backscatter response to the large change in snow depth was muted in comparison, emulating previously observed behaviour of the negative copolarization ratio observed in the distributed set of tundra snow targets. Across the width of the trench, copolarized horizontal response was found to be approximately 12% lower then the vertical response. To the right of the hummock, backscatter increased reaching a trench maximum near the horizontal position of 300 cm. The rapid increase in copolarized backscatter coincided with increasing snow depth and complexity in layering. In particular, layer 5 was a unique dielectric and geometric discontinuity where the indurated depth hoar was both of higher density and larger grain size in comparison to the surrounding layers. Coupled with the increased depth to the right of the hummock, there was potential for multiple-scattering which appeared to be supported by the increased depolarization. Overall, the forest edge trench demonstrated the presence of dynamic changes in snowpack structure over short distances which appear to have had a large influence on backscattered energy.

The second trench was completed within a sparsely populated tree stand, sheltered from strong local winds. Total depth along the trench ranged from 30.0 to 51.6 cm, with a smaller standard deviation of 3.1 cm. The contrasting influence of the local environmental agents was evident in the excavated stratigraphy (Figure 6.7). Here, layers were comparatively homogeneous, greater in number and, in most cases, found continuously through the 5 m trench. In total, 9 unique layers were identified with 5 present across the entire trench (Table 6.4). As in the previous excavation, a number of thin crusts ($<$ 1mm) were found separating the major internal layers. Fresh precipitation, identified as layer 9, was the most recent layer and was composed of a combination of large stellar plates (1 mm) and much

smaller graupel (0.1 mm). Below the fresh snow surface, a decomposing precipitation layer was found with smaller round grains (Layer 8). Lacking influence from local wind, the two most recent layers were very low in density ranging from approximately 100 to 150 kg m^{-3}. The remaining layers of the snowpack were heavily influenced by temperature gradient metamorphosis with grain size increasing towards the base of the snowpack. Layer 7, the more recent of two mixed type layers, was composed of smaller rounded grains with some larger faceted grains (0.3 to 1.0 mm). A similar mix of grain types was found in layer 6 with a bias towards larger faceted grains (0.6 to 1.8 mm). Density increased within the more mixed layers reaching a maximum of 270 kg m^{-3}. Again, basal depth hoar features dominated the remainder of the snowpack with layers 4 and 5 composed to large cup shaped grain up to 4 mm in diameter. Density within the unconsolidated depth hoar layers was lower at approximately 170 kg m^{-3}. A number of discontinuous icy hoar features, identified as layers 1, 2, and 3 were found at the base of the pack. These thin features were very hard in texture and were composed of large gains up to 4 mm in diameter.

Table 6.4: Description of stratigraphy excavated at the spruce forest trench site. Layer numbers correspond with those shown in Fig 6.7.

Layer	Description
9	Fresh snow. Stellar plates and graupel present.
8	Recent snow. Decomposing precipitation and clusters of rounded grains.
7	Mixed layer. Primarily composed of small rounded grains with some faceted grains present
6	Mixed layer. Primarily composed of larger loose faceted grains with some round grains.
5	Unconsolidated depth hoar. Mix of cups and less developed forms.
4	Unconsolidated depth hoar. Large cup shaped grains.
3	Consolidated depth hoar. Hard texture.
2	Icy layer. High density hard snow feature.
1	Icy layer. High density extremely hard snow feature.

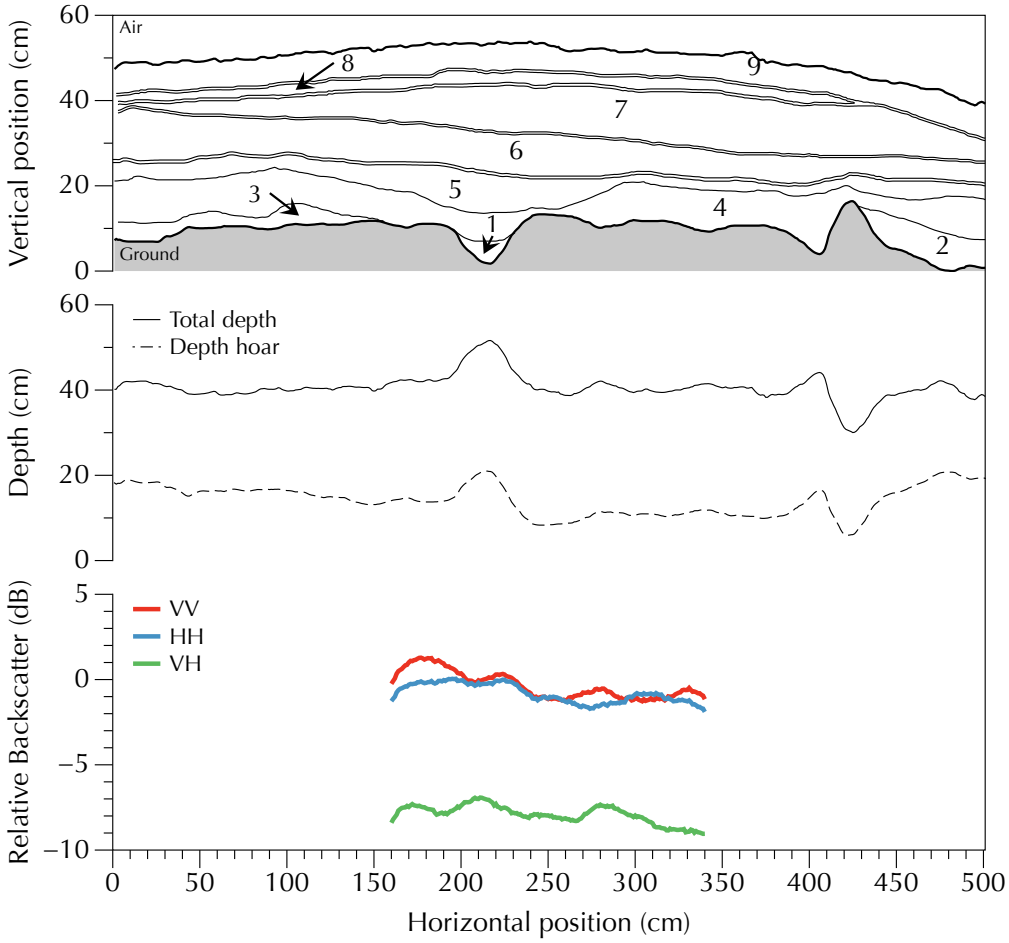

Figure 6.7: Stratigraphy (top), depth (middle), and relative backscatter (bottom) observed along the length of the forest trench. Layer notation in the top panel corresponds with description in Table 6.7.

In comparison to the forest edge trench, the backscatter response from the forest trench was stable across the scan. The reduced variability in the co- and cross-polarized backscatter corresponded well with reduced variation in snow depth and increased homogeneity of the internal stratigraphy relative to the previous trench. In clear contrast to the forest edge site, there was no observed preference in orientation of the copolarized backscatter. This

observation separates the forest response from the open tundra sites where vertical preferential scattering was consistently observed. Across the full length of the trench, a decline was identified in both the co- and cross-polarization response. This observed variation in backscatter was small in comparison to the previous trench, but did indicate a changing interaction with the physical and/or dielectric properties of the sub-scan target. The most evident change in snowpack composition along the trench that could have produced an attributable change in backscatter was the increasing thickness of layer 7 and corresponding reduction of layer 6. These two mixed layers types were composed of different grain sizes, where those within the more recent layer 7 were smaller in diameter by a substantial margin. From left to right, layer 7 gradually became the dominant layer of the snowpack effectively reducing the mean grain size of the snowpack. Unfortunately, the coarse range resolution of UW-Scat did not allow for characterization of individual layers contributions, and therefore, did not offer definitive evidence of why the change had occurred.

In general, the contrasting backscatter responses of the two trench sites provided practical examples of the influence of sub-scan snow properties on Ku-band backscatter. The findings suggest that variability in tundra snow properties over short distances are significant modifiers of Ku-band backscatter and, in the future, should be considered in the development of tundra snow property retrievals.

6.5 Discussion and conclusion

During CASIX, a distributed set of 26 backscatter measurements were collected across a range of tundra snow conditions influenced by spatiotemporal processes of accumulation and metamorphosis. A standardized sampling protocol was introduced to measure snow properties within the scatterometer field of view immediately after each scan to evaluate

local influences on backscatter. Predominant agents of wind transport and temperature gradient metamorphosis governed the spatiotemporal development of the observed snowpack at the selected open tundra sites. Sustained exposure to strong winds quickly redistributed accumulation and limited total depth to less than 30 cm. Inter-site variations in snow depth were often large as a result of changes in underlying ground surface height that varied over short distances. Given the anticipated sensitivity of Ku-band to changing snow conditions, the inter-site variations in depth had the potential to drive variability in sub-scan measurements. In addition to wind action, steep vertical temperature gradients were common to the open tundra sites which enabled periods of substantial grain growth. A thick basal depth hoar layer was found throughout the experiment with large cup shaped grains in excess of 4 mm. By the end of the observation period, faceted grains were found throughout the full volume of the snowpack. Electromagnetically, the rapid spatiotemporal development of large grains had potential to enhance backscatter response as a result of increased multiple-scattering (Du et al., 2010). Overall, the characterized snow conditions provided a unique opportunity to evaluate Ku-band interactions with a distributed set of snow covered targets not previously addressed in literature.

Despite the limited snow accumulation, a large dynamic range of co- and cross-polarized σ^0 was observed at the open tundra observation sites. Analysis of the spatiotemporal response indicated Ku-band backscatter sensitivity to increasing snow depth and SWE. Strong backscatter sensitivity identified across the small range of observed depth was significant as it demonstrated promise for retrieval of subtle changes in snow properties typical of environments with tundra type snow. Across the observed range of depth, σ^0_{vv} was found to have the greatest sensitivity and strongest coefficient of determination. Copolarized σ^0_{hh} and cross-polarized σ^0_{vh} were similar in slope, but with a lower coefficient of determinations. Modelled response shown in Xu et al. (2012) agrees with the strong Ku-band (17.2 GHz)

increase where signal saturation was noted at depth as shallow as 60 cm. Moreover, previous wideband study at Ku-band (14 to 18 GHz) by Marshall et al. (2004) identified strong reflections from depth hoar which may account for the enhanced tundra snow backscatter response.

While the distributed open tundra scatterometer observations showed sensitivity to evolving snow properties, inter-site measurements were insufficient to characterize the influence of sub-scan variations in snow properties. With demonstrated variability in depth and stratigraphy over short distances, a refined methodology for detailed characterization of snow stratigraphy within the field of view was implemented. Two detailed trench experiments completed in contrasting environments exemplified the highly variable nature of tundra snow despite its shallow accumulation. The influence of variability in snow properties was apparent in the backscatter signal at the forest edge site where deviations of depth and stratigraphy created strong deviations in signal. Conversely, the relative homogeneity of the forest trench site responded with reduced variability in backscatter. In the future, snow property information extracted from trench experiments will be of use to initialize electromagnetic models and for diagnostic analysis where sensitivity of high resolution snow properties can be evaluated over the entire trench. Such studies will be particularly useful for clarifying the role of grain size where subtle changes in layer structure have appeared to influence backscatter.

This study presented a novel set of field-based experiments to evaluate the influence of spatiotemporal changes in snow properties on Ku-band backscatter. In doing so, a previously untested tundra environment has been characterized providing a starting point for the development of robust retrieval methods. The findings of this study supports the use of Ku-band backscatter measurements for observation of snow properties in tundra environments. Future study will be needed to assess the implications of the demonstrated

backscatter variability with snow accumulation and its influence on scaling to airborne and satellite based observation approaches.

6.6 Acknowledgement

CASIX field activities were supported by the European Space Agency, Environment Canada, and Natural Sciences and Engineering Research Council of Canada. The authors would like to thank Arvids Silis, Cristina Surdu, Dave Halpin, Homa Kheyrollahpour, Jason Oldham, Mel Sandells, Nic Svacina, Niina Luus, Peter Toose, Ryan Ahola, and Steve Howell for their contributions to the field campaign. Logistical support for CASIX was provided by the Churchill Northern Studies Centre. The University of Waterloo scatterometer system was developed with support from the Canadian Foundation for Innovation and the Ontario Ministry of Research and Innovation. The work of Joshua King, Richard Kelly, Grant Gunn, and Claude Duguay was supported by the Natural Sciences and Engineering Research Council of Canada.

Chapter 7

General conclusions

7.1 Summary of work

The overall aim of this thesis was to advance knowledge of snow-radar interactions specific to tundra environments. For the first time, a set of field-based experiments was used to demonstrate the considerable potential of 17.2 and 9.6 GHz radar for observation of tundra snow properties. The limited coverage of ground-based snow accumulation measurement networks and challenges involved with current satellite-based approaches have made development of novel tools for snow observation, such as those presented in this thesis, of great importance to a diverse set of research communities. Ability to evaluate changing snow extent, mass, and energy at the scales of ground observed variation is critical to advancing our understanding of the role of snow in global climate processes, regional hydrology, and vulnerable ecosystems. Field observations and analysis of radar sensitivity to snow property presented as part of this thesis represent substantial advancements to our understanding of snow-microwave interaction and contribute novel spatiotemporal knowl-

edge specific to tundra environments. Advancements made in this thesis are valuable to the development of electromagnetic models and provide quantitative observations for the validation of retrieval algorithms. As a complementary approach to current snow remote sensing methods, radar observations have been demonstrated as a viable means to retrieve snow accumulation information for shallow tundra snow without the need for physical sampling or intervention.

Introductory chapters of this thesis presented background information regarding the development of seasonal snow in terrestrial environments and fundamental principles of radar interaction. In chapter 4, a novel platform for dual-frequency (17.2 and 9.6 GHz) microwave observation of terrestrial snow was introduced to evaluate processes described in the introductory chapters. Using two case studies, preliminary findings and observations from previously untested tundra and wetland environments near Churchill, Manitoba, Canada were evaluated. In the first case, a methodology for repeat observation of snow cover in a wetland environment was presented to relate seasonal variation in backscatter to evolving snow properties in a natural setting. The experiment demonstrated dual-frequency sensitivity to increasing depth and SWE at the wetland site. Of importance was the identification of a frequency-dependent backscatter response where Ku-band sensitivity to SWE was found to change beyond 81 mm due to potential saturation of the signal. Conversely, the longer wavelength X-band measurements increased in sensitivity as the target snow cover approached the maximum observed SWE of 120 mm. This finding suggested that frequency dependent sensitivity across the microwave spectrum could be leveraged to observe snow properties over a large range of conditions by using a dual-frequency approach. To separate and evaluate backscatter originating within the snow volume, an additional experiment was presented where snow was removed from the scatterometer field of view after an initial snow covered observation. Once the shallow 15 cm snow cover was removed, a

significant reduction in co- and cross-polarized Ku-band backscatter was observed from the bare ground. At X-band, a similar reduction in backscatter was not observed, indicating insensitivity to the shallow snowpack at the longer observing wavelength. These findings are significant as they identity substantial Ku-band sensitivity which could be used to retrieve snow properties under shallow snow conditions typical of tundra environments.

Extending the proof-of-concept approach introduced in chapter 4, an enhanced experiment for coincident seasonal observation of backscatter and snow properties was presented in chapter 5. Between November 2010 and March 2011, a total of 13 scatterometer observations were collected from a single snow covered target east of Churchill, Manitoba, Canada. To maintain an undisturbed target for seasonal scatterometer measurements, an area adjacent to the field of view was used to characterize the evolving snow conditions. Snow pit and transect sampling methodologies were used to evaluate seasonal processes of accumulation and metamorphosis at point and local scales. Seasonal evolution of the local snowpack included the development of a substantial depth hoar layer composed of large faceted grains ($>$ 6 mm). Comparative analysis of measured snow properties and backscatter revealed Ku-band sensitivity to increasing depth and SWE which was considerably higher than previously demonstrated in literature.

The Ku-band co-polarized response demonstrated in chapter 5 was found to increase by approximately 1.3 dB for every 1-cm change in SWE. A similar response in cross-polarized backscatter was observed as 0.8 dB for every 1-cm change in SWE. This finding demonstrated Ku-band sensitivity to small changes in depth and SWE across a limited range of representative tundra snow conditions. Analysis of the response from the longer wavelength X-band measurements suggested that the observed seasonal change in backscatter was not only modified by changing snow conditions, but also was heavily influenced by the underlying soil condition. The potential for X-band snow retrievals under shallow con-

ditions was therefore less clear than at Ku-band. A large change in the January X-band response suggested that the observed seasonal trend was influenced by a combination of snow and soil properties including moisture. At the conclusion of the experiment, snow was removed from the scatterometer field of view to measure the backscatter response from bare soil surface. At both frequencies, large decreases in backscatter were observed when the late season snowpack was removed. In contrast to the removal experiment presented in chapter 4, the substantial reduction at both frequencies demonstrated definitive Ku- and X-band sensitivity to the snow volume. The end of season snowpack observed in chapter 5 contained much larger basal depth hoar grains with a stronger preference to vertical orientation than found in the chapter 4 removal experiment. The differences between the two experiments suggest that X-band sensitivity evolves with seasonal snow metamorphosis and may be of use in areas subjected to sustained periods of kinetic grain growth. As in the previous study, the use of a dual-frequency approach is supported if snow depth, SWE, or grain size have evolved sufficiently to solicit an X-band backscatter response. Despite this, under the observed conditions a single frequency Ku-band retrieval would be sufficient to characterize the full range of depth and SWE encountered during the experiment.

In chapter 6, a distributed set of snow covered tundra targets were measured in a complementary experiment aimed at assessing spatiotemporal variability in backscatter response. As Ku-band measurements had been shown to be sufficient for observation of tundra accumulation, a single frequency approach was used. In a sled mounted configuration, the scatterometer was transported to 26 open tundra sites where coincident measurements of backscatter and snow properties were made between October 2010 and March 2011. The snow sampling protocol was modified from the previous chapter to include a destructive sampling scheme within the scatterometer field of view after each radar scan was completed. In doing so, the variability of snow properties at a scale sub-scan to the

observing instrument were quantified and evaluated. Again, Ku-band measurements were shown to be sensitive to tundra snow properties including depth and SWE. Ku-band σ^0_{vv} was found to increase by 0.82 dB for every 1 cm in SWE and σ^0_{hh} by 0.62 dB for every 1 cm increase. Similar increases were also observed in the cross-polarized σ^0_{hh} response where backscatter increased by 0.80 dB for every 1 cm increase in SWE.

Overall, this research contributes a number of important field-based observations that will aid in the development of radar based snow property retrievals and serve to validate existing models. Of particular note are defined sensitivities at Ku-band to evolving terrestrial snow properties, across a narrow range of depth and SWE, typical of tundra environments. Furthermore, Ku-band observations conveyed information about subtle changes in snow physical and dielectric properties opening the potential for detailed observations of changes in snow energy and mass balance at the scale of ground observed variations. While the analysis and interpretation of X-band backscatter proved to be challenging, the results do not exclude effectivity of the longer wavelength for estimating tundra snow properties. Evidence of X-band sensitivity to SWE was shown in analysis, but was complicated by uncertainties related to the soil scattering component.

A comprehensive set of seasonal, spatial, and destructive snow-radar experiments have been presented which exemplify the potential for Ku- and X-band retrieval of tundra snow properties. The presented research warrants further experimentation to address outstanding questions involving the influence of snow layering, grain size, and scaling of land cover features on Ku- and X-band backscatter.

7.2 Limitations

7.2.1 Soil properties

The most evident limitation of this thesis was the lack of measurements characterizing spatiotemporal variability in surface roughness and dielectric properties of soil. Chapters 4 and 5 demonstrated uncertainties in the seasonal X-band response which were unaccounted for in the snow measurements and ultimately attributed to changes of unquantified soil state. Discussion of soil-radar interactions in each chapter was further complicated by the general lack of literature regarding winter season dielectric properties of organic soils. Recent laboratory based research has suggested that organic soils are capable of retaining residual amounts of moisture at -5°C for extended periods of time (Nagare et al., 2012). Early season soil state previously thought to have been frozen after sustained periods of below 0°C surface temperatures may have retained residual moisture content capable of producing strong surface reflections. Left unquantified, the influence of soil state on the longer wavelength X-band measurements created signal noise that could not otherwise be decomposed from the desired snow volume response, and therefore confounding the retrieval of the desired snow properties.

7.2.2 Objective measurement of grain size

Chapters 4, 5 and 6 identified extended periods of temperature gradient metamorphosis which produced large depth hoar grains throughout the study area. The development of a prevalent depth hoar layer was not instantaneous as suggested by optical grain size measurements; the depth hoar layer increased gradually throughout the observation period. According to electromagnetic theory, the observed increase should result in prevalent

multiple-scattering as grain size approached the observing radar wavelength. While an amplified backscatter response was identified in Chapter 4 at Ku- and X-band, it was not possible to directly evaluate measured grain size statistics against backscatter due to the limitations of the sampling method used. As a qualitative descriptor, observer notes on grain size and shape were extremely useful for the identification of seasonal trends and local metamorphic processes. Unfortunately, quantitative evaluation of grain size was impaired by inherent biases introduced by observer based visual characterization. Here, operators relied on their own judgement to select representative set of snow grains and were required to complete characterizations under harsh sub-arctic conditions which stressed operator skill. At best, the visually interpreted grain size measurements were accurate to the nearest millimetre and therefore, were difficult to use in comparative analysis where sub-millimetre changes are highly influential on the radar response.

7.2.3 Scaling of observations

In the absence of space-borne observations, ground-based systems such as UW-Scat have been deployed to characterize microwave interactions with snow at scales much smaller than those possible with potential satellite missions. Despite the benefits of such studies, direct scaling to space-borne observation is difficult because of the deterioration of target heterogeneity at large scales. The CoReH$_2$O mission specifications called for a minimum spatial resolution of 50 $\times$ 50 m, a scale much larger than ground-based measurements collected as part of CASIX (Rott et al., 2010). The measurement protocol used in this thesis provided measurements representative of the snow conditions for a limited spatial extent at a single point in time. The short temporal scales of accumulation and metamorphic processes in Churchill made it difficult to collect a sufficient number of distributed

observations over short periods to characterize what would be considered a single pixel of a potential satellite mission. Moreover, measurements collected in open tundra areas did not include standing vegetation or significant variations in topography, which at satellite scales, are considerable modifiers of backscatter. In general, the ground-based system deployed does not allow sufficient range to target for integration of observations with standing vegetation and snow. Therefore, ground-based observations presented in this thesis should be considered as a first step towards an integrated study approach in which airborne and additional under flight testing is included to develop an improved spatial understanding of the physical interaction processes.

7.3 Recommendations and future work

This thesis demonstrates the sensitivity of Ku- and X-band radar measurements to snowpack properties. Observational analysis presented in this thesis would greatly benefit from application of electromagnetic models addressing snow volume and soil surface interactions. An emerging set of dense media radiative transfer (DMRT) models have shown considerable promise for simulation of polarimetric snow response at Ku- and X-band (e.g. Du et al., 2010; Tsang et al., 2007; Tse et al., 2007; Xu et al., 2010, 2012; Zurk et al., 1996). These studies have indicated backscatter uncertainties related to changes in grain size and shape similar to those encountered in chapters 4 and 5. Application of the tundra snow and backscatter measurements collected as part of CASIX would enable the evaluation of snow grain conditions previously untested and/or considered to be outliers in current DMRT implementations. As a diagnostic tool, current DMRT implementations are well suited for snow research but have not yet demonstrated the maturity needed to account for the full interaction space encountered in field-based applications. For example, Yueh et al.

(2009) called for improvements to electromagnetic models when significant differences (> 10 dB) were noted between field-observed cross-polarized backscatter and a DMRT model estimates. These models often lack representation for non-spherical particles; an issue of uncertainty as recently discussed by Du et al. (2010) when natural snow conditions are considered. Also, adaptations of DMRT, such as those introduced by Xu et al. (2010, 2012), have focused on refined non-spherical representation of snow and may be suited for evaluation of the tundra snow presented in this thesis. There is an immediate need for improved collaboration between modelling and observational communities to improve our understanding of snow-radar interactions for property retrieval across all snow cover types.

In addition to snow, application of electromagnetic models to explore soil scattering could improve observational analysis presented in this thesis. Using inversion techniques, soil scattering models could assist in filling dielectric and surface roughness data gaps introduced as a general limitation of analysis. Unfortunately, organic soils encountered in the observed study area are not well represented in the current literature and would require significant study to characterize interactions related to seasonal and spatial processes. Recent work by Mironov et al. (2010) has introduced laboratory based experimentation to simulate dielectric state of organic soils at microwave frequencies. This model could be used as an accessible means to characterize surface reflections contributing to soil scattering in the study area or for inversion of soil properties. Traditional semi-physically and physically based surface scattering models may also be of use to interpolate interactions observed at X-band which were unaccounted for in the seasonal snow evolution (e.g. Fung et al., 1992; Oh et al., 1992). The use of these traditional models would require investigation to determine their applicability in the Churchill study area and the unique conditions encountered in this environment. In the future, detailed study of bare soil measurements against a suite

of electromagnetic models could provide a starting point for evaluation of winter season scattering processes and serve to reduce uncertainty regarding seasonal X-band response.

Improvement to field-based observation measurements and protocols is an area of limitation which can be immediately addressed in future study of snow-microwave interaction. Repeatable grain property measurements, where operator bias is minimized, will enable more quantitative analysis to evaluate the influence of field-observed seasonal grain metamorphosis. Several emerging tools for objective characterization of snow grain properties, including optical transmission sensors, infrared integrating spheres, shortwave infrared cameras and digital snow penetrometers show excellent promise for repeatable field-based observation of snow grain properties (Kasurak et al., 2013; Langlois et al., 2010; Montpetit et al., 2012; Schneebeli et al., 1999). Community efforts are currently underway to complete inter-comparison projects and promote common tools so that results and analysis can be universally compared. In addition to grain sensors, sensors capable of soil dielectric measurements should be deployed in future studies to characterize spatiotemporal processes in a variety of soil types, especially organic soils. A spatially distributed set of sensors could assist in interpretation of X-band backscatter response and assist in the development of electromagnetic models applicable for use with organic soils. In the future, the addition of these tools will be important for the advancement of field-based snow-radar observation.

APPENDICES

Appendix A

UW-Scat hardware

A.1 Radio frequency hardware block diagrams

The following illustrates the University of Waterloo scatterometer Ku- and X-band radio frequency hardware as block diagrams. Detailed component descriptions are provided in Chapter 3.

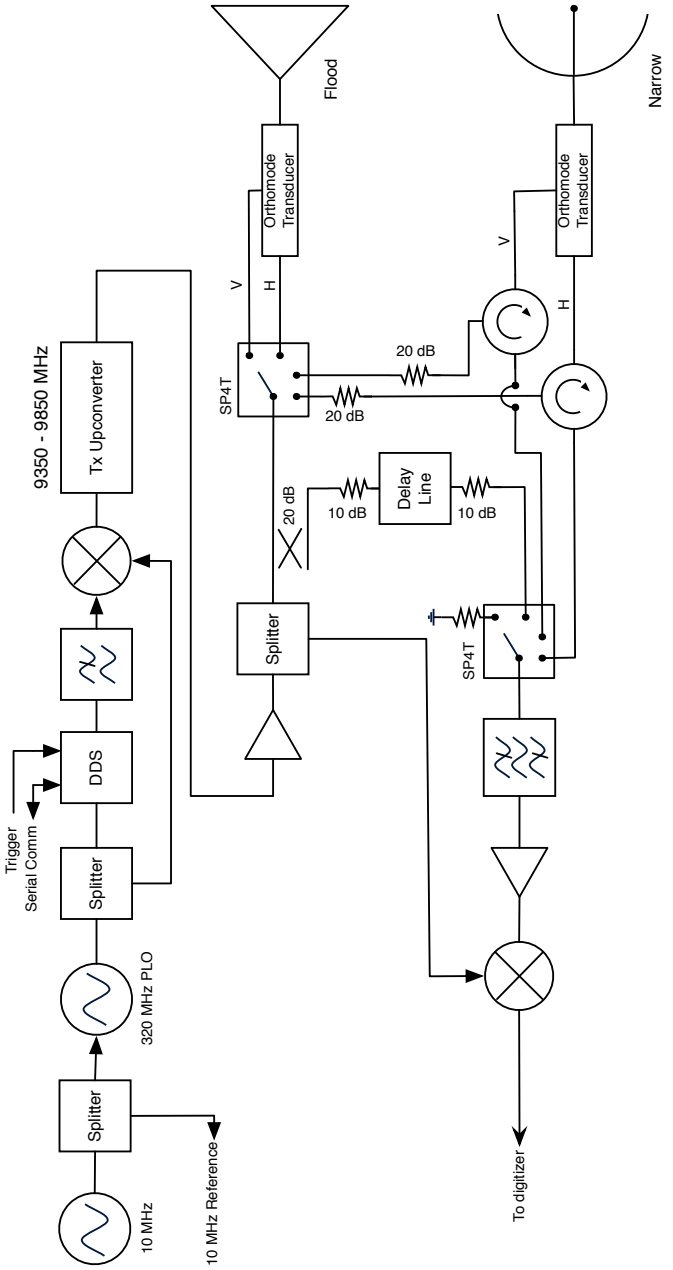

Figure A.1: Block diagram of the University of Waterloo Scatterometer X-band radio frequency unit.

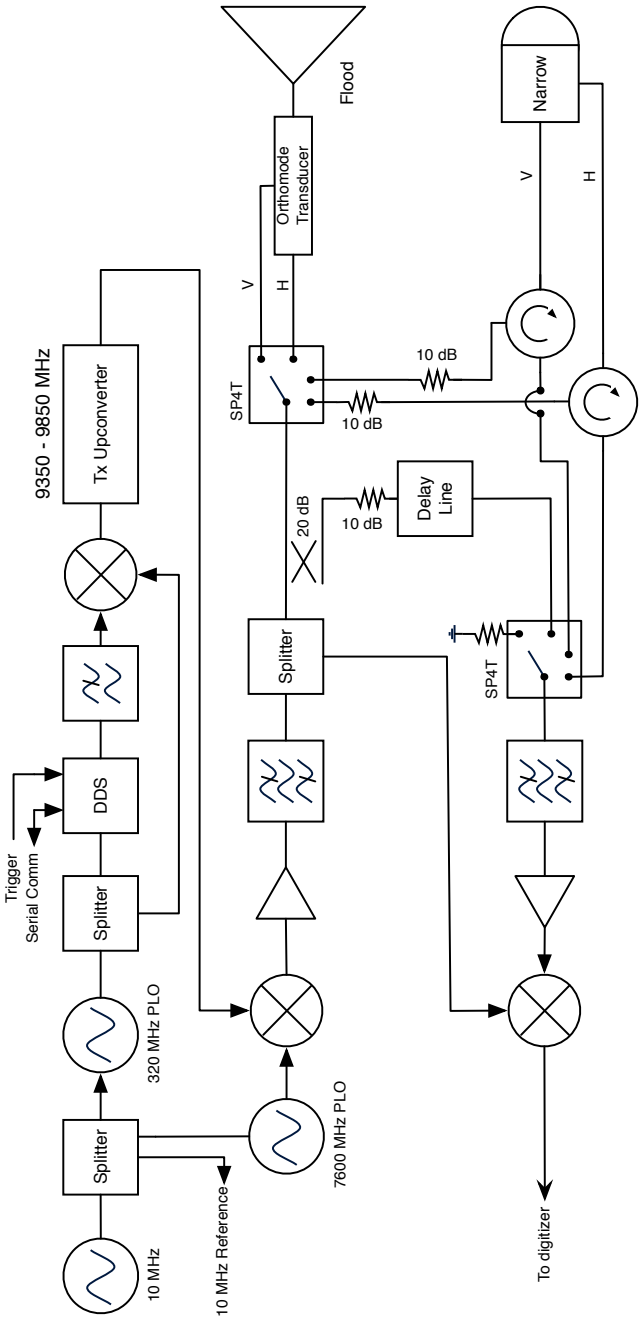

Figure A.2: Block diagram of the University of Waterloo Scatterometer Ku-band radio frequency unit.

A.2 Scatterometer footprint

Mounted aboard a snow-machine pulled sled, UW-Scat typically operates in close proximity to its intended snow target. Due to this, small changes in the geometry of the sensor may cause significant variation in the size and shape of the illuminated target area. This area of illumination, known as the footprint, is elliptical in shape with a major axis oriented parallel to the scatterometer range direction. As radar remote sensing of snow relies heavily on estimates of area normalized backscatter, it is important that any changes in the scatterometer footprint be carefully considered to minimize bias in the presented results.

The dimensions of the scatterometer footprint are a function of system geometry including elevation angle, antenna beamwidth, antenna height, and distance to the target. Antenna beamwidth and elevation angle are automatically associated with each data block based on user specified scan parameters. The height of the antenna (H_{a}) is estimated numerically for each scan line as

$$H_{\mathrm{a}} = H_{\mathrm{p}} + R_{\mathrm{b}} \sin\phi - R_{\mathrm{y}} \cos\phi \tag{A.1}$$

where H_{p} is the height of the positioning system elevation axis; R_{b} is the offset of the antenna phase centre from the positioning system elevation axis; R_{y} is the offset of the antenna phase center from the RF unit mounting bracket in the direction orthogonal to the primary offset; and ϕ is the elevation angle. Figure A.3 illustrates the geometry of equation A.1 as used to estimate H_{a} under field conditions. Constant values of 0.64 m and 0.23 m are used for R_{b} and R_{y}. The remaining unknown, H_{p}, is measured manually by system operators prior to the start of each scan. Unfortunately, this is a potential source of error

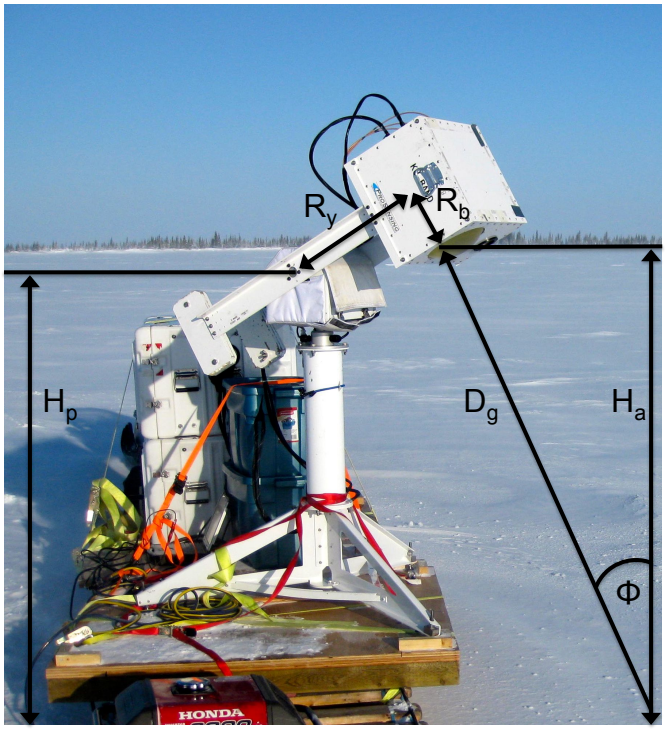

Figure A.3: Visualization of the geometry for estimating antenna height.

as operator bias may be introduced depending on the precision of the estimate. Between elevation angles of 30° and 45° the impact of operator bias is generally acceptable. For example, a 10 cm error in H_{p} causes a misestimation of approximately 0.045 m^2 or 10.06% of the footprint area. In general, it is expected that H_{p} is measured with an accuracy $>$ 10 cm as operators were advised of the importance of this procedure.

Once antenna height is resolved, the geometric distance to target (D_g) can be determined using trigonometry such that

$$D_g = \frac{H_{\mathrm{a}}}{\cos\phi}. \tag{A.2}$$

Geometric range estimated in equation A.2 makes the assumption that the distance from the ground target to a plane horizontal to the antenna is the same as the total antenna height. Under field conditions, actual distances may differ due to local variation in snow volume and topography[1]. As a first estimate using geometric range to target, the scatterometer footprint is approximated as

$$E_a = D_g \theta_{3\text{db}} / \cos\phi \tag{A.3}$$

$$E_b = D_g \theta_{3\text{db}} \tag{A.4}$$

where E_a is the major axis of the footprint ellipse ; and E_b is the minor axis of the footprint ellipse. From equations A.3 and A.4 it is apparent that the major axis of the footprint, and thus area, will change significantly at steep elevation angles when operated in close proximity to a target. Below elevation angles of 50°, the Ku- and X-band footprint increases gradually to a value >1 m^2 in narrow and flood beam mode. Beyond 50°, the illuminated area increases rapidly as the major axis of the footprint elongates in range. This increase is common to both frequencies and acquisition modes. Within the range of the CoReH_2O proposed incident angles, only a small change in the footprint dimensions is observed (Table A.1). This is favourable as there is no significant departure in the area over which incident energy is scattered within the desired elevation range.

[1] A refined distance to target is produced in post processing using the radar echo.

Table A.1: Dimensions of the scatterometer footprint at 30° and 40°. Minor axis, major axis, and footprint area estimates presented for both narrow and flood beam.

Parameter	Ku-band		X-band	
	30°	45°	30°	45°
Minor Axis (m)	0.21 / 0.28	0.28 / 0.37	0.16 / 0.21	0.21 / 0.29
Major Axis (m)	0.24 / 0.32	0.39 / 0.52	0.18 / 0.25	0.30 / 0.40
Footprint Area (m^2)	0.15 / 0.28	0.34 / 0.60	0.09 / 0.16	0.20 / 0.36

A.3 Scatterometer quality and error metrics

A.3.1 Independent samples

A rough estimate of beam-limited independent samples can be obtained by dividing the scan angular width by half the antenna beamwidth. When the major axis of the footprint exceeded the range resolution of the sensor (30 cm) the number of gates within the footprint was multiplied by the initial estimate to obtain independent samples in range. Applying the common 60° azimuth range, a minimum of 21 independent samples at 21° and a maximum of 567 at 81° were observed with the Ku-band RF unit. Using the same scan parameters a minimum of 28 at 21° and maximum of 586 at 81° were observed with the X-band RF unit. As elevation increased, the number of independent samples increased as the backscattered signal was spread over multiple range gates within the footprint. Logistical restraints including the height of the sensor RF unit prevented the practical collection of a larger number of samples under field conditions.

Signal-to-noise ratio

In addition to independent samples, SNR was calculated for each elevation angle. SNR was calculated by dividing the selected impulse range power by the total sky observation power over the same range. Both frequencies presented strong VV SNR across a large range of incident angles. SNR began to deteriorate at approximately 70° when backscattered energy was spread across a large number of range gates. Minimum SNRs of 28.7 and 20.6 at X- and Ku-band were observed at 81°. Cross-polarized returns also presented strong SNR well above the noise floor at elevation angles $> 70°$. Minimum X- and Ku-band SNRs of 18.8 and 9.8 were observed at 81°.

Random error

Random error in σ^0 is estimated as (Sarabandi et al., 1990):

$$\sigma_{ran} = \sqrt{\frac{1}{N_{ind}}\left(1+\frac{1}{SNR}\right)^2 + \frac{1}{N_n}\left(\frac{1}{SNR}\right)^2} \tag{A.5}$$

where N_{ind} is the number of independent samples and N_n is the number of noise samples. UW-Scat calculates N_n as the number of sky observations used. As they are averaged in preprocessing a value of 1 is assigned. The estimate of σ_{ran} assumes that the sky observation has been coherently subtracted from the received power when signal power is estimated.

Multiplicative Bias Errors

The calibration process used in the field was a source of error for offline processing. The corner reflector, which was supported by a tripod, may have generated correlated scatter causing signal clutter of the reference target. The resulting calibration bias can be estimated based on a signal-to-clutter (SCR) power ratio by the following two equations (Geldsetzer et al., 2007):

$$\Gamma^{+}_{cal} = \frac{1}{(1-\frac{1}{\sqrt{SCR}})^2} \tag{A.6}$$

$$\Gamma^{-}_{cal} = \frac{1}{(1+\frac{1}{\sqrt{SCR}})^2} \tag{A.7}$$

SCR in the field is estimated with observations of the support tripod without the reference target attached. The two calculations estimate out-of-phase and in-phase bias,

respectfully. Additional residual multiplicative calibration errors are lumped into a constant Γ_{res} with a conservative assumed value of 0.5 dB. These biases may result from factors such as misestimating range, antenna footprint, and incidence angle.

Total Error

An estimate of total error is calculated as positive and negative components. Total positive and negative errors are given by (Geldsetzer et al., 2007):

$$\Delta^{+}_{total} = \Gamma^{+}_{cal}\Gamma^{+}_{res}(1 + \sigma_{ran}) \tag{A.8}$$

$$\Delta^{-}_{total} = \Gamma^{-}_{cal}\Gamma^{-}_{res}(1 + \sigma_{ran}) \tag{A.9}$$

Copyright Permissions

IEEE COPYRIGHT AND CONSENT FORM

To ensure uniformity of treatment among all contributors, other forms may not be substituted for this form, nor may any wording of the form be changed. This form is intended for original material submitted to the IEEE and must accompany any such material in order to be published by the IEEE.Please read the form carefully and keep a copy for your files.

TITLE OF PAPER/ARTICLE/REPORT, INCLUDING ALL CONTENT IN ANY FORM, FORMAT, OR MEDIA (hereinafter, "The Work"):**UW-Scat - Ground-Based Dual Frequency Scatterometry for Observation of Snow Properties**

COMPLETE LIST OF AUTHORS:**King, Joshua; Kelly, Richard; Kasurak, Andrew; Gunn, Grant; Duguay, Claude; Mead, James**

IEEE PUBLICATION TITLE (Journal, Magazine, Conference, Book):**Geoscience and Remote Sensing Letters**

COPYRIGHT TRANSFER

1. The undersigned hereby assigns to The Institute of Electrical and Electronics Engineers,Incorporated (the "IEEE") all rights under copyright that may exist in and to: (a) the above Work,including any revised or expanded derivative works submitted to the IEEE by the undersigned based on the Work; and (b) any associated written or multimedia components or other enhancements accompanying the Work.

CONSENT AND RELEASE

2. ln the event the undersigned makes a presentation based upon the Work at a conference hosted or sponsored in whole or in part by the IEEE, the undersigned, in consideration for his/her participation in the conference, hereby grants the IEEE the unlimited, worldwide, irrevocable permission to use, distribute, publish, license, exhibit, record, digitize, broadcast, reproduce and archive, in any format or medium, whether now known or hereafter developed: (a) his/her presentation and comments at the conference; (b) any written materials or multimedia files used in connection with his/her presentation; and (c) any recorded interviews of him/her (collectively, the "Presentation"). The permission granted includes the transcription and reproduction ofthe Presentation for inclusion in products sold or distributed by IEEE and live or recorded broadcast ofthe Presentation during or after the conference.

3. In connection with the permission granted in Section 2, the undersigned hereby grants IEEE the unlimited, worldwide, irrevocable right to use his/her name, picture, likeness, voice and biographical information as part of the advertisement, distribution and sale ofproducts incorporating the Work or Presentation, and releases IEEE from any claim based on right of privacy or publicity.

4. The undersigned hereby warrants that the Work and Presentation (collectively, the "Materials") are original and that he/she is the author of the Materials. To the extent the Materials incorporate text passages, figures, data or other material from the works of others, the undersigned has obtained any necessary permissions. Where necessary, the undersigned has obtained all third party permissions and consents to grant the license above and has provided copies of such permissions and consents to IEEE.

[ ] Please check this box ifyou do not wish to have video/audio recordings made ofyour conference presentation.

See below for Retained Rights/Terms and Conditions, and Author Responsibilities.

AUTHOR RESPONSIBILITIES

The IEEE distributes its technical publications throughout the world and wants to ensure that the material submitted to its publications is properly available to the readership of those publications. Authors must ensure that their Work meets the requirements as stated in section 8.2.1 of the IEEE

PSPB Operations Manual, including provisions covering originality, authorship, author responsibilities and author misconduct. More information on IEEEs publishing policies may be found at http://www.ieee.org/publications_standards/publications/rights/pub_tools_policies.html. Authors are advised especially of IEEE PSPB Operations Manual section 8.2.1.B12: "It is the responsibility of the authors, not the IEEE, to determine whether disclosure of their material requires the prior consent of other parties and, if so, to obtain it." Authors are also advised of IEEE PSPB Operations Manual section 8.1.1B: "Statements and opinions given in work published by the IEEE are the expression of the authors."

RETAINED RIGHTS/TERMS AND CONDITIONS

General

1. Authors/employers retain all proprietary rights in any process, procedure, or article of manufacture described in the Work.

2. Authors/employers may reproduce or authorize others to reproduce the Work, material extracted verbatim from the Work, or derivative works for the author's personal use or for company use, provided that the source and the IEEE copyright notice are indicated, the copies are not used in any way that implies IEEE endorsement of a product or service of any employer, and the copies themselves are not offered for sale.

3. In the case of a Work performed under a U.S. Government contract or grant, the IEEE recognizes that the U.S. Government has royalty-free permission to reproduce all or portions of the Work, and to authorize others to do so, for official U.S. Government purposes only, if the contract/grant so requires.

4. Although authors are permitted to re-use all or portions of the Work in other works, this does not include granting third-party requests for reprinting, republishing, or other types of re-use.The IEEE Intellectual Property Rights office must handle all such third-party requests.

5. Authors whose work was performed under a grant from a government funding agency are free to fulfill any deposit mandates from that funding agency.

Author Online Use

6. Personal Servers. Authors and/or their employers shall have the right to post the accepted version of IEEE-copyrighted articles on their own personal servers or the servers of their institutions or employers without permission from IEEE, provided that the posted version includes a prominently displayed IEEE copyright notice and, when published, a full citation to the original IEEE publication, including a link to the article abstract in IEEE Xplore.Authors shall not post the final, published versions of their papers.

7. Classroom or Internal Training Use. An author is expressly permitted to post any portion of the accepted version of his/her own IEEE-copyrighted articles on the authors personal web site or the servers of the authors institution or company in connection with the authors teaching, training, or work responsibilities, provided that the appropriate copyright, credit, and reuse notices appear prominently with the posted material. Examples of permitted uses are lecture materials, course packs, e-reserves, conference presentations, or in-house training courses.

8. Electronic Preprints. Before submitting an article to an IEEE publication, authors frequently post their manuscripts to their own web site, their employers site, or to another server that invites constructive comment from colleagues.Upon submission of an article to IEEE, an author is required to transfer copyright in the article to IEEE, and the author must update any previously posted version of the article with a prominently displayed IEEE copyright notice. Upon publication of an article by the IEEE, the author must replace any previously posted electronic versions of the article with either (1) the full citation to the IEEE work with a Digital Object Identifier (DOI) or link to the article abstract in IEEE Xplore, or (2) the accepted version only (not the IEEE-published version), including the IEEE copyright notice and full citation, with a link to the final, published article in IEEE Xplore.

INFORMATION FOR AUTHORS

IEEE Copyright Ownership

It is the formal policy of the IEEE to own the copyrights to all copyrightable material in its technical publications and to the individual contributions contained therein, in order to protect the interests of the IEEE, its authors and their employers, and, at the same time, to facilitate the appropriate re-use of this material by others.The IEEE distributes its technical publications throughout the world and does so by various means such as hard copy, microfiche, microfilm, and electronic media.It also abstracts and may translate its publications, and articles contained therein, for inclusion in various compendiums, collective works, databases and similar publications.

Author/Employer Rights

If you are employed and prepared the Work on a subject within the scope of your employment, the copyright in the Work belongs to your employer as a work-for-hire. In that case, the IEEE assumes that when you sign this Form, you are authorized to do so by your employer and that your employer has consented to the transfer of copyright, to the representation and warranty of publication rights, and to all other terms and conditions of this Form. If such authorization and consent has not been given to you, an authorized representative of your employer should sign this Form as the Author.

GENERAL TERMS

1. The undersigned represents that he/she has the power and authority to make and execute this form.
2. The undersigned agrees to identify and hold harmless the IEEE from any damage or expense that may arise in the event of a breach of any of the warranties set forth above.
3. In the event the above work is not accepted and published by the IEEE or is withdrawn by the author(s) before acceptance by the IEEE, the foregoing grant of rights shall become null and void and all materials embodying the Work submitted to the IEEE will be destroyed.
4. For jointly authored Works, all joint authors should sign, or one of the authors should sign as authorized agent for the others.

Joshua King	**18-05-2012**
Author/Authorized Agent For Joint Authors	**Date(dd-mm-yy)**

THIS FORM MUST ACCOMPANY THE SUBMISSION OF THE AUTHOR'S MANUSCRIPT.
Questions about the submission of the form or manuscript must be sent to the publication's editor.Please direct all questions about IEEE copyright policy to:
IEEE Intellectual Property Rights Office, copyrights@ieee.org, +1-732-562-3966 (telephone)

References

Adams, E. E. and Miller, D. A. (2003). Ice crystals grown from vapor onto an orientated substrate: application to snow depth-hoar development and gas inclusions in lake ice. *Journal of Glaciology*, 49(164):8–12.

Ahrens, C. D. (2007). *Meteorology today: An introduction to weather, climate, and the environment*. Thomson Brooks Cole, Belmont, USA.

Armstrong, R. (1980). An analysis of compressive strain in adjacent temperature-gradient and equi-temperature layers in a natural snow cover. *Journal of Glaciology*, 26(94):283–289.

Arons, E. M. and Colbeck, S. C. (1995). Geometry of heat and mass-transfer in dry snow - A review of theory and experimentation. *Reviews of Geophysics*, 33(4):463–493.

Baker-Jarvis, J. (2000). A generalized dielectric polarization evolution equation. *IEEE Transactions on Dielectrics and Electrical Insulation*, 7(3):374–386.

Barnett, T. P., Adam, J. C., and Lettenmaier, D. P. (2005). Potential impacts of a warming climate on water availability in snow-dominated regions. *Nature*, 438(7066):303–309.

Baumgartner, F., Munk, J., Jezek, K., and Gogineni, S. (2002). On reconciling ground-based with spaceborne normalized radar cross section measurements. *IEEE Transactions on Geoscience and Remote Sensing*, 40(2):494–496.

Berry, M. O. and Maxwell, J. B. (1981). Snowfall formation. In Gray, D. M. and Male, D. H., editors, *Handbook of snow: Principles, processes, management & use*, chapter 4, pages 129–151. Pergamon Press, Toronto.

Bjerrum, N. (1952). Structure and properties of ice. *Science*, 115(2989):385–390.

Brown, R., Derksen, C., and Wang, L. (2010). A multi-data set analysis of variability and change in Arctic spring snow cover extent, 1967–2008. *Journal of Geophysical Research-Earth Surface*, 115:D16111.

Brown, R. D. (2000). Northern hemisphere snow cover variability and change, 1915–97. *Journal of Climate*, 13:2339–2355.

Brown, R. D., Brasnett, B., and Robinson, D. (2003). Gridded north american monthly snow depth and snow water equivalent for GCM evaluation. *Atmosphere Ocean*, 41(1):1–14.

Brown, R. D. and Mote, P. W. (2009). The response of Northern Hemisphere snow cover to a changing climate. *Journal of Climate*, 22(8):2124–2145.

Brown, R. D. and Robinson, D. A. (2011). Northern Hemisphere spring snow cover variability and change over 1922–2010 including an assessment of uncertainty. *The Cryosphere*, 5:219–229.

Chapin, F. S., Sturm, M., Serreze, M. C., McFadden, J. P., Key, J. R., Lloyd, A. H., McGuire, A. D., Rupp, T. S., Lynch, A. H., Schimel, J. P., Beringer, J., Chapman, W. L., Epstein, H. E., Euskirchen, E. S., Hinzman, L. D., Jia, G., Ping, C.-L., Tape, K. D., Thompson, C. D. C., Walker, D. A., and Welker, J. M. (2005). Role of land-surface changes in arctic summer warming. *Science*, 310:657–660.

Clark, M. P., Hendrikx, J., Slater, A. G., Kavetski, D., Anderson, B., Cullen, N. J., Kerr, T., Örn Hreinsson, E., and Woods, R. A. (2011). Representing spatial variability of snow water equivalent in hydrologic and land-surface models: A review. *Water resources research*, 47:W07539.

Cohen, J. L., Furtado, J. C., Barlow, M. A., Alexeev, V. A., and Cherry, J. E. (2012). Arctic warming, increasing snow cover and widespread boreal winter cooling. *Environmental Research Letters*, 7:014007.

Colbeck, S. C. (1980). Thermodynamics of snow metamorphism due to variations in curvature. *Journal of Glaciology*, 26(94):291–301.

Colbeck, S. C. (1982a). An overview of seasonal snow metamorphism. *Reviews of Geophysics*, 20(1):45–61.

Colbeck, S. C. (1982b). The geometry and permittivity of snow at high-frequencies. *Journal of Applied Physics*, 53(6):4495–4500.

Colbeck, S. C. (1983). Theory of metamorphism of dry snow. *Journal of Geophysical Research*, 88(C9):5475–5482.

Colbeck, S. C. (1986). Classification of seasonal snow cover crystals. *Water Resources Research*, 22(9):59S–70S.

Colbeck, S. C. (1991). The layered character of snow covers. *Reviews of Geophysics*, 29(1):81–96.

Colbeck, S. C. and Jamieson, J. B. (2001). The formation of faceted layers above crusts. *Cold Regions Science and Technology*, 33:247–252.

Cook, B. I., Bonan, G. B., Levis, S., and Epstein, H. E. (2007). The thermoinsulation effect of snow cover within a climate model. *Climate Dynamics*, 31:107–124.

Cumming, W. A. (1952). The dielectric properties of ice and snow at 3.2 centimeters. *Journal of Applied Physics*, 23(7):768–773.

Debye, P. (1929). *Polar Molecules*. Chemical Catalog Company, New York.

Deems, J. S., Fassnacht, S. R., and Elder, K. J. (2008). Interannual consistency in fractal snow depth patterns at two Colorado mountain sites. *Journal of Hydrometeorology*, 9(5):977–988.

Derksen, C. (2008). The contribution of AMSR-E 18.7 and 10.7 GHz measurements to improved boreal forest snow water equivalent retrievals. *Remote Sensing of Environment*, 112(5):2701–2710.

Derksen, C. and Brown, R. (2012). Spring snow cover extent reductions in the 2008–2012 period exceeding climate model projections. *Geophysical Research Letters*, 39(19):L19504.

Derksen, C., Silis, A., Sturm, M., Holmgren, J., Liston, G. E., Huntington, H., and Solie, D. (2009). Northwest Territories and Nunavut snow characteristics from a subarctic traverse: implications for passive microwave remote sensing. *Journal of Hydrometeorology*, 10(2):448–463.

Derksen, C., Smith, S. L., Sharp, M., Brown, L., Howell, S., Copland, L., Mueller, D. R., Gauthier, Y., Fletcher, C. G., Tivy, A., Bernier, M., Bourgeois, J., Brown, R., Burn, C. R., Duguay, C., Kushner, P., Langlois, A., Lewkowicz, A. G., Royer, A., and Walker, A. (2012a). Variability and change in the Canadian cryosphere. *Climatic Change*, 115(1):59–99.

Derksen, C., Toose, P., Lemmetyinen, J., Pulliainen, J., Langlois, A., Rutter, N., and Fuller, M. C. (2012b). Evaluation of passive microwave brightness temperature simulations and snow water equivalent retrievals through a winter season. *Remote Sensing of Environment*, 117:236–248.

Derksen, C., Toose, P., Rees, A., Wang, L., English, M., Walker, A., and Sturm, M. (2010). Development of a tundra-specific snow water equivalent retrieval algorithm for satellite passive microwave data. *Remote Sensing of Environment*, 114(8):1699 – 1709.

Derksen, C., Walker, A. E., Goodison, B. E., and Strapp, J. W. (2005). Integrating in situ and multiscale passive microwave data for estimation of subgrid scale snow water equivalent distribution and variability. *IEEE Transactions on Geoscience and Remote Sensing*, 43(5):960–972.

Domine, F., Gallet, J.-C., Bock, J., and Morin, S. (2012). Structure, specific surface area and thermal conductivity of the snowpack around Barrow, Alaska. *Journal of Geophysical Research-Earth Surface*, 117:D00R14.

Domine, F., Morin, S., Brun, E., and Lafaysse, M. (2013). Seasonal evolution of snow permeability under equi-temperature and temperature-gradient conditions. *The Cryosphere Discussions*, 7(3):2725–2759.

Domine, F., Taillandier, A.-S., Cabanes, A., Douglas, T. A., and Sturm, M. (2009). Three examples where the specific surface area of snow increased over time. *The Cryosphere*, 3:31–39.

Du, J., Shi, J. C., and Rott, H. (2010). Comparison between a multi-scattering and multilayer snow scattering model and its parameterized snow backscattering model. *Remote Sensing of Environment*, 114:1089–1098.

Duguay, C. R., Pultz, T. J., Lafleur, P. M., and Drai, D. (2002). RADARSAT backscatter characteristics of ice growing on shallow sub-Arctic lakes, Churchill, Manitoba, Canada. *Hydrological Processes*, 16:1631–1644.

Dye, D. G. (2002). Variability and trends in the annual snow-cover cycle in Northern Hemisphere land areas, 1972-2000. *Hydrological Processes*, 16(15):3065–3077.

Dyer, J. L. and Mote, T. L. (2006). Spatial variability and trends in observed snow depth over North America. *Geophysical Research Letters*, 33(16):L16503.

Environment Canada (2013). Canadian monthly climate data and 1981-2010 normals.

Essery, R. and Pomeroy, J. (2004). Vegetation and topographic control of wind-blown snow distributions in distributed and aggregated simulations for an Arctic tundra basin. *Journal of Hydrometeorology*, 5:735–744.

Fierz, C., Armstrong, R., Durand, Y., Etchevers, P., Greene, E., McClung, D., Nishimura, K., Satyawali, P., and Sokratov, S. (2009). The international classification for seasonal snow on the ground. Technical document, UNESCO-IHP, Paris.

Floricioiu, D. and Rott, H. (2001). Seasonal and short-term variability of multifrequency, polarimetric radar backscatter of alpine terrain from SIR-C/X-SAR and AIRSAR data. *IEEE Transactions on Geoscience and Remote Sensing*, 39(12):2634–2648.

Foster, J., Sun, C., Walker, J., Kelly, R., Chang, a., Dong, J., and Powell, H. (2005). Quantifying the uncertainty in passive microwave snow water equivalent observations. *Remote Sensing of Environment*, 94(2):187–203.

Frei, A. and Gong, G. (2005). Decadal to century scale trends in North American snow extent in coupled atmosphere-ocean general circulation models. *Geophysical Research Letters*, 32:L18502.

Fujino, K., Wakahama, G., Suzuki, M., Matsumoto, T., and Kuroiwa, D. (1985). Snow stratigraphy measured by an active microwave system. *Annals of Glaciology*, 6:207–210.

Fung, A., Li, Z., and Chen, K. (1992). Backscattering from a randomly rough dielectric surface. *IEEE Transactions on Geoscience and Remote Sensing*, 30(2):356–369.

Fung, A. K. (1994). *Microwave scattering and emission models and their applications*. Artech house, Norwood, MA.

Geldsetzer, T., Mead, J. B., Yackel, J. J., Scharien, R. K., and Howell, S. E. L. (2007). Surface-based polarimetric C-band scatterometer for field measurements of sea ice. *IEEE Transactions on Geoscience and Remote Sensing*, 45(11):3405–3416.

Glen, J. W. and Paren, J. G. (1975). The electrical properties of snow and ice. *Journal of Glaciology*, 15:15–38.

Hall, D. (1987). Influence of depth hoar on microwave emission from snow in northern Alaska. *Cold Regions Science and Technology*, 13(3):225–231.

Hall, D., Chang, A., and Foster, J. (1986). Detection of the depth-hoar layer in the snow-pack of the Arctic coastal plain of Alaska, USA, using satellite data. *Journal of Glaciology*, 32(110):87–94.

Hall, D., Sturm, M., Benson, C., Chang, A., and JL (1991). Passive microwave remote and in situ measurements of artic and subarctic snow covers in Alaska. *Remote Sensing of*, 38(3):161–172.

Hall, D. K., Riggs, G. a., Foster, J. L., and Kumar, S. V. (2010). Development and evaluation of a cloud-gap-filled MODIS daily snow-cover product. *Remote Sensing of Environment*, 114(3):496–503.

Hallikainen, M., Hyyppa, J., Haapanen, J., Tares, T., Ahola, P., Pulliainen, J., and Toikka, M. (1993). A Helicopter-borne 8-channel ranging scatterometer for remote-sensing. 1. System descrition. *IEEE Transactions on Geoscience and Remote Sensing*, 31(1):161–169.

Hallikainen, M. and Sievinen, P. (2007). Use of QuickSCAT Ku-band scatterometer data for retrieval of seasonal snow characteristics in Finland. In *Geoscience and Remote Sensing Symposium, 2007. IGARSS 2007. IEEE International*, pages 1228–1228.

Hallikainen, M., Ulaby, F., and Abdelrazik, M. (1986). Dielectric properties of snow in the 3 to 37 GHz range. *IEEE Transactions on Antennas and Propagation*, 34(11):1329–1340.

Hoose, C. (2010). How important is biological ice nucleation in clouds on a global scale? *Environmental Research Letters*, 5:1–7.

IEEE (1998). Standard definitions of terms for radio wave propagation. Technical report, Institute of Electrical and Electronics Engineers.

IGOS (2007). Integrated Global Observing Strategy Cryosphere Theme Report - For the Monitoring of our Environment from Space and from Earth. Technical Report WMO/TD-No. 1405, IGOS.

Jonas, T., Marty, C., and Magnusson, J. (2009). Estimating the snow water equivalent form snow depth measurements in the Swiss Alps. *Journal of Hydrology*, 378:161–167.

Jordan, R., Albert, M., and Brun, E. (2008). Physical processes within the snow cover and their parameterization. In Armstrong, R. and Brun, E., editors, *Snow and Climate: Physical Processes, Surface Energy Exchange and Modeling*, chapter 2. Cambridge University Press, Cambridge.

Kasurak, A., Kelly, R., and King, J. (2013). A simple in-situ sensor for snow grain size measurement. *Hydrological Processes*, in review.

Kelly, R. E., Chang, A. T., Tsang, L., and Foster, J. L. (2003). A prototype AMSR-E global snow area and snow depth algorithm. *IEEE Transactions on Geoscience and Remote Sensing*, 41(2):230–242.

Kendra, J. R., Sarabandi, K., and Ulaby, F. (1998). Radar measurements of snow: experiment and analysis. *IEEE Transactions on Geoscience and Remote Sensing*, 36(3):864–879.

Kern, S., Brath, M., Fontes, R., Gade, M., Gurgel, K.-W., Kaleschke, L., Spreen, G., Schulz, S., Winderlich, A., and Stammer, D. (2009). Multi(3)Scat-A helicopter-based scatterometer for snow-cover and sea-ice investigations. *IEEE Geoscience and Remote Sensing Letters*, 6(4):703–707.

Kershaw, P. and McCulloch, J. (2007). Midwinter snowpack variation across the Arctic treeline, Churchill, Manitoba, Canada. *Arctic, Antarctic, and Alpine Research*, 39(1):9–15.

King, J., Kelly, R., Kasurak, A., Gunn, G., Duguay, C., and Mead, J. (2013). UW-Scat - A ground-based dual frequency scatterometer for observation of snow properties. *IEEE Geoscience and Remote Sensing Letters*, 10(3):528–532.

Koh, G., Yankielun, N. E., and Baptista, A. I. (1996). Snow cover chracterization using multiband FMCW radars. *Hydrological Processes*, 10:1609–1617.

LaChapelle, E. (1969). *Field guide to snow crystals*. University of Washington Press, Seattle.

Langlois, A., Royer, A., Montpetit, B., Picard, G., Brucker, L., Arnaud, L., Harvey-Collard, P., Fily, M., and Goita, K. (2010). On the relationship between snow grain morphology and in-situ near infrared calibrated reflectance photographs. *Cold Regions Science and Technology*, 61:34–42.

Legagneux, L., Tailliandier, A.-S., and Domine, F. (2004). Grain growth theories and the isothermal evolution of the specific surface area of snow. *Journal of Applied Physics*, 95(11):6175–6184.

Lemmetyinen, J., Pulliainen, J., Arslan, A., Rautiainen, K., Vehvilainen, J., Wiesmann, A., Nagler, T., Rott, H., Davidson, M., Schuettemeyer, D., and Kern, M. (2011). Analysis of active and passive microwave observations from the nosrex campaign. In *Geoscience and Remote Sensing Symposium (IGARSS), 2011 IEEE International*, pages 2737–2740.

Li, L. and Pomeroy, J. W. (1997). Estimates of threshold wind speeds for snow transport using meterological data. *Journal of Applied Meteorology*, 36(3):205–213.

Libbrecht, K. G. (2005). The physics of snow crystals. *Reports on Progress in Physics*, 68(4):855–895.

Liston, G. E. (2004). Representing subgrid snow cover heterogeneities in regional and global models. *Journal of Climate*, 17:1381–1397.

Liston, G. E. and Sturm, M. (1998). A snow-transport model for complex terrain. *Journal of Glaciology*, 44(148):498–516.

Luus, K. A., Kelly, R. E. J., Lin, J. C., Humphreys, E. R., Lafleur, P. M., and Oechel, W. C. (2013). Modeling the influence of snow cover on low Arctic net ecosystem exchange. *Environmental Research Letters*, 8(3):035045.

Marshall, H. P., Koh, G., and Forster, R. R. (2004). Ground-based frequency-modulated continuous wave radar measurements in wet and dry snowpacks, Colorado, USA: an analysis and summary of the 2002-03 NASA CLPX data. *Hydrological Processes*, 18(18):3609–3622.

Marshall, H. P., Koh, G., and Forster, R. R. (2005). Estimating alpine snowpack properties using FMCW radar. *Annals of Glaciology*, 40:157–162.

Mätzler, C. (1987). Applications of the interaction of microwaves with the natural snow. *Remote Sensing Reviews*, 2(2):259–387.

Mätzler, C. (1996). Microwave permittivity of dry snow. *IEEE Transactions on Geoscience and Remote Sensing*, 34(2):573–581.

Mätzler, C. and Wegmuller, U. (1987). Dielectic properties of freshwater ice at microwave frequencies. *Journal of Physics D-Applied Physics*, 20(12):1623–1630.

McCabe, G. J. and Wolock, D. M. (2010). Long-term variability in Northern Hemisphere snow cover and associations with warmer winters. *Climatic Change*, 99:141–153.

Mellor, M. (1977). Engineering of snow properties. *Journal of Glaciology*, 19(81):16–66.

Miller, D. and Adams, E. (2009). A microstructural dry-snow metamorphism model for kinetic crystal growth. *Journal of Glaciology*, 55(194):1003–1011.

Mironov, V. L., De Roo, R. D., and Savin, I. V. (2010). Temperature-Dependable Microwave Dielectric Model for an Arctic Soil. *IEEE Transactions on Geoscience and Remote Sensing*, 48(6):2544–2556.

Montpetit, B., Royer, A., Langlois, A., Cliche, P., Roy, A., Champollion, N., Picard, G., Domine, F., and Obbard, R. (2012). New shortwave infrared albedo measurements for snow specific surface area retrieval. *Journal of Glaciology*, 58(211):941–952.

Montpetit, B., Royer, A., Roy, A., Langlois, A., and Derksen, C. (2013). Snow Microwave Emission Modeling of Ice Lenses Within a Snowpack Using the Microwave Emission Model for Layered Snowpacks. *IEEE Transactions on Geoscience and Remote Sensing*, 51(9):4705–4717.

Morrison, K. and Bennett, J. (2014). Tomographic profiling—a technique for multi-incidence-angle retrieval of the vertical sar backscattering profiles of biogeophysical targets. *IEEE Transactions on Geoscience and Remote Sensing*, 52(2):1350–1355.

Morrison, K., Rott, H., Nagler, T., Rebhan, H., and Wursteisen, P. (2007). The SARALPS-2007 measurement campaign on X- and Ku-band backscatter of snow. In *2007 IEEE Geoscience and Remote Sensing Symposium*, pages 1207–1210. IEEE.

Mote, P. W. (2006). Climate-driven variability and trends in mountain snowpack in western North America. *Journal of Climate*, 19(23):6209–6220.

Nagare, R. M., Schincariol, R. A., Quinton, W. L., and Hayashi, M. (2012). Effects of freezing on soil temperature, freezing front propagation and moisture redistribution in peat: laboratory investigations. *Hydrology and Earth System Sciences*, 16(2):501–515.

Nakaya, U. (1954). *Snow crystals: Natural and artifical*. Harvard University Press, Cambridge.

Nghiem, S. V. and Tsai, W. (2001). Global snow cover monitoring with spaceborne Ku-band scatterometer. *IEEE Transactions on Geoscience and Remote Sensing*, 39(10):2118–2134.

Oh, Y., Sarabandi, K., and Ulaby, F. (1992). An empirical model and an inversion technique for radar scattering from bare soil surfaces. *IEEE Transactions on Geoscience and Remote Sensing*, 30(2):370–381.

Pettinato, S., Santi, E., Brogioni, M., Paloscia, S., Palchetti, E., and Xiong, C. (2013). The potential of cosmo-skymed sar images in monitoring snow cover characteristics. *IEEE Geoscience and Remote Sensing Letters*, 10(1):9–13.

Pinzer, B. R. and Schneebeli, M. (2009). Snow metamorphism under alternating temperature gradients: Morphology and recrystallization in surface snow. *Geophysical Research Letters*, 36(23):10–13.

Pinzer, B. R., Schneebeli, M., and Kaempfer, T. U. (2012). Vapor flux and recrystallization during dry snow metamorphism under a steady temperature gradient as observed by time-lapse micro-tomography. *The Cryosphere Discussions*, 6(3):1673–1714.

Polder, D. and van Santeen, J. H. (1946). The effective permeability of mixtures of solids. *Physica*, 12(5):257–271.

Pomeroy, J. and Gray, D. (1990). Saltation of Snow. *Water resources research*, 26(7):1583–1594.

Pomeroy, J. and Li, L. (2010). Prairie and arctic areal snow cover mass balance using a blowing snow model. *Journal of Geophysical Research*, 105:619–634.

Pomeroy, J. W., Bewley, D. S., Essery, R. L. H., Hedstrom, N. R., Link, T., Granger, R. J., Sicart, J. E., Ellis, C. R., and Janowicz, J. R. (2006). Shrub tundra snowmelt. *Hydrological Processes*, 20(4):923–941.

Pomeroy, J. W., Gray, D. M., and Landine, P. G. (1993). The prairie blowing snow model - chracteristics, validation, operation. *Journal of Hydrology*, 144:165–192.

Pomeroy, J. W., Gray, D. M., Shook, K. R., Toth, B., Essery, R. L. H., Pietroniro, A., and Hedstrom, N. (1998). An evaluation of snow accumulation and ablation processes for land surface modelling. *Hydrological Processes*, 12(15):2339–2367.

Pomeroy, J. W. and Li, L. (2000). Prairie and arctic areal snow cover mass balance using a blowing snow model. *Journal of Geophysical Research*, 105(D21):619–634.

Pomeroy, J. W., Marsh, P., and Gray, D. M. (1997). Application of a distributed blowing snow model to the Arctic. *Hydrological Processes*, 11:1451–1464.

Purves, R. S., Barton, J. S., Mackaness, W. A., and Sugden, D. E. (1998). The development of a rule-based spatial model of wind transport and deposition of snow. *Annals of Glaciology*, 26:197–202.

Rees, A., English, M., Derksen, C., Toose, P., and Silis, A. (2013). Observations of late winter Canadian tundra snow cover properties. *Hydrological Processes*, in press.

Rees, G. (2001). *Physical Principles of Remote Sensing*. Cambridge University Press, Cambridge.

Riche, F. and Schneebeli, M. (2013). Thermal conductivity of snow measured by three independent methods and anisotropy considerations. *The Cryosphere*, 7:217–227.

Rott, H., Heidinger, M., Nagler, T., Cline, D., and Yueh, S. (2009). Retrieval of snow parameters from Ku-band and X-band radar backscatter measurements. In *2009 IEEE International Geoscience and Remote Sensing Symposium*, pages 144–147. Institute of Electrical and Electronics Engineers.

Rott, H., Sturm, K., and Miller, H. (1993). Active and passive microwave signatures of Antarctic firn by means of field-measurements and satellite data. *Annals of Glaciology*, 17:337–343.

Rott, H., Yueh, S., Cline, D., Duguay, C., Essery, R., Haas, C., Heliere, F., Kern, M., Macelloni, G., Malnes, E., Nagler, T., Pulliainen, J., Rebhan, H., and Thompson, A. (2010). Cold Regions Hydrology High-Resolution Observatory for Snow and Cold Land Processes. *Proceedings of the IEEE*, 98(5):752–765.

Rouse, W. (1991). Impacts of Hudson Bay on the terrestrial climate of the Hudson Bay Lowlands. *Arctic and Alpine Research*, 23(1):24–30.

Sarabandi, K., Ulaby, F., and Tassoudji, M. (1990). Calibration of polarimetric radar systems with good polarization isolation. *IEEE Transactions on Geoscience and Remote Sensing*, 28(1):70–75.

Schneebeli, M., Pielmeier, C., and Johnson, J. B. (1999). Measuring snow microstructure and hardness using a high resolution penetrometer. *Cold Regions Science and Technology*, 30(1):101–114.

Schwander, H., Mayer, B., Ruggaber, a., Albold, a., Seckmeyer, G., and Koepke, P. (1999). Method to determine snow albedo values in the ultraviolet for radiative transfer modeling. *Applied optics*, 38(18):3869–3875.

Scipión, D. E., Mott, R., Lehning, M., Schneebeli, M., and Berne, A. (2013). Seasonal small-scale spatial variability in alpine snowfall and snow accumulation. *Water resources research*, 49(3):1446–1457.

Serreze, M. C. and Barry, R. G. (2005). *The Arctic climate system*. Cambridge University Press.

Serreze, M. C., Walsh, J. E., Osterkamp, T., Dyurgerov, M., Romanovsky, V., Oechel, W. C., Morison, J., Zhang, T., and Barry, R. G. (2000). Observational evidence of recent change in the northern high-latitude environment. *Climate Change*, 46:159–207.

Shi, J. (2004). Estimation of snow water equivalence with two Ku-band dual polarization radar. In *2004 IEEE International Geoscience and Remote Sensing Symposium Proceedings*, pages 1649–1652. IEEE.

Shi, J., Yueh, S., and Cline, D. (2003). On estimation of snow water equivalence using L-band and Ku-band radar. In *2003 IEEE International Geoscience and Remote Sensing Symposium Proceedings*, volume 2, pages 845–847. IEEE.

Shi, J. C. (2008). Active microwave remote sensing systems and applications to snow monitoring. In Liang, S., editor, *Advances in Land Remote Sensing: System, Modelling, Inversion and Application*. Springer, Maryland.

Shi, J. C. and Dozier, J. (2000). Estimation of snow water equivalence using SIR-C/X-SAR, part II: Inferring snow depth and particle size. *IEEE Transactions on Geoscience and Remote Sensing*, 38(6):2475–2488.

Shi, X., Dery, S. J., Groisman, P. Y., and Lettenmaier, D. P. (2013). Relationships between recent pan-arctic snow cover and hydroclimate trends. *Journal of Climate*, 26(6):2048–2064.

Sihvola, A. and Tiuri, M. (1986). Snow fork for field determination of the density and wetness profiles of a snow pack. *IEEE Transactions on Geoscience and Remote Sensing*, GE-24(5):717 –721.

Stiles, W. and Ulaby, F. (1980). The active and passive microwave response to snow parameters 1. Wetness. *Journal of Geophysical Research*, 85(C2):1037–1044.

Stiles, W. H. and Ulaby, F. T. (1982). Dielectric properties of snow. Technical report, Kansas University Centre for Research Lawrence Remote Sensing Lab.

Strozzi, T. and Matzler, C. (1998). Backscattering measurements of alpine snowcovers at 5.3 and 35 GHz. *IEEE Transactions on Geoscience and Remote Sensing*, 38(12):2616–2624.

Sturm, M. and Benson, C. (2004). Scales of spatial heterogeneity for perennial and seasonal snow layers. *Annals of Glaciology*, 38:253–260.

Sturm, M. and Benson, C. S. (1997). Vapor transport, grain growth and depth-hoar development in the subarctic snow. *Journal of Glaciology*, 43(143):42–59.

Sturm, M., Holmgren, J., Konig, M., and Morris, K. (1997). The thermal conductivity of seasonal snow. *Journal of Glaciology*, 43(143):26–41.

Sturm, M., Holmgren, J., and Liston, G. E. (1995). A seasonal snow cover classification-system for local to global applications. *Journal of Climate*, 8(5):1261–1283.

Sturm, M. and Johnson, J. B. (1991). Natural-convection in the sub-arctic snow sover. *Journal of Geophysical Research-Solid Earth and Planets*, 96(B7):11657–11671.

Sturm, M., Taras, B., Liston, G. E., Derksen, C., Jonas, T., and Lea, J. (2010). Estimating snow water equivalent using snow depth data and climate classes. *Journal of Hydrometeorology*, 11(6):1380–1394.

Sturm, M. and Wagner, A. M. (2010). Using repeated patterns in snow distribution modeling: An Arctic example. *Water resources research*, 46:W12549.

Tape, K. D., Rutter, N., Marshall, H. P., Essery, R., and Sturm, M. (2010). Recording microscale variations in snowpack layering using near-infrared photography. *Journal of Glaciology*, 56(195):75–80.

Taras, B., Sturm, M., and Liston, G. E. (2002). Snow–ground interface temperatures in the Kuparuk River Basin, Arctic Alaska: Measurements and model. *Journal of Hydrometeorology*, 3(4):377.

Tinga, W. R. (1973). Generalized approach to multiphase dielectric mixture theory. *Journal of Applied Physics*, 44(9):3897–3902.

Tiuri, M. (1984). The complex dielectric constant of snow at microwave frequencies. *IEEE Journal of Oceanic Engineering*, 9(5):377–382.

Tsang, L., Pan, J., Liang, D., Li, Z., Cline, D., and Tan, Y. (2007). Modeling active microwave remote sensing of snow using dense media radiative transfer (DMRT) theory with multiple-scattering effects. *IEEE Transactions on Geoscience and Remote Sensing*, 45(4):990–1004.

Tse, K. K., Tsang, L., Chan, C. H., Ding, K. H., and Leung, K. W. (2007). Multiple scattering of waves by dense random distributions of sticky particles for applications in microwave scattering by terrestrial snow. *Radio Science*, 42:RS5001.

Ulaby, F., Moore, R., and Fung, A. (1981). *Microwave Remote Sensing: Active and Passive. Volume II Radar Remote Sensing and Surface Scattering and Emission Theory.* Addison-Wesley, Reading.

Ulaby, F. and Stiles, W. (1980). The active and passive microwave response to snow parameters 2. Water equivalent of dry snow. *Journal of Geophysical Research-Earth Surface*, 85(C2):1045–1049.

Ulaby, F., Stiles, W., and Abdelrazik, M. (1984). Snowcover influence on backscattering from terrain. *IEEE Transactions on Geoscience and Remote Sensing*, GE-22:126–133.

Werner, C., Wiesmann, A., Strozzi, T., Schneebeli, M., and Mätzler, C. (2010). The snowscat ground-based polarimetric scatterometer: Calibration and initial measurements from Davos, Switzerland. In *Geoscience and Remote Sensing Symposium*, pages 2363 –2366. IEEE.

West, D. (2000). Potential applications of 1 – 5 GHz radar backscatter measures of seasonal land snow cover. *Radio Science*, 35(4):967–981.

Willatt, R. C., Giles, K. A., Laxon, S. W., Stone-Drake, L., and Worby, A. P. (2010). Field investigations of Ku-band radar penetration into snow cover on Antarctic sea ice. *IEEE Transactions on Geoscience and Remote Sensing*, 48(1):365–372.

Williams, L., Sugden, D., and Gallagher, J. (1990). *Millimetric Radar Backscatter From Snowcover.* Stevenson, Dundee.

Woo, M. (2012). *Permafrost hydrology.* Springer.

Woodhouse, I. H. (2006). *Introduction to microwave remote sensing.* CRC Press.

Xu, X., Liang, D., Tsang, L., Andreadis, K. M., Josberger, E. G., Lettenmaier, D. P., Cline, D. W., and Yueh, S. H. (2010). Active remote sensing of snow using NMM3D/DMRT and comparison with CLPX II airborne data. *IEEE Journal of Selected Topics in Applied Earth Observations and Remote Sensing*, 3(4):689–697.

Xu, X., Tsang, L., and Yueh, S. (2012). Electromagnetic models of co/cross polarization of bicontinuous/dmrt in radar remote sensing of terrestrial snow at X- and Ku-band for CoReH2O and SCLP applications. *IEEE Journal of Selected Topics in Applied Earth Observations and Remote Sensing*, 5(3):1024–1032.

Yen, Y. (1962). Effective thermal conductivity of ventilated snow. *Journal of Geophysical Research*, 67(3):1091–1098.

Yosida, Z. (1955). Physical studies on deposited snow. Thermal properties. *Contributions from the Institute of Low Temperature Science*, 7:19–74.

Yueh, S., Dinardo, S., Akgiray, A., West, R., Cline, D., and Elder, K. (2009). Airborne Ku-band polarimetric radar remote sensing of terrestrial snow cover. *IEEE Transactions on Geoscience and Remote Sensing*, 47(10):3347–3364.

Zhang, T. (2005). Influence of the seasonal snow cover on the ground thermal regime: An overview. *Reviews of Geophysics*, 43:RG4002.

Zurk, L. M., Tsang, L., and Winebrenner, D. P. (1996). Scattering properties of dense media from Monte Carlo simulations with application to active remote sensing of snow. *Radio Science*, 31(4):803–819.